

# **Optical characterization of thin-film Si solar cells and knowledge transfer from bulk mc-Si**

Von der Fakultät für Mathematik, Naturwissenschaften und Informatik  
der Brandenburgischen Technischen Universität Cottbus

zur Erlangung des akademischen Grades

Doktor der Naturwissenschaften  
(Dr. rer. nat.)

genehmigte Dissertation

vorgelegt von

Diplom Physiker

André Klossek

geboren am 22. Juli 1983 in Cottbus, Deutschland

Gutachter: Apl. Prof. Dr. sc. nat. Martin Kittler

Gutachter: Prof. Dr. rer. nat. habil. Jürgen Reif

Gutachter: Prof. Dr. rer. nat. habil. Sigurd Schrader

Tag der mündlichen Prüfung: 18.11.2013

# Abstract

The aim of this work is to establish tools for optical characterization of defects in thin-film silicon solar cells. This is related to a challenging process of setup adjustments and careful interpretation of the measured raw data because of several artifacts and effects, which are typical for thin films. They are caused by the low layer/sample thickness and the related high impact of interfaces. Therefore, different thin-film samples were investigated to establish a process to correct/minimize these thin-film effects. The possibility of a knowledge transfer from mc-Si wafers with bulk thickness to thin Si films was checked. This would simplify a successful interpretation of the corrected data. Defects in mc-Si were investigated for many decades without the parasitic impact of thin films. Other Si phases, which are limited to thin-film samples, were investigated to learn details about their specific physical properties. These Si phases are amorphous and microcrystalline silicon. Additional to that electroluminescence investigations were performed on mc-Si solar cells. These investigation deals with topics, which are not even understood on bulk materials up to now. This could offer a basic for further knowledge transfers to thin-film Si.

Das Ziel dieser Arbeit ist es Werkzeuge für die optische Charakterisierung von Defekten in Dünnschicht Silizium Solarzellen zu etablieren. Das ist mit einem anspruchsvollen Prozess von Setupanpassungen und vorsichtigen Interpretationen der gemessenen Rohdaten verbunden, aufgrund verschiedener Artefakte und Effekte, die typisch für dünne Schichten sind. Diese werden durch die geringe Schicht-/Probendicke und den damit verbundenen hohen Einfluss von Grenzschichten verursacht. Deshalb wurden verschieden Dünnschichtproben untersucht um einen Prozess zu etablieren der es erlaubt diese Dünnschichteffekten zu korrigieren/vermeiden. Die Möglichkeit eines Wissenstransfers von mc-Si Wafern mit Volumendicke zu dünnen Si Filmen wurde geprüft. Dies würde eine erfolgreiche Interpretation der korrigierten Daten vereinfachen. Defekte in mc-Si wurden seit mehreren Jahrzehnten ohne den störenden Einfluss der dünnen Schichten untersucht. Andere Siliziumphasen, die auf Dünnschichtproben begrenzt sind, wurden untersucht um etwas über deren spezifische physikalische Eigenschaften zu lernen. Diese Siliziumphasen sind amorphes und mikrokristallines Silizium. Zusätzlich dazu wurden Elektrolumineszenzuntersuchungen an mc-Si Solarzellen durchgeführt. Diese Untersuchungen befassen sich mit Themen, die bisher noch nicht mal in Volumenmaterial verstanden sind. Das könnte eine Basis für weiterführende Wissenstransfers zu Dünnschichtsilizium bieten.

# Contents

<b>Introduction .....</b>	<b>5</b>
<b>1. Basic knowledge .....</b>	<b>8</b>
1.1 Recombination mechanisms in dislocated silicon .....	8
1.2 Principles of luminescence .....	12
1.2.1 Band-to-band luminescence (BB) in dislocated silicon .....	14
1.2.2 Defect-related luminescence (DRL) in dislocated silicon .....	18
1.3 Basic material properties of silicon phases in thin-film solar cells – a-Si:H, $\mu$ c-Si:H and c-Si .....	26
1.4 Overview of thin-film solar cell technologies .....	32
1.4.1 Silicon based thin-film solar cell technologies .....	34
1.4.2 Other thin-film solar cell technologies .....	37
<b>2. Experimental .....</b>	<b>40</b>
2.1 Photoluminescence (PL) investigations .....	40
2.2 Raman investigations .....	42
2.3 Typical effects in the analysis of thin-film samples with laser-based techniques .....	45
<b>Part I .....</b>	<b>51</b>
<b>3. Electron-beam crystallized large grained Si thin films .....</b>	<b>51</b>
3.1 Results and Discussion – Optical investigations .....	52
3.2 Results and Discussion –EBIC investigations .....	60
<b>4. Solid-phase crystallized poly-Si thin films with subsequent rapid- thermal processing .....</b>	<b>64</b>
4.1 Results and Discussion – PL investigations .....	65
4.2 Results and Discussion – Raman investigations .....	74
<b>5 Other thin-film Si phases – amorphous and microcrystalline Si .....</b>	<b>77</b>
5.1 Characterization of thin-film a-Si:H/ $\mu$ c-Si:H tandem solar cells on glass substrate .....	78
5.1.1 Results and Discussion – Optical investigations .....	80
5.1.2 Results and Discussion – EBIC investigations .....	85
5.2 Characterization of 500 nm $\mu$ c-Si:H on glass substrate .....	88
5.2.1 Results and Discussion – Raman investigations .....	89

## Contents

5.2.2 Results and Discussion – PL investigations .....	91
<b><u>Part II</u></b> .....	<b>102</b>
<b>6. Electroluminescence investigations on bulk mc-Si solar cells .....</b>	<b>102</b>
6.1 Anomalous temperature behavior of band-to-band (BB) EL in mc-Si solar cells .....	102
6.2 Distribution of defects and breakdown sites in UMG-Si cells studied by luminescence imaging .....	109
<b>7. Summary and conclusion .....</b>	<b>114</b>
<b>List of abbreviation and symbols .....</b>	<b>118</b>
<b>References .....</b>	<b>119</b>
<b>Acknowledgement .....</b>	<b>125</b>

# Introduction

Since the last 3 to 4 years, photovoltaic industry is in a crisis, despite of the fact that the market for PV modules is still increasing. This is mainly caused by an enormous price decline and the reduction of subsidies, especially in Europe. One possible direction for the future could be the developments in thin-film PV. Thin-film solar cells offer a high potential in cost and resource minimization [Gre2004]. This technology could reduce the electricity price by reducing fabrication costs and using less material [Amk2011]. In case of silicon films on glass substrates, the required material volume is typically 100 times less than for wafer-based multicrystalline silicon (mc-Si) solar cells. The lower thickness of the absorber layer can be compensated by using other Si phases. For instance hydrogenated amorphous (a-Si:H) and microcrystalline Si ( $\mu\text{c-Si:H}$ ) are characterized by higher absorption coefficients than pure crystalline Si (c-Si). That allows the absorption of the entire solar spectrum in layer thicknesses of a few micrometres or even less. However, this advantage is reduced by worse electrical properties (e.g. lower excess carrier lifetime). For that reason, other concepts base on the use of subsequently crystallized Si by irradiation (laser, electron-beam), thermal treatment, etc. This is a very rough classification of the enormous variety of Si based thin-film solar cell concepts. Finer classifications can base on different electrical concepts (single- or multi-junction cells, p-n junction cells, p-i-n heterojunction cells), materials (e.g. amorphous silicon, crystalline silicon (varying grain size)), cell structures etc. However, none of these concepts is able to compete against wafer-based Si solar cells of bulk thickness in the important parameters (costs, efficiency and long-time stability) up to now. For this reason, analytics is needed to improve the mentioned solar cell parameters as well as for quality control.

The analysis of thin-films differs from the analysis of bulk materials, because of several effects. For instance, luminescence techniques are affected by the low layer/sample thickness, which leads to low luminescence signals. The most important effect is the strong impact of interfaces. That becomes additionally amplified due to the required roughness of the interfaces to enhance photocurrent generation by light trapping. All cell concepts are characterized by distinct interface effects. A very important one is the enhanced recombination at interfaces, which can lead to specific distributions of carrier lifetime because of rough interfaces [Sei2011]. Other possible interface-related effects are band-gap alignment of the interface [Wei2005], band-gap states, problems with light trapping [Peu2003], light extraction, etc. The attention to these effects is especially required because almost all analytic techniques were originally designed for bulk samples and are not directly considered during the measurement. Therefore, it is very important to combine several characterization techniques and very careful interpretation of the obtained data.

## Aim and outline of this work

This work is a result of the PVcomB project (Competence Centre Thin-Film- and Nanotechnology for Photovoltaics Berlin) - Teilvorhaben 6 Analytik. The aim of this project is to establish analytic tools for thin-film PV with a special focus on the optical

characterization of defects, mainly by photoluminescence (PL) [Arg2002]. The PL results will be added by other techniques, such as Raman spectroscopy and electron-induced-beam-current (EBIC). The challenging adjustments for the application of the different techniques to thin films can be written in three key-questions.

### **1. How to correct/minimize thin-film effects?**

It is necessary to investigate the thin-film effects and their impact very precisely. That includes an exact identification of these effects on several samples. That shall lead to a possibility to correct/minimize their impact on the measured raw data.

### **2. What knowledge/methods can be transferred from bulk Si to thin-film ones?**

All Si thin films are characterized by a high concentration of various defects, independent on the exact type of sample/cell concept. These defects are one of the most important points limiting the excess carrier lifetime and the associated solar cell efficiency. Therefore, an elaborated investigation is necessary. Therefore, the corrected data from the first key-question must be interpreted carefully. The interpretation would be enormously simplified if it would be possible to transfer knowledge about defects and/or investigation methods from bulk mc-Si. At this material, defects were investigated for many decades without the parasitic thin-film effect.

### **3. What can be learned about the physical aspects of typical thin-film Si-phases?**

Some thin-film solar cell concepts base on amorphous and microcrystalline silicon. In these cases, a transfer of knowledge from mc-Si is obviously very restricted. However, it might be still possible to transfer investigation techniques/methods, which where originally designed on bulk materials. Physical aspects about the material-specific properties cannot be transferred. This becomes clear due to the fact that such silicon phases do not have applications or do not even exist in bulk thickness (e.g.  $\mu\text{c-Si:H}$ ). Therefore, physical aspects of those materials are very interesting, but hard to obtain because of the unavoidable presence of thin-film effects.

To answer these three key-questions the work is ordered into several chapters. In chapter 1 describes basic knowledge, which is necessary to discuss the obtained results on thin-film samples. That includes knowledge about mc-Si of bulk thickness, which is used as reference for the transfer as well as basic knowledge about the thin-film phases ( $\text{a-Si:H}$  and  $\mu\text{c-Si:H}$ ).

Chapter 2 gives an overview of the most important experimental techniques: PL and Raman spectroscopy. It also includes some comments about their application on thin films.

After chapter 2, this work is subdivided into two parts. In the first main part, the key-questions are discussed by investigating several Si thin-film samples on glass substrate (chapters 3 to 5). These samples represent a stepwise evolution from bulk mc-Si to other Si phases, which are restricted to thin-film applications. The evolution manifests in an increasing complexity of the cell stack and changed material properties of the Si layers. Chapter 3 marks the first step. A large grained electron-beam crystallized Si film with a thickness of around 10  $\mu\text{m}$  is investigated there. Its properties are very similar to those of bulk mc-Si. The middle step is given in chapter 4 by a 1.6  $\mu\text{m}$  thick poly-Si layer with a grain size of a few

## Introduction

micrometres. The final step is an a-Si:H/ $\mu$ c-Si:H tandem solar cell on glass substrate in chapter 5. The main advantage of such cell concepts is given by the limited efficiency of single-junction cells. All important parameters, such as short-circuit current ( $I_{SC}$ ), open circuit voltage ( $V_{OC}$ ), filling factor ( $FF$ ), etc. can increase due to the absorption by more than one bandgap energy. This was theoretically approximated by Meillaud et al. [Meil2006] and experimentally confirmed by several groups [Mei2002, Söd2010]. It will be a high challenge to minimize/correct the thin-film effects (first key-question) due to the complex cell structure. But the main focus of this chapter is on the physical aspects of  $\mu$ c-Si:H (third key-question). Thereby two aspects are of particular interest. The first aspect is on PL itself, where variations in the deposition and growth conditions have an enormous impact on the detected spectra [Bha1983, Bou1983, Yue2000, etc.]. The second aspect is the transformation process from amorphous to microcrystalline silicon. This is investigated by measurements of samples with various crystallinities (ratio between amorphous and crystalline phase).

The shorter second part is discussed in chapter 6. It deals with electroluminescence investigations on mc-Si solar cells to offer a basic for knowledge transfer to thin-film samples in the future.

The results of both parts are summarized in chapter 7, with a focus on the answers of the three key-questions.

# 1. Basic knowledge

This chapter gives an overview about basic knowledge, which is necessary to follow the description of the experimental results in chapters 3 to 6. It will be focused on radiative recombination mechanisms and the related luminescence signals in silicon according to the main technique – PL. Thereby the sub-chapters 1.2.1 and 1.2.2 will describe luminescence features in bulk mc-Si. It is the reference for the desired transfer of knowledge to thin-film Si. The structural and optical properties of other Si thin-film phases (a-Si:H,  $\mu$ c-Si:H) are given in sub-chapter 1.3. Sub-chapter 1.4 gives an overview of commonly used thin-film solar cell technologies.

## 1.1 Recombination mechanisms in dislocated silicon

Excited electrons in the conduction band are in a meta-stable state and will return to a lower energy position in the valence band. This transition consists of an electron moving back into an empty valence band state and consequently, when the electron falls back down into the valence band, it removes a hole. This process is called recombination. A common classification of the different recombination mechanisms distinguishes intrinsic and extrinsic mechanisms:

- Intrinsic recombination mechanisms are always present even in ideal crystals and do not depend on the specific technique used for crystal growth. Depending on the way, the excess energy released by the decay of an electron-hole pair is dispersed, two fundamental processes may be distinguished: radiative recombination and Auger recombination. Both mechanisms are characterized by a direct transition from conduction to valence band.
- In case of extrinsic recombination mechanisms, the decay of an electron-hole pair does not occur directly via a band-to-band (BB) transition of an electron – as in the case of the intrinsic mechanisms – but stepwise by transition via a defect centers. These centers are localized within the band gap. Extrinsic recombination mechanisms can be distinguished in Shockley-Read-Hall (SRH) recombination and surface recombination, depending on the origin of the defect centers. The defect centers are generated due to imperfections of the crystal structure. SRH is very often the dominant process, especially in indirect semiconductors.

### **Radiative recombination:**

Radiative recombination consists of direct annihilation of one conduction band electron and one valence band hole. In case of indirect semiconductors, it occurs with the participation of one or multiple phonons to conserve the momentum. The probability of BB transitions in



## 1. Basic knowledge

indirect semiconductor is much lower than that in direct ones. The lifetime  $\tau$  of excess carriers is much longer. The radiative recombination rate  $R$  can be written as:

$$R = -\frac{dn}{d\tau} = -\frac{dp}{d\tau} = Bnp \quad (1.1.1)$$

where  $n$  and  $p$  are electron and hole concentration and  $B$  the radiative recombination coefficient. In case of excitation, it is useful to distinguish between equilibrium concentrations  $n_0, p_0$  and concentrations of the excess carriers  $\Delta n, \Delta p$

$$\begin{aligned} n &= n_0 + \Delta n \\ p &= p_0 + \Delta p \end{aligned} \quad (1.1.2)$$

In most cases the excitation is done in a way that the excess carrier concentrations are equal  $\Delta n = \Delta p$  (e.g. PL). Then the semiconductor is in a non-equilibrium state and the excess carriers begin to recombine. The excess radiative recombination rate  $\Delta R$  is the difference of the total recombination rate  $R$  and the thermal equilibrium condition  $R_0$

$$\begin{aligned} \Delta R &= R - R_0 = Bnp - Bn_0p_0 = B(n_0 + \Delta n)(p_0 + \Delta p) - Bn_0p_0 \\ &= B(n_0 + p_0)\Delta n + B\Delta n^2 \end{aligned} \quad (1.1.3)$$

At low injection condition, ( $\Delta n \ll n_0$ ) the quadratic term can be neglected. Under high injection condition, the term becomes dominant.

From now on, the radiative recombination rate will be written as  $R_{rad}$  to separate it from other recombination mechanisms.

### **Shockley-Read-Hall recombination:**

SRH recombination denotes the recombination process through energy levels within the band gap. The energy levels are generated due to crystal defects. Some of these defects can be electrically active, causing levels in the band gap. So these defects act as recombination active centers or traps for minority carriers. Especially important are impurities due to transition metals and extended defects.

The SRH model describes the total recombination in the following assumptions:

- No radiative or Auger transitions
- energy position of the recombination centre  $E_T$  is independent on the occupation
- relaxation of carriers captured at the centre is much faster than the emission processes
- recombination centers are homogeneously distributed and at much lower concentration than the doping concentration
- no direct interaction between the defects
- Fermi-Dirac-Statistic is applicable

## 1. Basic knowledge

Under low injection conditions the recombination rate is given by [Sho1952, Hal1952]:

$$R_{SRH} = \frac{np - n_i^2}{(n + n_T)\tau_p + (p + p_T)\tau_n} \quad (1.1.4)$$

where the electron and hole concentrations are  $n$  and  $p$  and  $n_i$  is the intrinsic carrier concentration. The index  $T$  denotes the concentration of trap states.  $\tau_p$  and  $\tau_n$  are the lifetimes of the excess electrons and holes (completely occupied or empty). They are defined by following equations:

$$\begin{aligned} n_T &= N_C \exp\left[\frac{E_T - E_C}{k_B T}\right] & \tau_p &= \frac{1}{N_T \sigma_p v_{th,p}} \\ p_T &= N_V \exp\left[\frac{E_V - E_T}{k_B T}\right] & \tau_n &= \frac{1}{N_T \sigma_n v_{th,n}} \end{aligned} \quad (1.1.5) \quad (1.1.6)$$

with  $N_C$  and  $N_V$  the effective densities of states in the conduction and valence bands,  $E_C$  and  $E_V$  the conduction and valence band energy,  $E_T$  the energy of the trap.  $N_T$  the trap concentration,  $\sigma_n$ ,  $\sigma_p$  the capture cross sections of the trap for electrons and holes, and  $v_{th,n}$ ,  $v_{th,p}$  the thermal velocities of the electrons and holes, respectively. In case of n-type semiconductors, equation (1.1.4) can be simplified to:

$$R_{SRH} = \frac{np - n_i^2}{(n + n_T)\tau_p} \quad (1.1.7)$$

Under low injection condition ( $\Delta n \approx \Delta p \ll n_0$ ,  $n = n_0 + \Delta n$ ,  $p = p_0 + \Delta p$ , and  $n_0 p_0 = n_i^2$ ) equation (1.1.7) can be rewritten:

$$R_{SRH} = \frac{(n_0 + p_0)\Delta n + \Delta n^2}{(n + n_T)\tau_p} \approx \frac{n_0 \Delta n}{(n + n_T)\tau_p} = \frac{N_T \sigma_p v_{th,p} n_0 \Delta n}{n + n_i \exp[(E_T - E_i)/k_B T]} \approx \frac{\Delta n}{\tau_{SRH}} \quad (1.1.8)$$

### Auger recombination:

Auger recombination becomes important under high injection conditions or in highly doped semiconductors (majority carriers  $\sim 10^{18} \text{ cm}^{-3}$ ). Auger recombination processes can be understood as an extended version of BB transitions. It involves three particles: an electron and a hole, which recombines in a direct BB transition and gives off the resulting energy to another electron (eeh) or hole (ehh) [Dzi1977]. Auger recombination occurs through a participation of three particles. Therefore, the recombination rate is proportional to the product of the concentrations of the three particles. The two processes define the recombination rate  $R_{Auger}$ :

$$R_{Auger} = C_{eeh} n^2 p + C_{ehh} n p^2 \quad (1.1.9)$$

## 1. Basic knowledge

where the coefficients  $C_{eeh}$  and  $C_{ehh}$  represent the e-e-h and e-h-h recombination mechanisms, respectively. Figure 1.1.1 illustrates some possible Auger recombination processes.

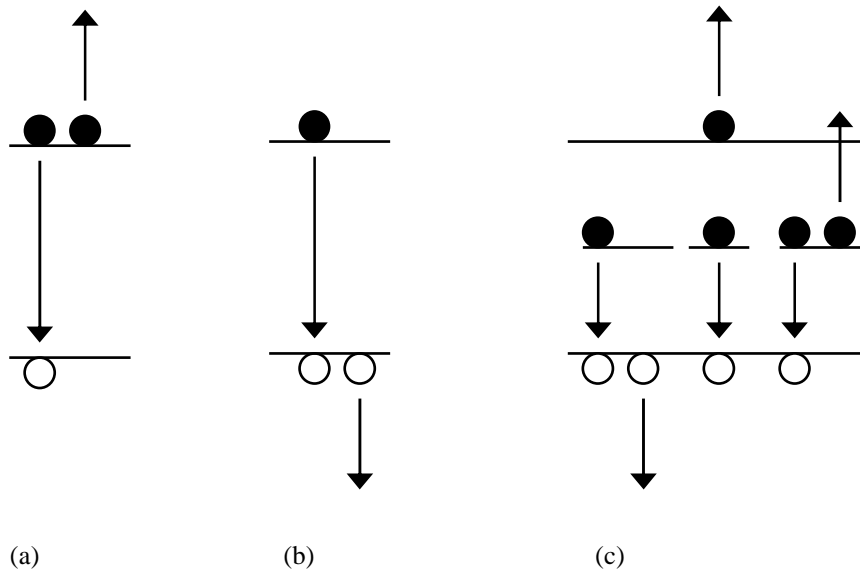


**Figure 1.1.1:** Scheme of Auger recombination processes: In electron-electron-hole process the transition energy is carried away by an electron (a); in electron-hole-hole process transition energy is carried away by a hole (b); process with participation of traps in the bandgap and different possibilities to carry the transition energy (c)

Both coefficients are slightly dependent on the temperature [Dzi1977] (Table 1.1.1), but independent on impurity concentrations.

T [K]	77	300	400
$C_{eeh}$ [ $\text{cm}^6/\text{s}$ ]	$2,3 \times 10^{-31}$	$2,8 \times 10^{-31}$	$2,8 \times 10^{-31}$
$C_{ehh}$ [ $\text{cm}^6/\text{s}$ ]	$7,8 \times 10^{-31}$	$9,9 \times 10^{-31}$	$1,2 \times 10^{-31}$

**Table 1.1.1:** Auger coefficients at different temperatures (data from [Dzi1977])

### Surface recombination:

Recombination at surfaces and interfaces can have a significant impact on the behavior of semiconductor devices. This is because surfaces and interfaces typically contain a large number of recombination centers because of the abrupt termination of the semiconductor crystal, which leaves a large number of electrically active states. In addition, the surfaces and interfaces are more likely to contain impurities since they are exposed during the device fabrication process. Surface recombination is similar to SRH recombination. Under assumption of only one trap, the rate can be written as [Schr1990]:

$$R_{Surf} = \frac{np - n_i^2}{\frac{1}{v_p}(n + n_T) + \frac{1}{v_p}(p + p_T)} \quad (1.1.10)$$

## 1. Basic knowledge

with the recombination velocities  $v_p$  and  $v_n$ .

All recombination mechanisms can be summarized in the total recombination rate  $R_{tot}$ .

$$R_{tot} = R_{rad} + R_{SRH} + R_{Auger} + R_{surface} \quad (1.1.11)$$

where  $R_{rad}$ ,  $R_{SRH}$ ,  $R_{Auger}$ , and  $R_{surf}$  denote the radiative, Shockley-Read-Hall, Auger and surface recombination rate, respectively. Therefore, the total lifetime of the excess carriers depends on all four recombination processes and can be written by the following equation:

$$\frac{1}{\tau_{tot}} = \frac{1}{\tau_{rad}} + \frac{1}{\tau_{SRH}} + \frac{1}{\tau_{Auger}} + \frac{1}{\tau_{surf}} \quad (1.1.12)$$

where  $\tau_{rad}$ ,  $\tau_{SRH}$  and  $\tau_{Auger}$  without  $\tau_{surf}$  represent the bulk lifetime  $\tau_{bulk}$ . This distinction is used to describe the efficiency of surface passivation. It is especially helpful to describe devices with a high impact of interfaces, such as thin-film solar cells.

$$\frac{1}{\tau_{tot}} = \frac{1}{\tau_{bulk}} + \frac{1}{\tau_{surface}} \quad (1.1.13)$$

## 1.2 Principles of luminescence

Luminescence spectroscopy is a technique, which is used to study defects in semiconductors. The main principle for interpretation spectra is the conservation of energy and momentum. Photons with an energy  $h\nu > E_g$  (bandgap) will be able to excite electrons from the valence band to the conduction band and leaving a hole in the valence band. The electron in the conduction band and hole in the valence band are called electron-hole pair. After excitation, this pair will recombine to obtain a lower energy state. The first step is thermal relaxations (thermalisation), whose timescale is very short (picoseconds). This means that the electron moves to the conduction band minimum. From this point, there are different possibilities to reach the state of equilibrium. Thereby it must be distinguished between the two types of semiconductors. The band diagrams of these two types are shown schematically in figure 1.2.1. Direct semiconductors are characterized by the same position of the conduction band minimum and valence band maximum in reciprocal space (figure 1.2.1a). In this case, a transition of an electron needs no phonon for conservation of momentum. Contrary to this, transitions in indirect semiconductors (figure 1.2.1b) need the participation of a phonon. Cheeseman [Che1952] first pointed out the possibility of such transitions.

## 1. Basic knowledge

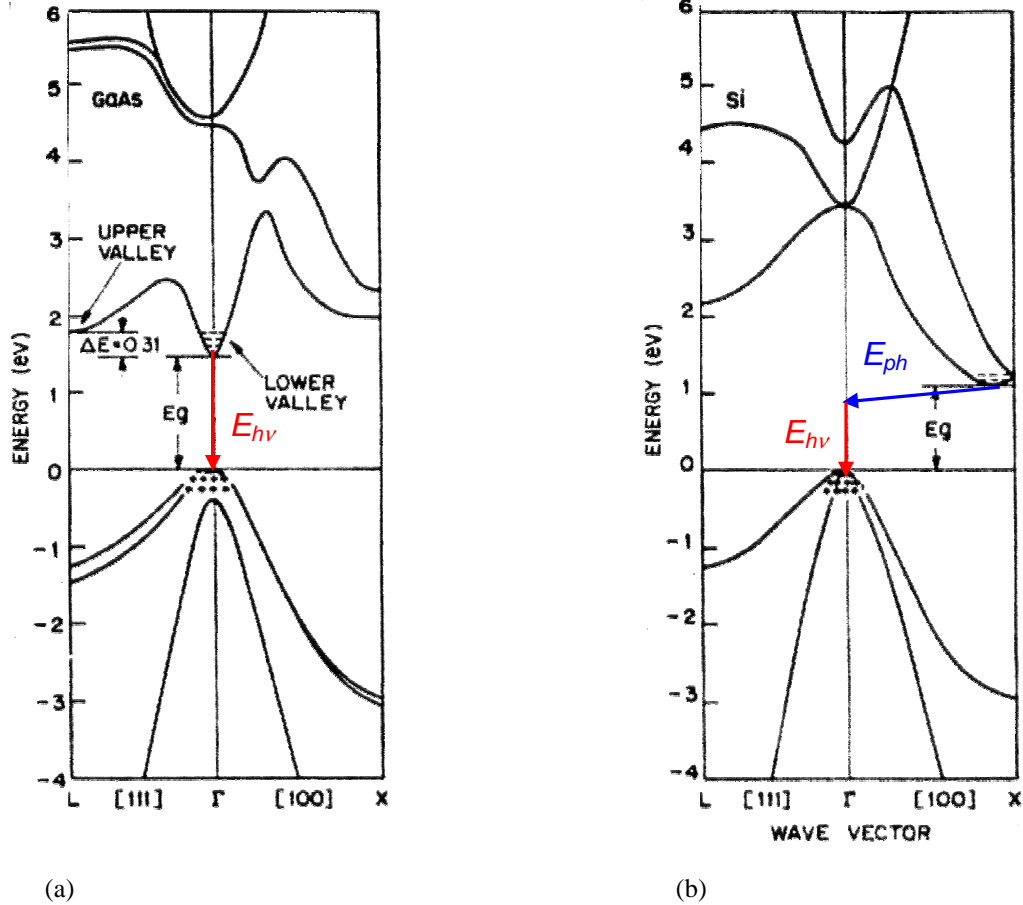


**Figure 1.2.1:** Luminescence in direct semiconductors (e.g. GaAs) (a); and indirect semiconductor (e.g. Si) (b)

Direct transitions are more probable than indirect transitions, because of this requirement. Such direct transitions from conduction to valence band are called band-to-band (BB) transitions. During this transition, the electron-hole pair loses energy. The energy must be transferred to some other particle. Transitions that emit photons are radiative processes, and transitions that generate only phonons are non-radiative processes. In indirect semiconductors, transitions involve both the energy of phonon  $E_{ph}$  and photon  $h\nu$ . Then the energy of the emitted photon is given by:

$$h\nu = E_g - E_{ph} \quad (1.2.1)$$

The effects of Coulomb interaction between the carriers lead to reduction of the energy of the emitted photons at lower temperatures. A part of the lost energy is transferred to excitons, formed by the interaction of a free hole and a free electron in the conduction band. The energy of the resulting photon is reduced by the energy of the exciton  $E_{ex}$ .

$$h\nu = E_g - E_{ph} - E_{ex} \quad (1.2.2)$$

The excitons may become bound to neutral donor or acceptor, forming bound excitons. This reduces the energy of the emitted photon again. The lost energy is labeled as binding energy of the excitons  $E_b$ .

## 1. Basic knowledge

$$h\nu = E_g - E_{ph} - E_{ex} - E_b \quad (1.2.3)$$

The energy position of the peaks in the luminescence spectrum characterizes the types of transitions during the recombination process. Additional to the band-to-band transition there are other peaks in the luminescence spectrum (e.g. D-lines).

In the next two sub-chapters, the luminescence in mc-Si will be discussed more detailed. Sub-chapter 1.2.1 will be focused on the BB luminescence, which is characteristic for silicon itself. It describes the ideal case of defect-free silicon. Sub-chapter 1.2.2 will focus on defect-related luminescence (DRL), which represents the impact of impurities, dislocations etc. These defects are characteristic for mc-Si but more important in thin-film Si because of smaller grain sizes and the associated higher amount of grain boundaries. Of course, these two sub-chapters cannot describe luminescence in mc-Si completely. It is just a short overview. Nevertheless, it is necessary to provide a basic image of luminescence on bulk mc-Si as reference for thin-film Si. The important properties of thin films will be described in sub-chapters 1.3. This comparison is designed to answer the second key-question of this work: “What knowledge/methods can be transferred from bulk Si to thin-film Si?”

### 1.2.1 Band-to-band luminescence (BB) in dislocated silicon

Band-to-band luminescence (BB) is the transition between the conduction and valence band, without participation of any traps within the bandgap. Therefore, it represents ‘defect-free’ silicon in luminescence techniques and was illustrated in figure 1.2.1(b) previously. The most important parameter for radiative recombination is the radiative recombination coefficient  $B(h\nu, T)$  [Hal1959]. It includes all material properties, which are important for radiative recombination, such as dependences on temperature and photon energy. It can be used as a measure of the luminescence intensity.

Theoretical estimations base on a detailed balance principle [Roo1954]. According to that, the radiative recombination rate at thermal equilibrium in an elementary frequency interval,  $d\nu$ , at frequency  $\nu$ , is equal to the corresponding generation rate of electron-hole pairs by thermal radiation. So Planck’s law can be used:

$$\rho(\nu)d\nu = \frac{8\pi\nu^2}{c^3} \frac{n_s^2 \left[ \frac{d(n_s\nu)}{d\nu} \right]}{\exp\left[\frac{h\nu}{kT}\right] - 1} d\nu \quad (1.2.1.1)$$

, where the generation rate is defined by the spectral photon density in the semiconductor  $\rho(\nu)$  (number of photons in unit volume and unit frequency interval). Another parameter is the absorption probability. It is given as the product of group velocity of the light,  $v_g = c d\nu / d(n_s\nu)$ , and the absorption coefficient of the semiconductor  $\alpha$ . So the recombination rate can be written as:

## 1. Basic knowledge

$$R(\nu)d\nu = \frac{8\pi\alpha n^2}{c^2} \frac{\nu^2}{\exp\left[\frac{h\nu}{kT}\right] - 1} d\nu \quad (1.2.1.2)$$

, where  $n$  is the refractive index of the semiconductor,  $c$ ,  $h$ , and  $k$  are the speed of light, Boltzmann and Planck constants, respectively. The validity of this approach can be checked by writing (1.2.1.2) in a different form. The spontaneous emission rate in an excited semiconductor can be written by the generalized Planck equation [Wür1982]:

$$dR_{sp}(E_\gamma, T) = \frac{E_\gamma^2 n_s^2}{\pi^2 \hbar^3 c^2} \alpha_{BB}(E_\gamma, T) \frac{1}{\exp\left[\frac{E_\gamma - \Delta\eta}{k_B T}\right]} dE_\gamma \quad (1.2.1.3)$$

This is an extended form of the van Roosbroeck equation, where  $\Delta\eta$  is the separation of the quasi-Fermi energies due to excitation and  $\alpha_{BB}$  the absorption coefficient in the wavelength range of the BB transition. It can be simplified for non-degenerated occupation of the bands to:

$$dR_{sp}(E_\gamma) = \frac{E_\gamma^2 n^2}{4\pi^2 \hbar^3 c^2} a_{BB}(E_\gamma, T) \exp\left[\frac{\Delta\eta - E_\gamma}{k_B T}\right] dE_\gamma \quad (1.2.1.4)$$

This equation can be used to get an idea of the BB luminescence signal in silicon by assuming values for  $\Delta\eta$  and inserting known values of  $\alpha_{BB}(E_\nu, T)$  from absorption measurements [Gre1995]. The calculated spectrum (Fig. 1.2.1.1) exhibits amazing similarity with experimentally detected BB luminescence.

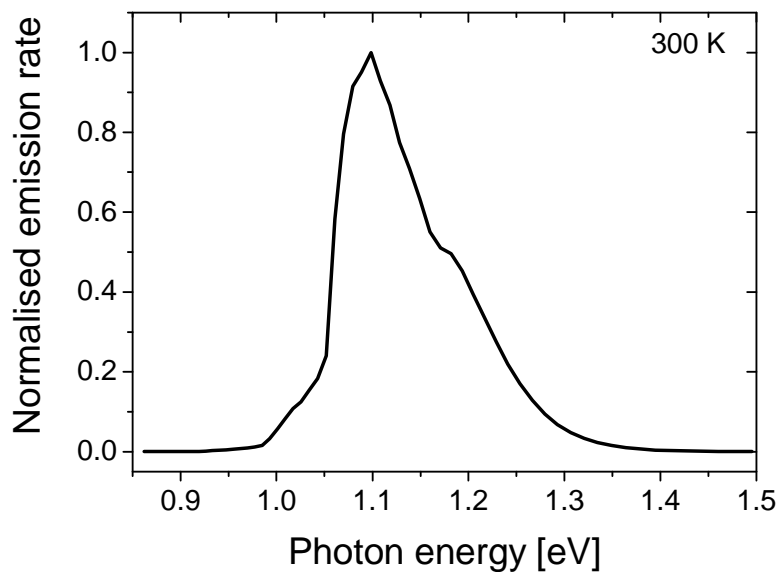


**Figure 1.2.1.1:** Calculated BB spectrum at silicon by using equation (1.2.1.4) with  $\Delta\eta=0.5$  eV,  $T=300$  K and  $\alpha_{BB}(300$  K) extracted from [Gre1995]

## 1. Basic knowledge

As an indirect semiconductor, transitions in silicon must be assisted by phonon interactions. This fact is included in the absorption coefficient  $\alpha(\nu)$ . Macfarlane et al. [Mac1955] gave an approximation for that:

$$a = A \left[ \frac{(h\nu - E_g + k\Theta)^2}{\exp\left[\frac{\Theta}{T}\right] - 1} + \frac{(h\nu - E_g - k\Theta)^2}{1 - \exp\left[\frac{-\Theta}{T}\right]} \right]; \quad (1.2.1.5a)$$

$$a = A \left[ \frac{(h\nu - E_g + k\Theta)^2}{\exp\left[\frac{\Theta}{T}\right] - 1} \right]; \quad (1.2.15b)$$

$$\alpha = 0; \quad (1.2.1.5c)$$

where  $A$  is a constant,  $E_g$  is the bandgap energy of silicon,  $\Theta$  is the Debye temperature and  $T$  is the temperature. With these equations, it is possible to obtain a formula for the radiative recombination coefficient of transitions in indirect semiconductors  $B_{indirect}$  [Var1967]:

$$B_{indirect} = \frac{Ah^3 n_s^2}{2\pi^2 c_2} \frac{E_g^2}{M_C (m_e m_h)^{3/2}} \frac{\exp\left[\frac{\Theta}{T}\right] + 1}{\exp\left[\frac{\Theta}{T}\right] - 1} \quad (1.2.1.6)$$

, where  $m_e$ ,  $m_h$  are the effective masses of electrons and holes and  $M_C$  is the number of equivalent minima in the conduction band (Si:  $M_C = 6$ ). One limit of it this model is given by the temperature behavior of BB luminescence. Equation (1.2.1.6) includes the increasing occupation of phonon states with increasing temperature behavior. Correspondingly, the BB intensity should increase with temperature. Despite of this that behavior is not observed experimentally [Schl1974] in most cases. Therefore, the predicted mechanisms to describe the temperature behavior are not completely understood. The reason for this disagreement between theory and experimental observations is the formation of excitons. They are formed due to the Coulomb attraction between electrons and holes. Neutral donors can bind some of these or acceptors, forming bound excitons (see: chapter 1.2). Because of the small binding energy of the excitons they can easily be destroyed at higher temperatures. The recombination probability increases as result of their spatial neighborhood. [Schl1974] gives an improved expression of the radiative recombination rate:

$$B_{indirect} = 2\sqrt{\pi} \sqrt{\frac{G}{kT}} \left( 1 + 2 \frac{G}{kT} \exp\left[\frac{G}{kT}\right] \right) C \frac{\exp\left[\frac{\Theta}{T}\right] + 1}{\exp\left[\frac{\Theta}{T}\right] - 1} \quad (1.2.1.7)$$

, where  $G$  is the binding energy of the excitons ( $\sim 15$  meV) and  $C$  the first two temperature independent terms in (1.2.1.6). The temperature dependence of the radiative recombination coefficient  $B$  was calculated in several studies. An overview is given in figure 1.2.1.2.



## 1. Basic knowledge

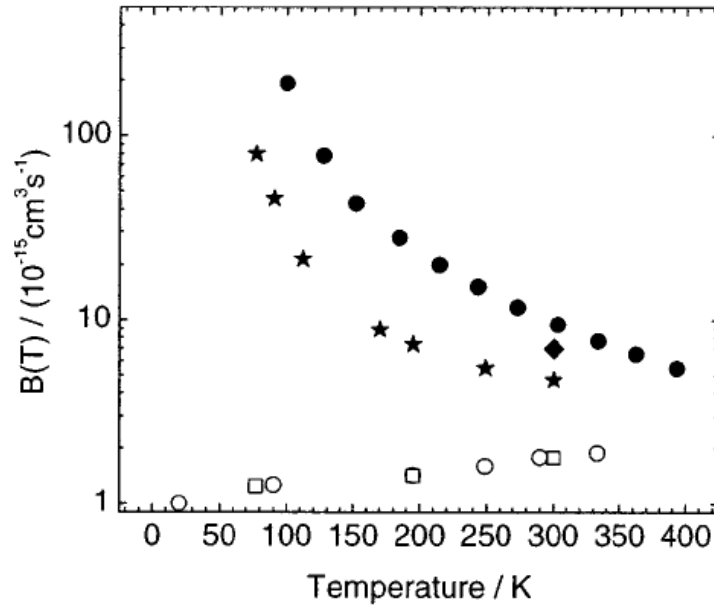


**Figure 1.2.1.2:** Comparison of calculated  $B(T)$  from e.g. Varshni [Var1967] (open circles), Schlangenotto et al.: [Schl1974] (full circles) and Trupke et al. [Tru2003] (stars); (Image taken from [Tru2003]).

There one can see increasing  $B(T)$  with increasing temperature [Var1967] as well as decreasing  $B(T)$  with increasing temperature [Schl1974, Tru2003]. The calculations by Schlangenotto and Trupke include the impact of excitons at lower temperatures. Note the wide range of  $B(T)$  due to the logarithmic scale. So, it should be expected that the BB intensity decreases with increasing temperature from the theoretical point of view. That is called the normal temperature behavior. Indeed, such luminescence quenching is usually observed for high-grade silicon. However, opposite temperature behavior, namely, increase of the BB intensity with temperature has been observed for silicon subjected to ion implantation [Ng2001] and for solar grade materials [Bre2008]. This anomalous temperature behavior of the BB intensity has been related to shallow levels in the silicon band gap.

In summary, the temperature behavior of the BB intensity is determined by two main factors. The first one is the radiative recombination coefficient  $B(T)$  and the second one is the minority carrier lifetime  $\tau(T)$ . Therefore, it can be expected that the temperature dependence of the carrier lifetime will influence that of BB luminescence. Besides, above described temperature dependence of the recombination coefficient, there are other factors, which can limit the luminescence intensity. For instance, competitive non-radiative recombination paths decrease the concentration of the injected carriers  $\Delta n$  and  $\Delta p$  and lead to observed decrease in the luminescence [Arg2007]. Another factor is the influence of the used analysis technique. This will be discussed by comparative measurements of EL and PL in sub-chapter 6.1.

However, it is widely accepted that the temperature behavior in PL is a measure for the silicon material quality. Despite of this fact the different mechanisms are not completely understood up to know. It can be summarized that normal temperature behavior denotes a quite high material quality and the opposite for anomalous temperature behavior. In this way, the temperature behavior gives an indirect and restricted approach to the material quality.

## 1. Basic knowledge

Another important point is that it includes evidences to other material properties, such as non-radiative recombination processes. These processes are not directly visible in PL but estimations about them can be obtained from the temperature behavior.

### 1.2.2 Defect-related luminescence (DRL) in dislocated silicon

In semiconductors, e.g. silicon, an enormous number of several defects can be distinguished. A very rough classification can be obtained by separating into dislocations and precipitates. Of course, interactions between both are possible. This chapter gives a rough overview of these two kinds of defects. Thereby the separation between dislocations and precipitates should be used. However, in realistic investigation/characterization processes, excluding specially prepared samples (e.g. model dislocations by wafer bonding [Ike1998]), it is very difficult to separate both and sometimes not possible. Therefore the more general term 'defect-related luminescence' (DRL) will be used.

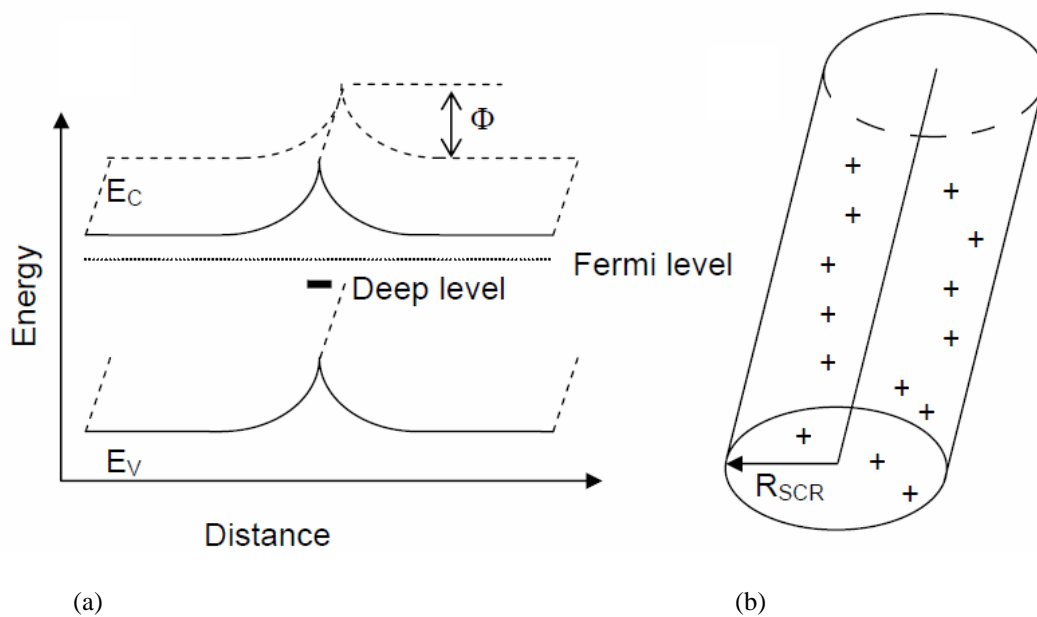


**Figure 1.2.2.1:** Model of a charged dislocation in n-type material: space-charge region and deformation of bands at dislocation (a); space-charge region (Read-Cylinder) with charged dopants (b); Image taken from [Arg2007a]

Dislocations and grain boundaries are some of the most important defects in silicon, because of their strong impact on its recombination activity. Dislocations can be charged due to the presence of dangling bonds. Such behavior was observed in doped silicon, where carriers were captured at dislocations [Ale1990]. This was found to be one of the main reasons for dislocation-related luminescence. In a simple estimation, it can be assumed that dislocations behave as charged lines, which attract minority carriers. Therefore, the dislocation lines must create a space-charge region around the dislocation (Read-Cylinder) because of the required charge conservation (Fig. 1.2.2.1).

## 1. Basic knowledge

Dislocations cause deformations of the bands in the semiconductor that compensate the dislocation charge. Kveder et al. [Kve2001] gave following equation about potential barrier  $\Phi$  and carrier density at the dislocation  $N_{tot}$ :

$$\Phi = \frac{eN_{tot}}{4\pi\epsilon_{Si}} \left[ \ln \left( \frac{N_{tot}^3}{\pi N_d} \right) - 1 \right] \quad (1.2.2.1)$$

, where  $\epsilon_{Si}$  is the permittivity of silicon,  $e$  the elementary charge and  $N_d$  the doping concentration. The radius of the Read-Cylinder is:

$$R_{SCR} = \sqrt{\frac{N_{tot}}{\pi N_d}} \quad (1.2.2.2)$$

In n-Si dislocations are negatively charged. The opposite charging is observed for p-Si. The recombination process of minority carries, captured by dislocations, is analogue to simple BB transitions. The only difference is that they recombine through states in the bandgap and the emitted photon energy is reduced correspondingly.

### Origin of defect-related luminescence (DRL)

In chapter 1.2.1 the well-known band-to-band transition (BB) was described, which is related to ‘defect-free’ silicon. Additional to that, there are other radiative recombination processes in silicon, which are related to defects. Figure 1.2.2.2 shows a PL spectrum of dislocated silicon at 80 K.

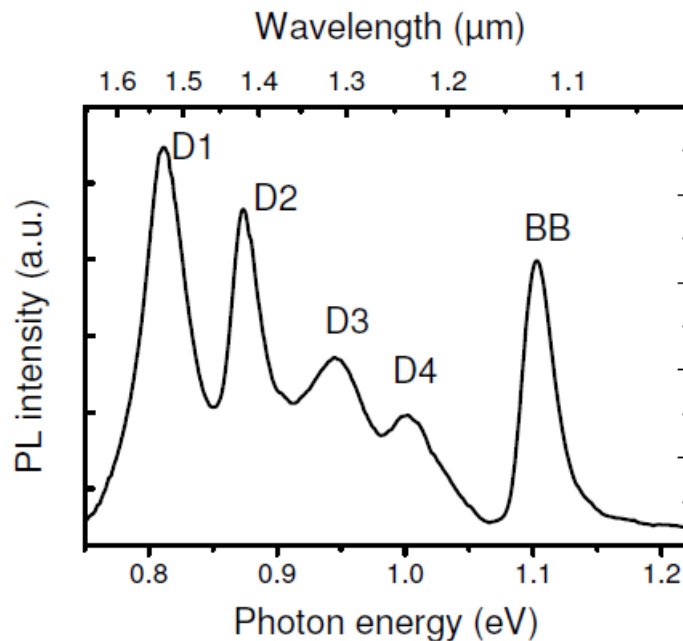


**Figure 1.2.2.2:** PL spectrum of a dislocated silicon made by plastic deformation at 80 K. All four D-lines and the BB line are clearly visible [Arg2007a]

## 1. Basic knowledge

There one can see four peaks (D1 - D4) besides the BB peak. These peaks are called D-lines or dislocation-related lines. Drozdov et al. firstly reported them and their spectral positions at helium temperature: D1 (0.812 eV), D2 (0.875 eV), D3 (0.934 eV) and D4 (1.0eV) [Dro1976].

Despite of many studies with several techniques the exact mechanisms of the D-lines is still unknown. One possible reason is that they are formed due to the strain field caused by lattice distortion around the dislocation, structural defects at the dislocation or due to impurity atoms captured at the dislocation strain field. Following the strain-field idea, an approach of explanation assumes long-range strain fields around dislocations. These strain-fields are independent on the structure of the dislocation core or its decoration by impurities. Such strain fields could form one-dimensional energy bands, which are related to the Burgers vector of the dislocation [Lel1992]:

$$E = E_g - A \left( \frac{b_e}{a} \right)^2 \quad (1.2.2.3)$$

, where  $E$  is the energy of the emitted radiation,  $E_g$  the bandgap energy,  $a$  the lattice constant,  $A$  is a constant accounting for the deformation potential and the effective mass of the charge carriers and  $b_e$  is the edge component of the Burgers vector of the dislocation. Modifications of the bandgap for selected types of dislocation show quiet good agreements with the observed spectral positions of D-lines. This was confirmed from theoretical point of view [Lel1992] as well as from the experimental one [Sek1994, Sek1996]. A comparison of such studies is summarized in table 1.2.2.1. Further correlation between luminescence features and dislocation types have been found. For instance, D1 and D2 are dominant in regions of intersecting slip lines. In contrast to that, D3 and D4 are dominant along glide dislocations [Sek1994, Sek1996]. Relations between D1-D4 and relaxed dislocations [Sau1985], between D1-D2 and screw dislocations, D3-D4 and edge dislocations have been found as well [Mch2009].

Dislocation type	$b_e/a$	Calculated E [eV]	Observed E [eV]
Screw non-split	1/2 [110]	/	/
30° partial glide	1/6 [211]	1.14	/
Stair-rod partials	1/6 [110]	1.125	1.023
90° partial glide	1/6 [112]	1.04	1.013
Frank partial	1/3 [111]	0.9	0.87 (D2)
60° non-split	1/2 [101]	0.87	0.84
Lomer-Cottrell	1/2 [110]	0.77	0.808 (D1)

**Table 1.2.2.1:** Comparison of calculated and experimentally observed luminescence in one-dimensional band gap, formed due to the strain field of dislocations [Lel1992].

## Role of impurities

Impurities are an unavoidable part of silicon. One of the main differences between various material qualities is the amount and the type of impurities. They can be roughly classified in two groups: transition metals and non-metallic impurities. Non-metallic impurities contain desired dopants (e.g. phosphorus) as well as undesired impurities (e.g. oxygen), which become embedded in the crystal lattice during the crystallization/growth process.

### Transition metals

Important transition metals in silicon are Cu, Ni, Fe, Ti, Au etc. Their contamination can influence the radiative recombination activity at dislocations drastically. Some transition metals like copper, iron or nickel have an affinity to decorate dislocations and grain boundaries in mc-Si and increase their electrical activity [McH1993, Hig1993, Kit1993]. Kveder et al. [Kve2001] developed a model of the transitions between traps within the bandgap and conduction or valence band. The impact of transition metals was studied on selectively contaminated dislocations formed by epitaxially grown stacking faults [Hig1992]. Thereby a characteristic maximum intensity of D1 and D2 luminescence was observed at specific concentrations. The decrease of luminescence intensity was related to the beginning formation of precipitates. That marks the fluent change from dislocation-related luminescence to luminescence related by precipitates. An example for copper is given for copper in figure 1.2.2.3. The appearance of such an optimum is typical for most of the transition metals. There are different theories about the interaction between transition metals and dislocations. One approach of explanation assumes that metals passivate non-radiate recombination centers at the dislocation. This leads to an increase of DRL [Sek1994]. But this approach is not totally convincing, because of metallic-free dislocations do not show higher total recombination than slightly contaminated ones [Hig1993].

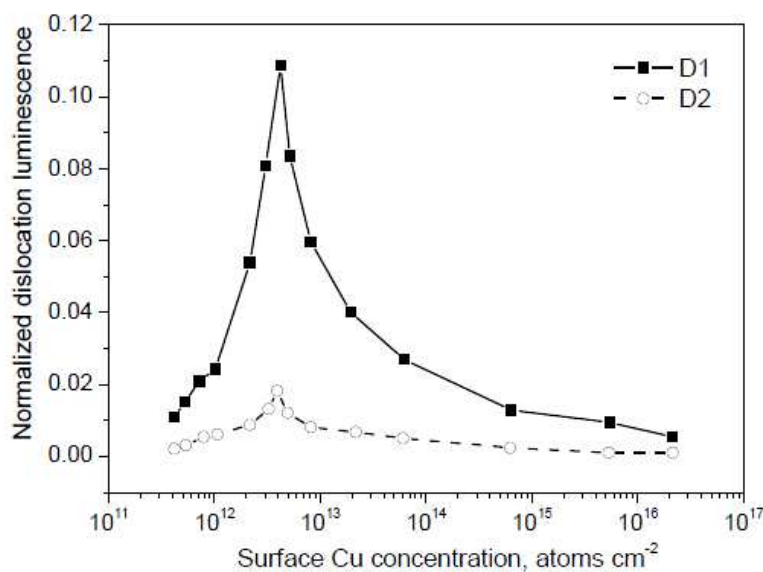


**Figure 1.2.2.3:** Dependence of D1 and D2 intensities on surface concentration of Cu: The dislocation luminescence peaks are normalized on the phosphorous bound-exciton peak, which appears close to BB in the spectra. The Cu contamination was controllably introduced onto the sample surface [Hig1992].

## 1. Basic knowledge

The impact of contamination was studied by EBIC, where the EBIC contrast reflects the recombination activity of dislocations. Thereby the recombination activity depends on the temperature of the sample and the concentration of excited minority carriers. This dependence is characterized by the EBIC contrast as function of the temperature and beam current. These investigations exhibit strong interaction of the dislocations with impurities. This was shown by studies of the transition metal contamination of the dislocations leading to distinct temperature behaviors of the EBIC contrast [Kit1995, Kit1995a].

Kveder et al. [Kve2001] developed a model to describe the interactions between dislocations and metals, whereas a strong coupling between impurity level and one-dimensional dislocation bands is used to describe the recombination. It must be emphasized that the model is more complex than just a simple SRH recombination process. It assumes a balance between carrier exchange and recombination between dislocation bands and levels formed by metal impurities.

### **Oxide precipitates**

The relation between oxide precipitates (OP's) and DRL was initially pointed out by Drozdov et al. [Dro1981]. They showed that the D1 line broadens at dislocations formed on oxygen atmosphere. Note that most studies about oxygen-related luminescence were performed on Float zone (FZ-Si) or Czochralski Si (Cz-Si).

The formation of OP's in silicon starts with homogeneous nucleation and is affected by the presence of vacancies at around 450 °C. In a next step oxygen starts to agglomerate during the temperature treatment, resulting in the formation of so-called 'thermal donors' (TD's). Several types of TD's can be formed due to several temperatures and times of treatment. Besides these TD's other oxygen-related luminescence features have been observed. The most prominent one is the P-line at 0.767 eV at around 10 K [Piz2000], among many distinct lines [Kür1989]. Further temperature treatment leads to the appearance of broader peaks between 0.7 eV and 0.95 eV [Bin2002] instead of the sharp lines. Tajima et al. suggested following approach of explanation for this behavior on the example of the P-line: The 0.767 eV PL defect is an intermediate state of oxygen agglomeration between the TD's and extended oxygen complexes [Taj1994]. At temperatures, significantly about 450 °C it can be assumed that almost all TD's are transformed into more or less complex oxygen complexes.

In mc-Si, it is often very difficult to separate luminescence features caused by dislocations (mainly D1) and those caused by OP's. Nevertheless, two points can be used as good evidence for the participation of OP's. The first one is luminescence, which is clearly redshifted (~ 0.77 eV), especially at room temperature [Taj1992]. The other evidence for OP's is an unusual broadening of the luminescence signals in the interesting spectral range. Another important point of mc-Si is the affinity of oxide precipitates to be gettered by dislocations [Cav1993].

## **Properties and behaviors of defect-related luminescence (DRL)**

The complete origin of DRL is still unknown. However, typical properties and behaviors depending on external parameters, such as temperature, excitation power etc. were observed. D1 and D2 respectively D3 and D4 are commonly considered as pairs, because of their similar behaviors upon external parameters. This similarity does not mean that they have the same origin urgently. However, it denotes any relation between the two lines of a pair.

### **Energy shift upon application of uniaxial stress**

The shift of the peak position upon externally applied uni-axial stress gives information about the symmetry of the radiative centers and their piezo-optical constant. For instance, compression of samples along the  $\langle 111 \rangle$ ,  $\langle 110 \rangle$  and  $\langle 100 \rangle$  crystallographic directions leads to redshifts in case of D3 and D4 and blue shifts in contrast to that D1 and D2 [Dro1977]. Another stress-related feature is the splitting of D1 and D2 into two components each [Sue1982, Sue1983], whereas both components have different sign of their piezo-optical constants. A centre with tetragonal symmetry, responsible for the D1 and D2 emission, could explain this.

### **Radiative decay times**

Fukatsu et al. [Fuk1996] did one of the rare studies about the radiative decay times on dislocated undoped SiGe alloy layers. They found out that all four D-lines decay in the nanosecond range of time. The decay times at 9 K, indicate a pairing of D1 and D2 (~ 200 ns) and D3 and D4 (~ 60 ns), again. The temperature dependence of decay times show a decrease with increasing temperature for D1 and D2, but almost constant decay times for D3 and D4.

### **Dependence on the excitation power**

The dependence of defect luminescence intensity on the excitation/generation of excess carriers differs from that one of BB luminescence intensity. In case of BB, the intensity behaves linear in low injection regime and quadratic in high injection regime (see: sub-chapter 1.1). In contrast to that D1 and D2 exhibit sub-linear dependence on excitation level and at higher temperatures the intensities saturates actually. D3 and D4 exhibit almost linear behavior [Sue1983a].

### **Temperature dependence of dislocation-related luminescence**

Two models were developed to describe the temperature behavior of DRL, the ‘bound-to-free’ and the ‘bound-to-bound’ deactivation models. These models describe the deactivation

## 1. Basic knowledge

of a carrier trapped at a radiative centre in a semiconductor three-dimensional band or in another bound state, respectively (Fig. 1.2.2.4).

The bound-to-free model assumes two non-degenerated levels at dislocations, one shallow trap occupied with electrons and one deep trap occupied with holes. Injection of carriers leads to non-thermal equilibrium conditions. The occupation can be described by quasi-Fermi levels. Further assumptions are that the quasi-Fermi levels  $F_n$  and  $F_p$  are close to the valence and conduction band and a trap level  $E_T$  is close to  $F_n$  (Fig. 1.2.2.4(a)).

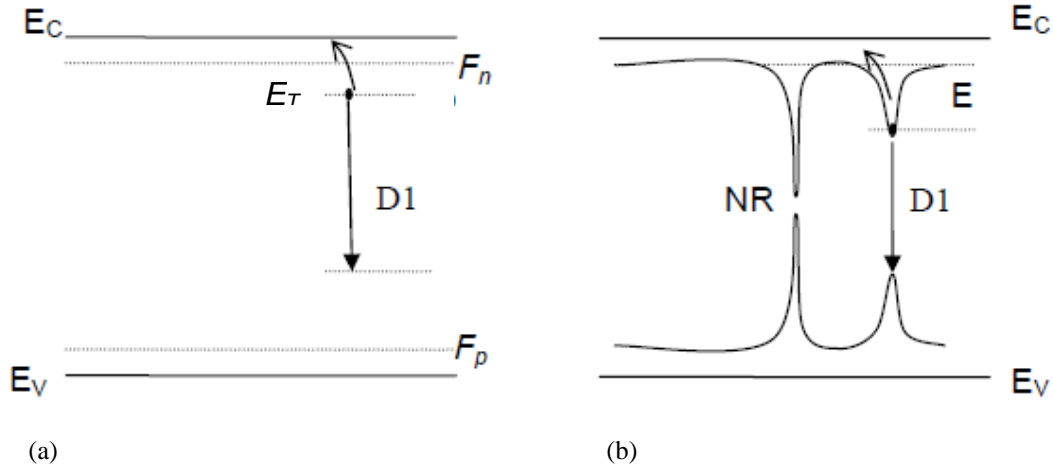


**Figure 1.2.2.4:** Models to describe temperature behavior of DRL: bound-to-free model (a); bound-to-bound model (b). Image taken from [Arg2007a]

Then the occupation can be described by:

$$f = \frac{1}{1 + \exp\left[\frac{E_T - F_n}{kT}\right]} \quad (1.2.2.4)$$

The electron density  $n$  in the conduction band, generated due to excitation close to the trap, related to the Fermi level is given by:

$$n = N_C \exp\left[\frac{F_n - E_C}{kT}\right] \quad (1.2.2.5)$$

where,  $N_C$  is the effective density of states in the conduction band. Considering its temperature dependence ( $N_C = N_{C0} * T^{3/2}$ ) equations (1.2.2.4) and (1.2.2.5) can be combined to:

$$f = \frac{1}{1 + \left(\frac{N_{C0}}{n}\right) T^{3/2} \exp\left[\frac{E_T - E_C}{kT}\right]} \quad (1.2.2.6)$$

The substitutions  $E_d = -(E_T - E_C)$  and  $C = N_{C0}/n$  leads to an expression of the luminescence intensity  $I(T)$  at temperature  $T$  relative to the intensity  $I(0)$  extrapolated to 0 K [Sue1983a]:



## 1. Basic knowledge

$$\frac{I(T)}{I(0)} = \frac{1}{1 + CT^{3/2} \exp[-E_d / kT]} \quad (1.2.2.7)$$

The important parameter is the deactivation energy  $E_d$ . In the model, it describes the energy barrier between the trap level  $E_T$  and the conduction band. In realistic materials, the deactivation energy is the barrier between the occupied level and an unknown level above. This can be another trap level or the conduction band.

In contrast to the bound-to-free model, the bound-to-bound model assumes the vicinity of a radiative defect states and a non-radiative states [Sau1985, Pan1975]. Under such conditions electron-hole pairs can recombine by emitting of multi-phonons or auger process. So the model describes the recombination probability of two rivaling processes: radiative and non-radiative. That is illustrated in figure 1.2.2.4(b). A carrier is captured at a trap responsible for radiative recombination (e.g. D1). A deactivation of this trap is possible if the carrier overcomes the energy barrier  $E_d$  to the non-radiative trap (NR). The temperature independent probability  $P_{nr}$  for this transition is give by:

$$P_{nr} = P \exp[-E_d / kT] \quad (1.2.2.8)$$

where  $P$  is the non-radiative decay probability. Assuming that the radiative recombination probability  $P_r$  is also independent on temperature, then the intensity ratio is given by:

$$\frac{I(T)}{I(0)} = \frac{P_r}{P_{nr} + P_r} = \frac{1}{1 + C \exp[-E_d / kT]} \quad (1.2.2.9)$$

where  $C$  is a constant, accounting for the radiative and non-radiative transition probabilities, and  $E_d$  is the deactivation energy of a radiative traps.

Studies of the deactivation energies obtained values of about 165 meV for D1 and 95 meV for D4 in heavily dislocated Si [Kve1995, Kve1996]. Although most studies (e.g. [Sue1983a]) found similar temperature dependences of D1 and D2 on the one side and D3 and D4 on the other side, there are contrary results. Such as, Sauer et al. [Sau1985] found that D1 and D3 remain virtually constant up to 20 K, while D2 and D4 showed a gradual decrease.

### **Spatial distribution**

The spatial distribution was investigated by high-resolution cathodoluminescence measurements. Thereby D3 and D4 appear at the dislocation core. D1 and D2 appear in the vicinity. Vicinity means a distance of 2 – 9  $\mu\text{m}$  [Hig1992a, Sek1996], which is not detectable by the PL setup used in this work. Therefore, BB luminescence and DRL should exhibit a spatial anti-correlation. If this is not the case, other reasons, such as gettering, must be discussed.

### **Addition D-lines in non-relaxed dislocations**

Other lines D5 (0.953 eV), D6 (1.0126 eV) and D12 (0.8443 eV) were associated with dislocations, too [Sau1985]. They were attributed to non-relaxed dislocations, produced by two-step deformation. These additional D-lines were generated by extended temperature treatments of FZ silicon samples. However, it is sufficient to focus on the dislocation-related peaks D1 – D4 during analysis of luminescence spectra. Other D-lines might be a possible misunderstanding of spectral shifts due to stress etc.

### **Phonon replica relation between D3-D4**

The correlation between D1 - D2 and between D3 – D4 has been observed in many studies of various parameters. Therefore, D3 is considered to be TO phonon replica of D4, whereas the larger peak width of D3 in comparison to D4 is explained by the small energy differences between the three, momentum conserving TO phonons [Wor1992]. Such close relation was not observed between D1 and D2, despite of similar behaviors.

### **Summary**

The defect-related luminescence (DRL) consists of D-lines (D1-D4), which are related to dislocations and other luminescence features, which are related to precipitates (e.g. oxygen). The luminescence properties (peak position, peak width, etc.) are affected by several external parameters (stress, temperature, contamination, etc.). D3 and D4 are generated by transition between one-dimensional dislocation bands on 60° dislocations. D3 is a phonon replica of D4. Contrary to this, the exact origin of D1 and D2 is still unknown, but they are most probably caused by the interaction of the dislocations with background metallic impurities. D1 and D2 are related in any way, too.

## **1.3 Basic material properties of silicon phases in thin-film solar cells - a-Si:H, $\mu$ c-Si:H and c-Si**

In this sub-chapter the basic structural and optical properties of amorphous (a-Si:H) and microcrystalline silicon ( $\mu$ c-Si:H) are discussed and compared with those of crystalline silicon (c-Si). Note that both Si phases become hydrogenated for photovoltaic applications to passivate the dangling bonds.

## Structural properties

### Crystalline Silicon (c-Si):

Crystalline silicon is a very general term for silicon with grain sizes above a few micrometres. That includes monocrystalline silicon (Cz-Si, FZ-Si) and multicrystalline silicon (mc-Si). Of course, they are distinguished by defect concentrations, such as grain boundaries. However, for this overview the optical and structural properties can be considered as equal. Crystalline silicon has a diamond lattice structure with a bond length of  $2.35 \text{ \AA}$  and a covalent bond angle of  $109^\circ$ . Further information can be found in [Sze1981]. The well-known band structure of c-Si was already shown (see: figure 1.2.1(b)). The ordered lattice structure is responsible for the presence of a well-defined and abrupt bandgap of about  $1.12 \text{ eV}$  in crystalline silicon at room temperature.

### Amorphous Silicon (a-Si:H):

The main difference between amorphous and crystalline silicon is the structural disorder, which is characterized by enormous deviations in bond length and bond angle. That results in the presence of localized states close to conduction and valence band of a-Si:H, called 'tail states' [Ove1989]. The range of the band tails, in a-Si:H, is about  $0.2 \text{ eV}$  (conduction band tail) and  $0.3 \text{ eV} - 0.4 \text{ eV}$  (valence band tail) [Stu1987]. The term tail states originates from the broadening/enhancement of the bandgap visible in absorption measurements (see: Fig. 1.3.3). These tail states differ from defect states in c-Si, causing SRH-recombination, because of their high density and energetically broadening. They can be described as bands and/or tails of the regular conduction and valence bands.

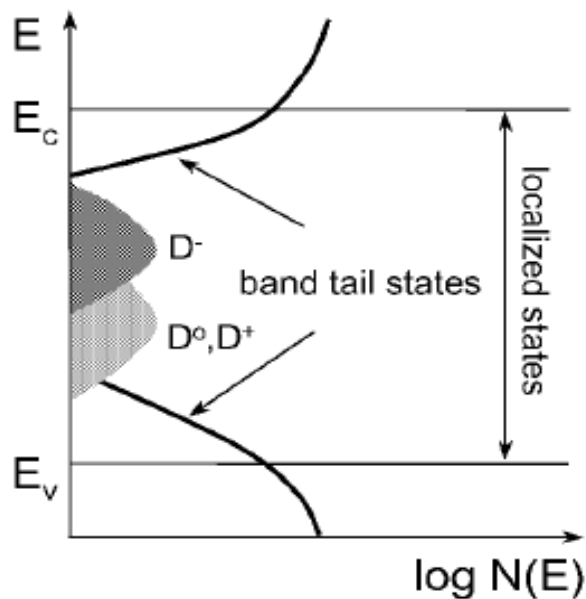


**Figure 1.3.1:** Sketch of the density of states diagram of a-Si:H: Band tail states are localized close to the conduction and valence band, differently charged defect states ( $D^-$ ,  $D^0$  and  $D^+$ ) are localized in the middle of the bandgap. (Image taken from [Mer2005])

## 1. Basic knowledge

It is very important that these states lead to a partially relaxation of the momentum conservation. Therefore, radiative recombination becomes much more probable than in c-Si. To emphasize this fact a-Si:H is also called ‘quasi-direct semiconductor’. Of course, defect states in the middle of the bandgap are still present. These defect states are also characterized by a significant broadening. All states are illustrated as a distribution of the density of states  $N(E)$  in figure 1.3.1. The charged defect states  $D^-$ ,  $D^0$  and  $D^+$ , in the middle of the bandgap, might be caused by dangling bonds and have to be saturated by hydrogen passivation to improve the electrical properties. Due to the tails states it is not so easy to determine an exact definition of the bandgap. It can be estimated to 1.6 eV – 1.8 eV, larger than the bandgap in c-Si. Another important property of a-Si:H is the high absorption coefficient, which makes it interesting for thin-film solar cell applications. It allows efficient absorption of the entire solar spectrum in films with a thickness of around one  $\mu\text{m}$ .

### Microcrystalline Silicon ( $\mu\text{c-Si:H}$ ):

Microcrystalline silicon represents a junction/transition between amorphous and crystalline silicon, but it is rather comparable to c-Si than a-Si:H. Exact statements about its properties are complicated by the fact that they are strongly dependent on the deposition conditions, e.g. ratio of silane to hydrogen, substrate temperature, etc. Several studies were published dealing with these dependences on the structural, electrical and optical properties of  $\mu\text{c-Si:H}$  [Car 1997, Fin1997].

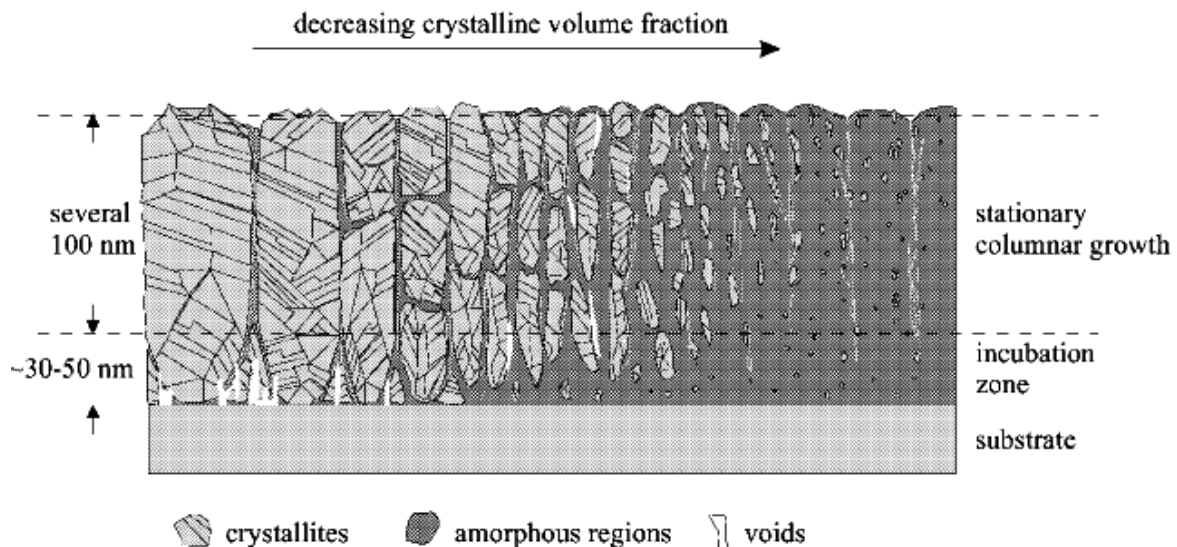


**Figure 1.3.2:** Sketch of the structure of microcrystalline silicon grown by high frequency PECVD. From the left to the right, the film composition changes from crystalline to highly amorphous regions. (Image taken from [Vet2000])

Combined techniques, such as transmission electron microscopy (TEM), Raman spectroscopy and X-ray diffraction (XRD), were used to develop a model of the structure of  $\mu\text{c-Si:H}$ . Figure 1.3.2 shows an image, which illustrates a widely-accepted model of  $\mu\text{c-Si:H}$ . One of the main key-parameters for the deposition of  $\mu\text{c-Si:H}$  is the silane concentration.

## 1. Basic knowledge

Simplified it can be said: the lower the silane concentration the higher the crystalline fraction of  $\mu\text{c-Si:H}$ . Under crystalline growth conditions, the deposited films consist of columnar clusters of smaller grains with coherent crystalline regions (left side of Figure 1.3.2). Amorphous regions or regions of voids separate the columns from each other. Tzolov et al. found out that the exact composition depends on the deposition conditions and the substrate properties [Tzo1997]. In strongly amorphous regions, silicon crystals can be described as nanocrystalline isles within an a-Si:H matrix (right side of Figure 1.3.2). It is important to emphasize that the grain size of  $\mu\text{c-Si:H}$  crystals (10 nm - 30 nm) do not increase significantly with increasing crystallinity. The single crystals start to agglomerate to columns with a size of several hundred nanometers [Luy1997, Hou1998]. High densities of twin boundaries and stacking faults are typical for the columns.

### Optical Properties of a-Si:H, $\mu\text{c-Si:H}$ and c-Si

The optical absorption spectra of all three silicon phases are shown in figure 1.3.3. At high photon energies  $h\nu > 1.8$  eV the absorption of a-Si:H is much higher than in c-Si. The absorption of  $\mu\text{c-Si:H}$  is between both, caused by absorption in a-Si:H regions and/or internal light scattering in the  $\mu\text{c-Si:H}$  phase [Die1998]. At middle photon energies (1.1 eV - 1.8 eV)  $\mu\text{c-Si:H}$  behaves quite similar to c-Si, while the absorption of a-Si:H drops drastically with decreasing energies. The critical photon energy is at 1.1 eV, the bandgap of c-Si. It exhibits an abrupt drop of the absorption coefficient, caused by the well-defined conduction and valence band. But the absorption spectra of a-Si:H and  $\mu\text{c-Si:H}$  exhibit tail states. These are clearly visible by the non-vanishing absorption coefficients at photon energies below 1.1 eV. Thereby the tail states in a-Si:H are more distinctive than in  $\mu\text{c-Si:H}$ .

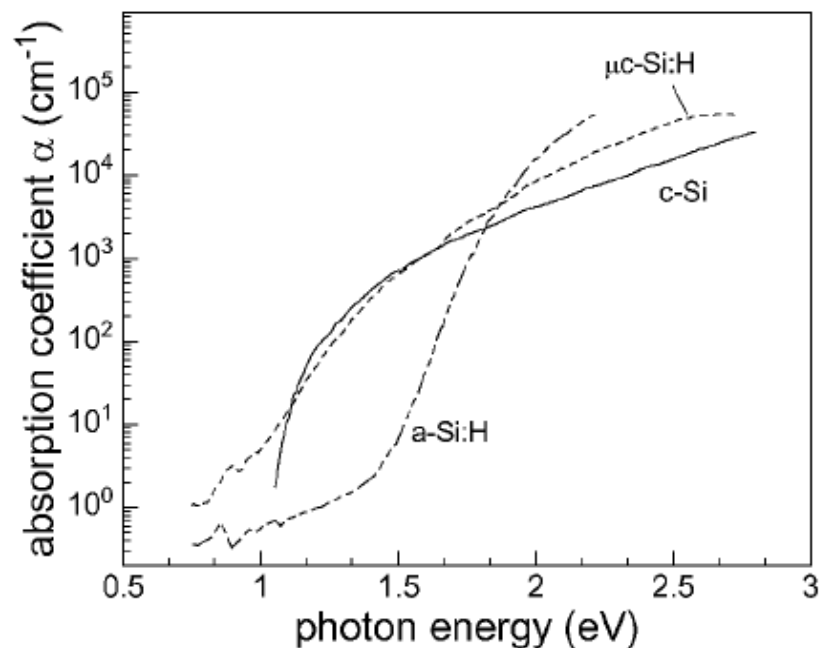


**Figure 1.3.3:** Absorption coefficient  $\alpha$  of crystalline silicon (c-Si), hydrogenated amorphous silicon (a-Si:H) and microcrystalline silicon ( $\mu\text{c-Si:H}$ ) measured by photothermal deflection spectroscopy (PDS). (Image taken from [Mer2005])

### Luminescence from a-Si:H, $\mu\text{c-Si:H}$ and c-Si

In principle, generation and recombination processes in a-Si:H and  $\mu\text{c-Si:H}$  are the same as in other semiconductors (see: sub-chapter 1.2). In a-Si:H and  $\mu\text{c-Si:H}$  three different thermalisation processes can be distinguished. The first one is thermalisation by phonon emission happening in less than  $10^{-12}$  s. The second one is thermalisation by tunneling between localized states (hopping down) occurs at low temperature [Str1981]. The last thermalisation process appears by multiple trapping mechanisms [Ore1981]. Note that thermalisation ends in the tail state and not at the conduction band minimum.

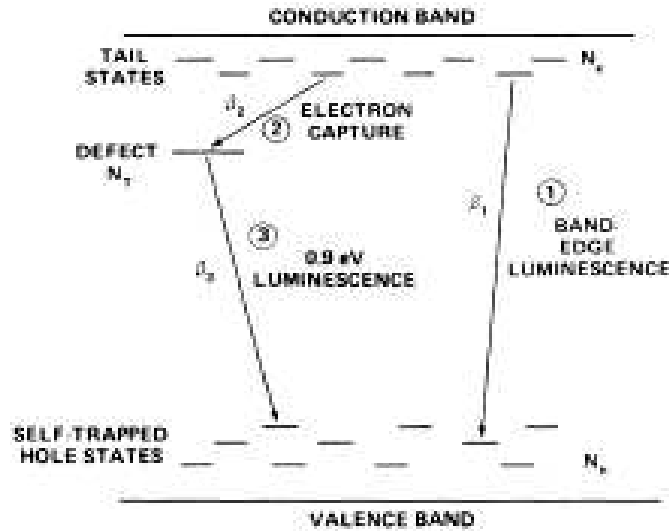


**Figure 1.3.4:** Sketch of the band diagram of a-Si:H ( $\mu\text{c-Si:H}$  is very similar, but tail states are less distinctive). Possible recombination paths are shown. (Image taken from [Str1980])

Next, the carrier can recombine by two main radiative recombination paths. The first one is radiative transition between tail states of conduction and valence band ((1) in figure 1.3.4). The second one is a non-radiative transition from the tail states to defect states in the middle of the bandgap ((2) in figure 1.3.4). From these defect state radiative transition is possible again ((3) in figure 1.3.4).

First photoluminescence measurements on a-Si:H were performed by [Eng1973]. Street et al. [Str1980, Str1981] performed studies that are more extensive. Thereby two peaks were distinguished. In amorphous silicon, the dominant radiative recombination mechanism at low temperature and low defect density is the radiative transition between localized tail states at around 1.2 eV – 1.4 eV ((1) in figure 1.3.4). At higher temperatures defect-related luminescence at about 0.9 eV ((3) in figure 1.3.4) becomes more important.

Peak energy and peak width of PL spectra contain a large amount of information about the occupation and energy position of electronic states. Although this information is not easily available especially in disordered system, such as a-Si:H and  $\mu\text{c-Si:H}$ . Exact statements about the peak width require very low temperatures ( $\sim 10$  K) to avoid thermally activated non-radiative transitions. Only at these conditions the peak width can be used to extract information about the electrical broadening of the states due to disorders in the crystal lattice, like in a-Si:H or  $\mu\text{c-Si:H}$ . At higher temperatures, such statements are just qualitatively.

## 1. Basic knowledge

Figure 1.3.5 shows a slightly simplified composition of typical PL spectra measured on a-Si:H,  $\mu\text{c-Si:H}$  and c-Si at low temperatures of 10 K – 20 K.

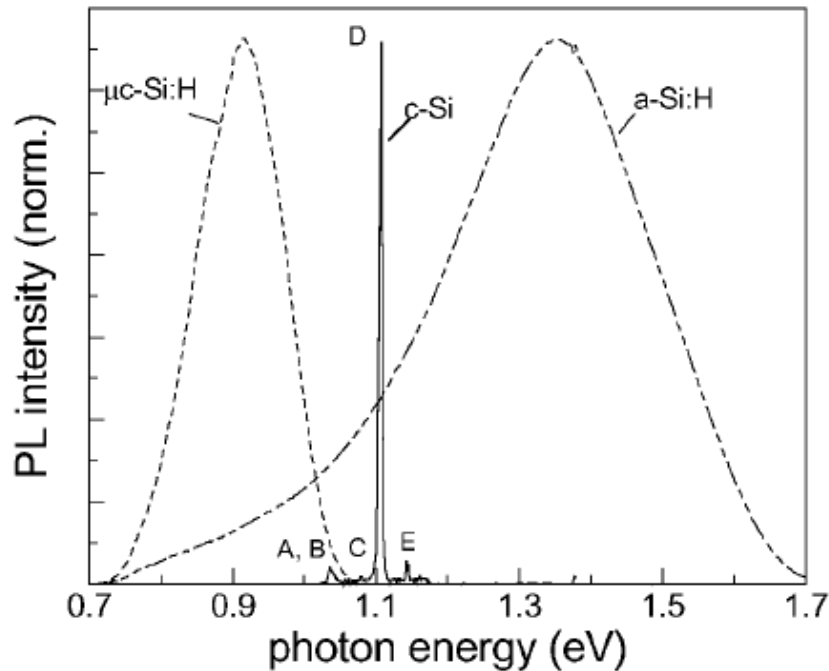


**Figure 1.3.5:** Comparison of PL spectra of crystalline (c-Si), hydrogenated amorphous (a-Si:H) and microcrystalline ( $\mu\text{c-Si:H}$ ) silicon: PL spectra of a-Si:H and  $\mu\text{c-Si:H}$  films are excited by energy of 2.54 eV at 10 K. The PL spectrum of c-Si was excited by a mercury arc at 18 K and is taken from [Var1967]. (Image taken from [Mer2005])

Crystalline silicon is characterized by an abrupt bandgap leading to a very sharp luminescence peak in PL. Several phonon participations are possible and labeled by the letters A – E, because of the indirect transition. D is the most probable band-to-band transition at about 1.1 eV. It is equal to the transverse optical (TO) phonon emission, originating from bound exciton recombination. The further phonon transitions are discussed in [Sau1985].

In a-Si:H a very broad peak between 1.25 eV and 1.4 eV is observed at low temperatures. The exact peak energy varies depending on the deposition conditions. The peak broadening is caused by the disorder in a-Si:H and is one of the most characteristic features of a-Si:H tail states. The peak form exhibits an asymmetry due to defect-related luminescence at around 0.9 eV. The defect related emission is also shows an enormous peak width. It is especially observed in doped a-Si:H and in materials with high defect densities. In contrast to the tail state peak, it is dominant at room temperature.

PL spectra of  $\mu\text{c-Si:H}$  are strongly dependent on deposition conditions (e.g. substrate parameters, layer thickness etc.). That means that almost every single publication reports different PL spectra. For that reason, this overview can just summarize some very typical features in  $\mu\text{c-Si:H}$ . A broad PL peak is observed in the range of tail states of a-Si:H (1.2 - 1.3 eV) [Bha1983]. This peak is not surprising because it is related to the remaining amorphous phase in  $\mu\text{c-Si:H}$ . Often the peak width is slightly lower than that one of a-Si:H. A second typical PL peak is detected around 0.9 eV - 1.05 eV at low temperatures. It is probably related to transitions between tail states in the microcrystalline phase. This is shown in figure 1.3.5.

## 1. Basic knowledge

Additional to these more or less typical luminescence signals further peaks were observed depending on the deposition conditions of the  $\mu\text{c-Si:H}$  films. The spectral range of these peaks reaches from around 0.45 eV to 1.7 eV. Physical interpretation of these various peaks differ from defect-related luminescence [Mer2006] via widening of optical bandgap and narrowing of band tails by hydrogen dilution in a-Si:H [Yue1999] through to terms of quantum size effects [Kaa2000].

It makes no sense to discuss all these approaches here, because of the enormous impact of deposition conditions. Therefore, a sufficient comparability between them is rather improbable. But it should be emphasized that the interpretation of  $\mu\text{c-Si:H}$  spectra is more complicated than in a-Si:H or c-Si due to this complicated dependences on deposition conditions.

### 1.4 Overview of thin-film solar cells technologies

Since decades, photovoltaic market has been dominated by solar cell concepts based on silicon wafers of bulk thickness. Thin-film concepts have the potential to capture their own place on market due to the high pressure in cost minimization.

Thin-film technologies can be distinguished into two main classes. One bases on several silicon phases (a-Si:H,  $\mu\text{c-Si:H}$ , c-Si) and the other one bases on polycrystalline chalcogenide compounds (CdTe, CIS, etc.). Other thin-film technologies can be summarized in a third class, including upcoming technologies like organic solar cells.

Cell type	Area [cm <sup>2</sup> ]	V <sub>OC</sub> [mV]	I <sub>SC</sub> [mA/cm <sup>2</sup> ]	FF [%]	Best known efficiency [%]
<b>Bulk cells</b>					
mono-Si	4	706	42.7	82.8	25
mc-Si	~ 1	664	38	80.9	20.4
<b>Thin-film cells</b>					
<b>Si based</b>					
a-Si:H	~ 1	886	76.75	67	10.1
$\mu\text{c-Si:H}$	~ 1	539	24.4	76.6	10.1
a-Si:H/ $\mu\text{c-Si:H}$	~ 1	1365	12.93	69.4	12.3
<b>Chalcogenide</b>					
CIS / CIGS	~ 1	713	34.8	79.2	19.6
CdTe	~ 1	845	26.1	75.5	16.7
<b>Others</b>					
DSSC	~ 1	714	21.93	70.3	11
Organic	~ 1	899	16.75	66.1	10

**Table 1.4.1:** Overview of several record parameters for the most important solar cell technologies; data extracted from [Gre2012].



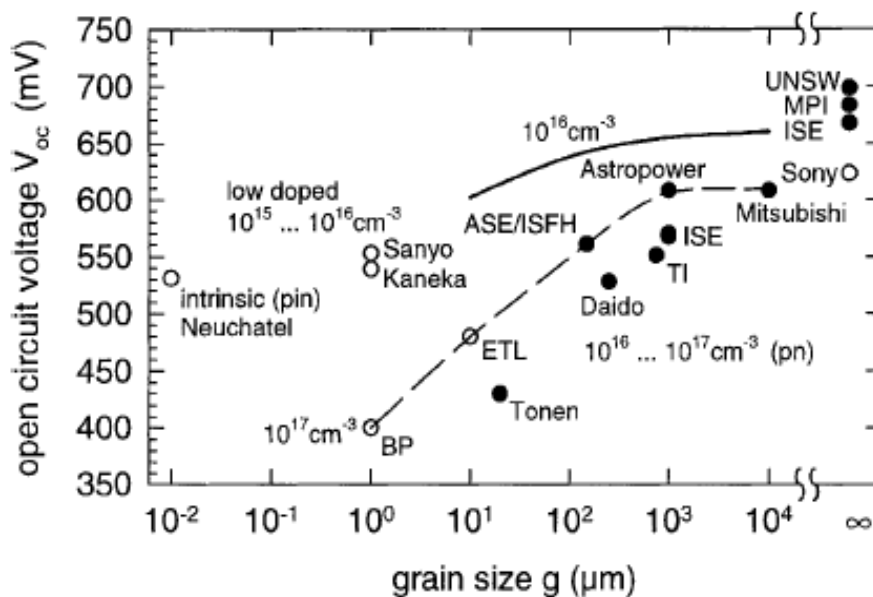
## 1. Basic knowledge

Table 1.4.1 gives an overview of the most important thin-film technologies in comparison with established wafer based bulk cells. Note that the reported record values differ from those measured on stabilized large-scale modules.

The different silicon phases, which are used for thin-film solar cells, were presented in the previous sub-chapter focusing on material aspects. In this chapter, the focus will be on the applications for Si photovoltaic. In an intermediate step, the relation between the materials and the cell concepts will be discussed. Thereby the term relation refers to the different deposition and crystallization processes of Si, which leads to different phases. These distinct phases require distinct solar cell technologies. Finally, complete solar cell technologies will be presented in the sub-chapters 1.4.1 and 1.4.2. Other thin-film technologies will be presented very shortly, to give a general overview.

### Classification of Si thin films

A classification of Si based thin-film solar cells can be done according to the grain size  $g$ . That is one of the most important parameter of thin-film solar cells, because of its enormous influence on electrical structure (p-n or p-i-n junction), diffusion length, deposition temperatures etc. A simplified relation between grain size  $g$  and possible efficiency is shown in figure 1.4.1, where the open circuit voltage  $V_{OC}$  is used as indicator for the efficiency.



**Figure 1.4.1:** Open-circuit voltage  $V_{OC}$  of thin-film Si solar cells as function of grain size  $g$ :  $V_{OC}$  rapidly decreases with grain size, experimentally (dashed line) as well as predicted from fit of diffusion length data based on cast Si (solid line) (image taken from [Ber1999]).

No Si grains:

These solar cells totally consist of amorphous silicon and require a p-i-n junction within the cell structure. They are characterized by easy and cheap production costs (simple CVD deposition) and low stabilized large-scale efficiencies between 5 and 10 %.

## 1. Basic knowledge

Small-grained Si with  $g \ll 1$  mm:

These grain sizes include nc-Si:H and  $\mu\text{c-Si:H}$ . Thereby a clear separation of both is not possible considering the fact that  $\mu\text{c-Si:H}$  consists of nanocrystalline Si (see: sub-chapter 1.3). However, both terms deal with grain sizes of around 10 nm. Solar cells made by these materials base on intrinsic or moderately doped absorber and need a p-i-n junction with built-in drift field for carrier separation. The advantages of this material are the low deposition temperature of around 450 °C and the lower affinity for light-induced degradation.

Silicon with grain sizes in the order of a few micrometres does not need the p-i-n junction urgently. In those cases, a simple p-n junction is sufficient. The material is also called poly-Si. It is often obtained by subsequent crystallization of amorphous or nanocrystalline silicon. The crystallization can be induced by thermal treatment [Ols1988] or irradiation (e.g. laser-induced [Mch2011], electron-beam induced [Lul1987]).

Large-grained Si with  $g \sim 1$  mm:

This type of silicon is called large-grained Si. It is also produced by subsequent crystallization of a-Si:H or nc-Si:H. Such cells use higher doped ( $10^{15} - 10^{16} \text{ cm}^{-3}$ ) absorbers and thus employ p-n junction to separate free carriers. It can be deposited on several glasses [Feh1997] or metal films [Mat1996] in a temperature range of 450 °C – 700 °C.

Very large-grained Si with  $g > 1$ mm:

Such grain sizes are typical for mc-Si or mono-Si and require p-n junction. The material crystallizes in high temperature processes above 800 °C. The formation of mono-Si thin-films is a special case and need a transformation steps (e.g. growing on mono-Si substrate transferred to foreign substrate). It should be emphasized that mono-Si thin films are characterized by high costs. This is contrary to the desired price reduction.

### 1.4.1 Silicon based thin-film technologies

#### Single-junction amorphous silicon (SJ a-Si:H)

Usually amorphous silicon is deposited by CVD (chemical vapor deposition) of a gas mixture containing silane ( $\text{SiH}_4$ ). Thereby two different deposition mechanisms are commonly used: plasma-enhanced-CVD (PECVD) [Wro2001] and hot wire CVD (HWCVD) [Ami2004]. The advantage of these technologies is the incorporation of about 10 % (atomic) hydrogen, whereas the hydrogen passivates the dangling bonds of a-Si:H. That leads to a significant improvement of the electronic properties [Gre2003]. The high absorption coefficient allows the absorption of the incident sunlight in almost one micrometer. A disadvantage is the light-induced degradation (LID), e.g. Staebler-Wronski effect [Sta1977]. One of the properties, which are affected by LID, is the low carrier mobility. Therefore the structure of a-Si:H solar cells differ from crystalline bulk ones in two points [Gre2003]. At first, free carriers are generated in the electric field of a p-i-n junction. This is used to aid the collection of excess carrier. Therefore, the light-induced generation must be localized in the intrinsic layer. The second difference is the use of a transparent conducting oxide (TCO) on the front side, e.g.

## 1. Basic knowledge

$\text{SnO}_2$ . The TCO is necessary to allow lateral flow of carriers. Otherwise, the low mobility and the small thicknesses of the p-layer would lead to a very low conductivity. A sketch of such single-junction a-Si:H cell is shown in figure 1.4.1.1. Such cells are equipped with surface texture [Lec2002] for light trapping. The main advantages of these cells are the very low material costs and the simplicity of the technology. For example, it is possible to deposit large glass sheets automatically interconnected during deposition. The main disadvantage is the quite low stabilized module efficiency of around 5 %.

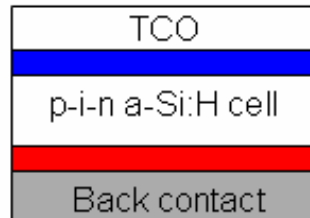


**Figure 1.4.1.1:** Sketch of single-junction a-Si:H p-i-n solar cell structure. The layers may be deposited onto both rigid substrates e.g. glass or onto flexible substrates

### Multi-junction (tandem) amorphous silicon solar cells (MJ a-Si:H)

The light-induced degradation of single-junction a-Si:H cells can be reduced by using thinner layers of amorphous silicon in form of two or more cells stacked on top of one another (Fig. 1.4.1.2). An improvement of the performance can be created by changing the bandgap from high values on top to lower ones by alloying with germanium (a-Si:Ge:H) [Ayr2002]. The module efficiency is in the order of 6 % to 7 %. Usually such cells are deposited on glass substrate. It is possible to stack more than two cells on each other. However, there is no significant increase in efficiency. For instance, triple-junction stacks with different Ge content achieve stabilized efficiency of just 6.3 %. That is insufficient considering the desired reduction in material and processing costs.

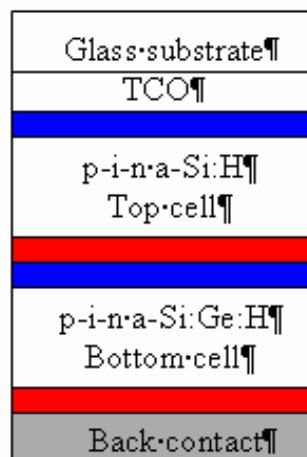


**Figure 1.4.1.2:** Sketch of a-Si:H based tandem solar cells where two or more current matched cells are stacked on top of another.

**a-Si:H/ $\mu$ c-Si:H tandem solar cells on glass**

The next step to improve the efficiency of thin-film solar cells is the combination of an amorphous silicon top cell with and microcrystalline silicon bottom cell. It is much easier and cheaper to use  $\mu$ c-Si:H instead of real c-Si, because of the enormous effort in subsequent crystallization. Thereby variations of the hydrogen concentration in the gas mixture lead to deposition of  $\mu$ c-Si:H films [Bab1995] instead of a-Si:H ones. It should be emphasized again that  $\mu$ c-Si:H films consist of mixed-phases of small crystallites within an amorphous matrix. That is illustrated in figure 1.4.1.3(a). One of the most important advantages of  $\mu$ c-Si:H is the higher stability under intense illumination (LID). The carrier mobility is still low. Therefore, p-i-n structures are still necessary. Due to the more complex cell structure there are matching problems, e.g. match current from a-Si:H top cell with  $\mu$ c-Si:H bottom cell. Such tandem cells can beat triple-junction a-Si:H cells in terms of efficiency and stability [Sha2004] by achieving stable efficiencies of around 10 %. A sketch is shown in figure 1.4.1.3(b).

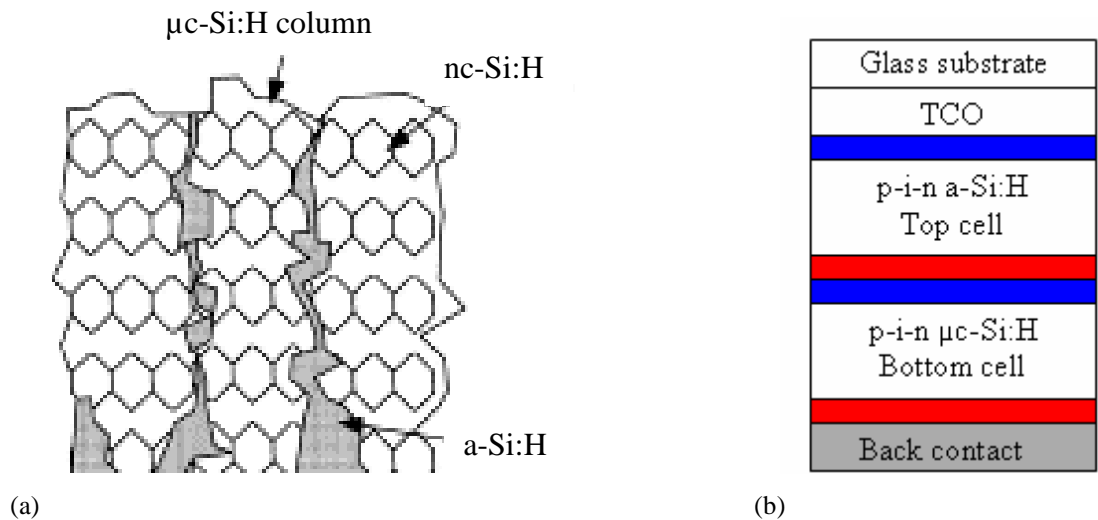


**Figure 1.4.1.3:** Sketch of the structure of  $\mu$ c-Si:H [after Fuh2002] (a); Sketch of a-Si:H/ $\mu$ c-Si:H tandem cell (b)

**Thin-film solar cells based on mono-Si**

One of the main problems of thin monocrystalline Si films is the costs, which are related to the crystallization of mono-Si. Sony Corp. presented the first solar cell result based on a 12 mm thin, mono-Si film with an efficiency of 12.5 % [Tay1998]. This efficiency is comparable to thin-film cells based on large-grained poly-Si. Efficiencies above 19 % are currently only obtained by techniques that are not suited for low-cost production such as wafer thinning employed at the Max-Planck Institute for Solid State Research (MPI) in Stuttgart, Germany [Bren1995] and other groups or the use of epitaxial films on SIMOX substrates by the Fraunhofer Institute for Solar Energy Research (ISE) in Freiburg, Germany.

## 1.4.2 Other thin-film technologies

### Cadmium sulphide

The first thin-film solar cell candidates for large-scale manufacture were based on cadmium sulphide. Attempts to commercialize this technology were not successful, because of the stability issues with the cells and the appearance of amorphous silicon as an apparently superior contender.

### Cadmium telluride solar cell

Investigations in CdTe start in the 1950s [Jen1954]. Its bandgap of about 1.5 eV matches quite well to the distribution of the solar spectrum. A device sketch of cadmium telluride solar cells is shown in figure 1.4.2.1. The substrate and TCO structure is analogous to silicon based thin-film solar cells. The active part consists of a simple heterojunction design involves a p-type CdTe absorber layer matched with n-type  $\text{CdS}_x\text{Te}_{1-x}$ . Various deposition techniques like close-spaced sublimation (CSS), vapor transport, chemical spraying or electroplating are used. Cell efficiency has achieved 16.5 %. CdTe has the optimal band gap for single-junction devices, it may be expected that efficiencies close to 20 % can be achieved. But this positive aspect is reduced by the problem of CdTe-technology, namely the toxicity of cadmium. Therefore, cadmium based PV was banned in some countries.

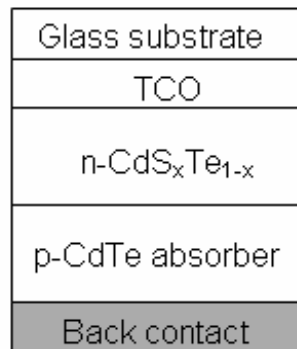


**Figure 1.4.2.1:** Sketch of a CdTe solar cell

### Copper-indium diselenide (CIS)

CIS technology is able to achieve very high efficiency up to 19.5 %. The metal contact is deposited on glass in CIS cells. This is shown in figure 1.4.2.2. The electrical connection is similar to other thin-film cells. Sometimes an additional glass layer on the top is used to laminate the cell stack. One of the main disadvantages of this technology is the limited availability of indium. This might make CIS solar cells unattractive as cheap thin-film technology in the future.

## 1. Basic knowledge

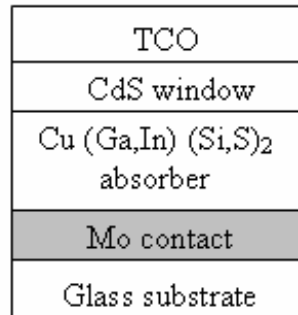


**Figure 1.4.2.2:** Sketch of a CIS solar cell

### Copper indium gallium selenide (CIGSe) solar cells

CIGSe is a I-III-VI<sub>2</sub> compound solid solution of copper indium selenide (CIS) and copper gallium selenide, which is summarized as CuIn<sub>x</sub>Ga<sub>(1-x)</sub>Se<sub>2</sub>. It is a tetrahedrally bonded semiconductor, with the chalcopyrite crystal structure. Its direct bandgap varies continuously with x from about 1.0 eV (for CIS) to about 1.7 eV (for CGS) [Tin1991]. The absorption coefficient is higher than 10<sup>5</sup> cm<sup>-1</sup> [Stan2002]. The basic structure of CIGSe solar cells is shown in figure 1.4.2.3. Usually a glass substrate is used, but other materials (e.g. polyimide or metal foils) have the advantage of flexibility. The substrate is coated with a molybdenum (Mo) layer as back contact and internal reflector. A p-type CIGS absorber layer and a thin n-type ZnO layer form a heterojunction. The CIGS layer is doped by intrinsic defects and the ZnO by aluminum. Usually some buffer layers of CdS and intrinsic ZnO are deposited via chemical bath deposition between these layers. This is necessary to improve the cell performance by electrical isolation between the conductive ZnO and the CIGS layer. CIGSe is mainly used in polycrystalline form reaching cell efficiencies up to 19.9 % and module efficiencies in the order of 13 to 14 %. It should point out that CIGS compared to CdTe need smaller amount of toxic material cadmium.

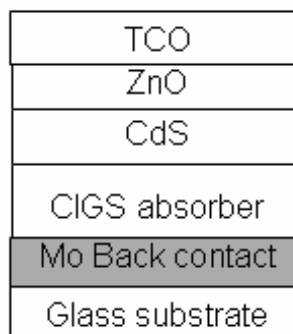


**Figure 1.4.2.3:** Sketch of a CIGS solar cell

### Dye-sensitized solar cell (DSSC, DSC or DYSC)

A dye-sensitized solar cell is a low-cost thin-film solar cell. The basic structure consists of a semiconductor formed between a photosensitized anode and an electrolyte. This creates a photo-electrochemical system. The active element is an organic dye generating electricity

## 1. Basic knowledge

under illumination [Ger1968]. Modern DSSC, Graetzel cells [O'Re1991] are composed of a porous layer of titanium dioxide nanoparticles, covered with a molecular dye that absorbs sunlight, like chlorophyll in green leaves. The main advantage of DSSCs is the low costs. In theory, they can reach the best price/performance ratio of all solar cells, even similar to fossil fuels. The current record efficiency is about 11 % - 12 %. Other advantages are the mechanical robustness and low weight. The major disadvantage to the DSSC design is the use of the liquid electrolyte, which has temperature stability problems. Additional to that DSSC have a quite high affinity to degradation caused by UV absorption.

### **Organic/polymer solar cells:**

The technology is relatively new. It promises high price reduction, because of a simple large-scale production, including processing from solution and simple printing. Device structure differs from inorganic solar cells, based on p-n or p-i-n junction. The absorber (~ 100 nm) consists of two organic semiconductors (including polymers), in what one acts as donor and the other one as acceptor. A light-generated electron-hole pair is generated as exciton and becomes separated by diffusion to donor-acceptor interface. Highest reported efficiencies are in the order of 10 %.

### **Summary and conclusion**

An enormous number of different technologies characterize thin-film solar cells. Note that the reported technologies are just an overview basing on the used absorber materials. There are several technologies for every material (e.g. different electrical connections etc.). Among all these technologies chalcogenide-based solar cells are the one that currently exhibit the highest efficiencies. However, it is highly probable that these solar cells will not dominate the thin-film market, because of their inherent disadvantages. That means the limited availability of toxic and expensive materials, such as indium, molybdenum, etc., and the scientific and technological advantages of silicon. Therefore, Si-based technologies seem to be the dominant thin-film technology in the future. But the exact cell concept is unknown.

## 2. Experimental

Basic elements of PL and Raman will be discussed in this chapter. These are the main investigation techniques in this work. Note that both techniques use the same excitation wavelength of 532 nm. Therefore, the penetration depth of the laser is constant and different results are caused by different sensitivities of the techniques. It should be emphasized that the sub-chapter 2.2 includes the Raman setup and the basic knowledge for interpretation of the detected signal. This is in contrast to PL, where the luminescence features were described in chapter 1. Sub-chapter 2.3 discusses the impact of some typical thin-film effects, which must be considered during the investigation/characterization process. The impact of these effects affects the actual measurements as well as the interpretation.

Important setup parameters of other used techniques, such as EBIC, will be mentioned at the corresponding parts in chapters 3 to 5.

### 2.1 Photoluminescence (PL) investigations

Major parts of the reported results were obtained by using PL techniques. Thereby two different setups were used.

The first one is a camera-based setup for electroluminescence (EL)- and PL investigations. It is an upgraded version of the setup, which was designed for defect monitoring using a luminescence imaging technique for mc-Si solar wafers [Schm2011, Man2012]. Samples can be excited by electrical current for EL or by a LED array for PL. The current is supplied by a power supply connected with the busbars on the front side and the full-scale metal contact on the backside of the solar cell. In case of PL, the sample is illuminated from the backside by a LED array. The standard excitation wavelength is 660 nm. Other wavelength can be applied by using other light sources and optical filters. Unwanted light due to heating of the LED is blocked by a VIS-filter (pass  $\lambda < 800$  nm). An InGaAs 512 x 640 CCD-camera detects the emitted luminescence. The detected wavelength range can be selected by using several filters to image distinct luminescence features, such as BB luminescence or DRL. Usually, the setup is used to get an overview of complete solar wafers. However, it is also possible to obtain higher magnifications, with a maximum spatial resolution of around 30 – 50  $\mu\text{m}$ . This setup is called ‘PL Imaging setup’, from now on.

Another setup was used was used for more detailed PL investigations. It was originally designed by Tzanimir Arguirov [Arg2007a]. The experimental setup is shown in figure 2.1.1. The samples (size: up to 1.2 cm x 1.2 cm) are placed in a liquid nitrogen cryostat Microstat N



## 2. Experimental

(Oxford Instruments), which allows measurements in a range of temperature from 80 K to 325 K by controlled electrical heating. The cryostat is mounted on a motorized XY- table. The excitation beam for PL measurements is supplied by a water-cooled OPS laser (optically pumped semiconductor laser) with 532 nm wavelength of the Verdi G series from Coherent. Before exciting the sample the laser beam passes a prism and an IR-filter (pass  $\lambda < 800$  nm). These optics secure that only 532 nm and no parasitic wavelength can reach the sample. The laser output consists of about 40 % - 50 % near-infrared components, like the fundamental wave (1064 nm) of the frequency-doubled 532 nm.

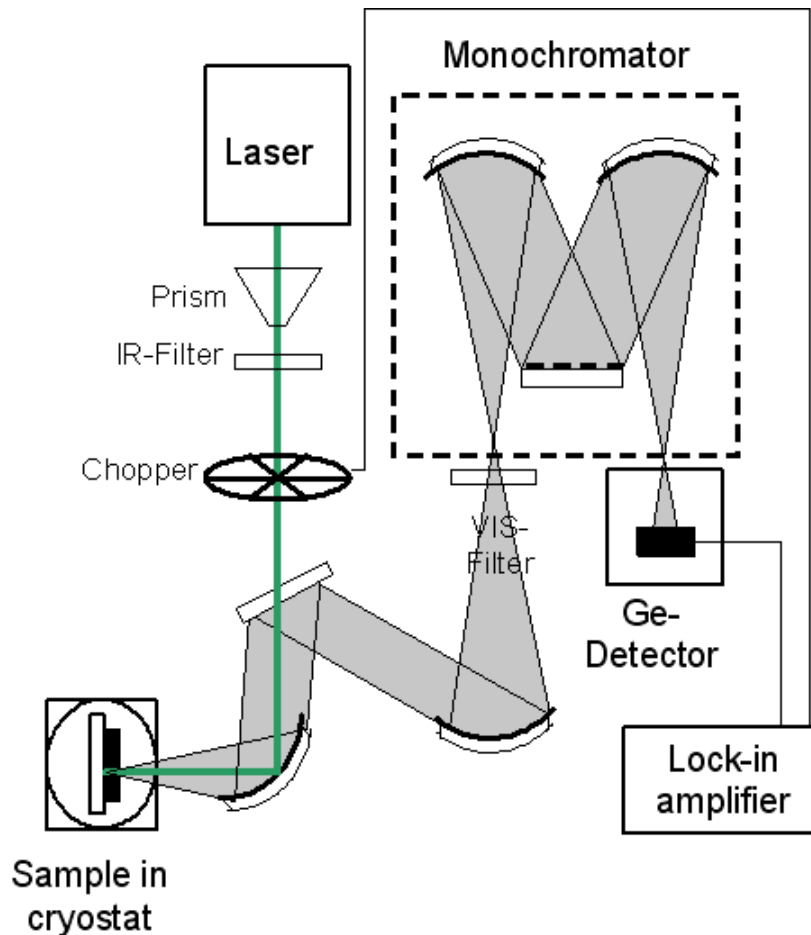


**Figure 2.1.1:** Setup for PL Mapping: The sample is placed in a cryostat and excited by a laser beam. The luminescence is collected by parabolic mirrors and spectrally resolved by a monochromator. For analyzing a Ge-Detector with lock-in amplifier is used.

The power of the laser beam can be controlled by computer software in a range from 10 mW to 2 W (Attention: the power controller does not distinguish between 532 nm and 1064 nm.). The excitation light is directed normal to the sample and focused by a parabolic mirror with a focal length of 12 cm. The focused laser spot has a diameter of about 100  $\mu\text{m}$  at the sample surface. The same mirror, which is used to focus the laser beam, collects the emitted luminescence and guides it to other mirrors. The last mirror focus the luminescence light on the monochromator slit. In front of the monochromator a VIS-filter (pass  $\lambda > 800$  nm) is placed to eliminate scattered light of the excitation wavelength. The luminescence is

## 2. Experimental

spectrally resolved by a monochromator (HR 640 Jobin Yvon) offering the possibility to choose three different gratings blazed at 1300 nm each. Depending on the desired spectral resolution, it can be selected between 300, 600 or 1200 l/mm grating. The 300 l/mm grating is set as standard giving a spectral resolution of about 2 nm. The bandpass of the monochromator can be adjusted by the widths of the entrance and exit slits. It is set to 15 nm as standard. Luminescence is detected by a liquid nitrogen cooled germanium p-i-n diode (North coast L). The detector is sensitive between 800 nm and 1800 nm (1.55 eV – 0.69 eV). A mechanical chopper modulates the signal with a frequency of 33 Hz to use lock-in technique to amplify the signal.

For scanning PL measurements, the monochromator can be set on a fixed wavelength and than the sample can be scanned by stepwise moving of the motorized XY-table. Therefore, this technique is also called ‘PL Mapping’. A typical step size is about 50  $\mu\text{m}$ . Note that this is not equal to the spatial resolution, because of the laser spot size and changing spatial distribution of the excess carriers by diffusion processes. A rough estimation of the real spatial resolution is about 100  $\mu\text{m}$ , depending on the diffusion length of the investigated material.

Temperature dependent EL measurements were performed on another setup allowing temperature ranges from 10 K to 300 K. Thereby the samples (size: 1 cm x 1 cm) are mounted on a sample holder and contacted with contact fingers supplying current from a stabilized power supply. The sample holder is placed in a Closed-cycle Refrigerator System, which provides the cooling of the sample by controlled compression and expansion of a fixed volume of helium gas. A compressor is used to provide the high-pressure helium gas needed for the cycle. Flexible metal gas lines deliver the compressed helium gas to the refrigerator for cooling the sample, and return the low-pressure gas to the compressor for recirculation. This setup allows comparisons with the excitation conditions of PL, whereas the excitation beam comes from a pulsed ns-laser system. This system consists of a pump laser (Continuum Powerlight 9030) and an optical parametric oscillator (Continuum Panther EX OPO). The laser parameters are a pulse length of about 5 ns with a repetition rate of 30 Hz and wavelengths between 410 nm and 2550 nm (differing energies). The spot size is limited by an iris diaphragm to about 1 mm. The luminescence is collected by two parabolic mirrors and focused into a monochromator with a 300 l/mm grating blazed on 1700 nm. The monochromator is equipped with an air/water cooled InGaAs CCD-line detector operating at  $-60\text{ }^{\circ}\text{C}$  /  $-70\text{ }^{\circ}\text{C}$  (Andor iDUS DU492A-2.2).

### 2.2 Raman Spectroscopy

Raman spectroscopy offers an approach to several features of solid states. For instance, it can be used to identify different materials. Its abilities to identify several phases of solid states (chapter 5) and to investigate internal stress (chapter 4) are important for this work. In general, Raman scattering describes the inelastic scattering of a photon under emission (Stokes process) and under absorption (Anti-Stokes process) of a phonon. A detailed discussion of the method is given in the literature (e.g. [Lon1977]). The identification of

## 2. Experimental

different phases based on the differences in translation symmetry with well-defined electronic transitions and selection rules.

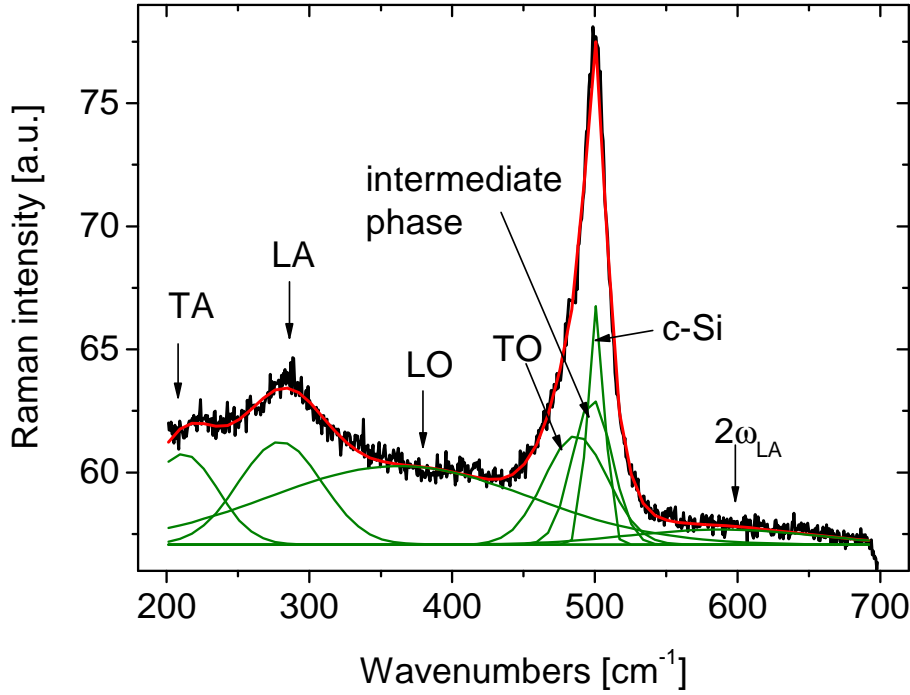


**Figure 2.2.1:** Deconvolution of  $\mu\text{c-Si:H}$  Raman spectrum: Several phonon modes are attributed to a-Si:H. For  $\mu\text{c-Si:H}$  the intermediate ( $\sim 505 \text{ cm}^{-1}$ ) and crystalline components ( $\sim 520 \text{ cm}^{-1}$ ) are characteristic.

Figure 2.2.1 shows a typical Raman spectrum of a microcrystalline silicon thin-film excited by a 532 nm laser and the deconvolution into several Gaussian peaks. It consists of a complex mixture of peaks, which attribute either to amorphous or to crystalline silicon. The broad peaks around  $200 \text{ cm}^{-1}$  (TA),  $300 \text{ cm}^{-1}$  (LA),  $400 \text{ cm}^{-1}$  (LO) and  $480 \text{ cm}^{-1}$  (TO) belong to several phonon modes of a-Si:H. The weak peak labeled  $\omega_{2\text{LA}}$  at about  $600 \text{ cm}^{-1}$  is an overtone of the main a-Si  $\omega_{\text{LA}}$  structure [Ric1981, Lia2008]. A very sharp peak at  $520 \text{ cm}^{-1}$ , characterizes c-Si. An additional peak at around  $505 \text{ cm}^{-1}$  is typical for  $\mu\text{c-Si:H}$ . It was associated with structural defects of the crystalline phase (stacking faults) as well as bond dilutions at grain boundaries [Vep1987]. However, this intermediate phase is a typical Raman feature in  $\mu\text{c-Si:H}$  samples and is related to the transition from amorphous to crystalline silicon in any way. Various  $\mu\text{c-Si:H}$  films mainly differ in their crystalline volume fraction. That describes the ration of remaining a-Si:H to crystalline regions. It can be determined by following equation:

$$X_c = \frac{\sum I_c}{\sum I_c + y I_a} \approx \frac{I_{505} + I_{520}}{I_{480} + I_{505} + I_{520}} \quad (2.2.1)$$

, where  $I_c$  and  $I_a$  are the integrated intensities of the crystalline component and the amorphous component, respectively.  $X_c$  is the crystalline volume fraction including the ratio of the cross section for the amorphous and crystalline phase  $y$ . A determination of this parameter requires the knowledge of the actual grain size [Bus1988] (by XRD or TEM). For that reason, a simplification of the equation is given by focusing on the main amorphous peak at  $480 \text{ cm}^{-1}$ ,

## 2. Experimental

the c-Si peak at  $520\text{ cm}^{-1}$  and the intermediate one at  $505\text{ cm}^{-1}$ . The obtained value of this simplified equation is known as Raman-crystallinity and is a well-established measure for  $\mu\text{c-Si:H}$  films. All crystallinities in this work are Raman-crystallinities.

The peak position and peak width of the c-Si peak is a measure for the crystallinity/crystalline quality of silicon. Usually the c-Si Raman peak of Si thin films appears at lower Raman frequencies and is broader as that one measured on mc-Si or even mono-Si wafers.

Mechanical strain or stress affects the peak position of the Raman modes. Ganesan et al. [Gan1970] wrote one of the first theoretical papers about this. Compressive uniaxial or biaxial stress leads to an increase of the Raman frequency, while tensile stress causes a decrease. A detailed description about the theoretical background is given in [Wol1996]. Note that the temperature also affects the peak position. Therefore, a careful selection of the used laser power is necessary.

### Raman setup:

The Raman setup is shown in figure 2.2.2. In this work, the microscopic entrance of the spectrometer was used. The spatial resolution is limited by the laser spot size to around  $1\text{ }\mu\text{m}$ . A microscope focuses the laser beam for excitation of the sample. The microscope is also used to collect the scattered light from the sample. Investigations of the spatial distribution of the Raman signal were not performed, because of the required high flatness of the sample surfaces. The investigated thin-film samples are characterized by very rough surfaces. The used Raman spectrometer is a Dilor XY-Modular Raman spectrometer consisting of a double-grating monochromator (G) and a  $\text{LN}_2$  cooled Si CCD-Detector. The used laser is an diode-pumped frequency-doubled Nd:YVO<sub>4</sub> laser with a wavelength of 532 nm. The applied laser power at the sample is between 2 and 5 mW. A Labspec-Software is used for spectrometer control and the recording of the spectra.

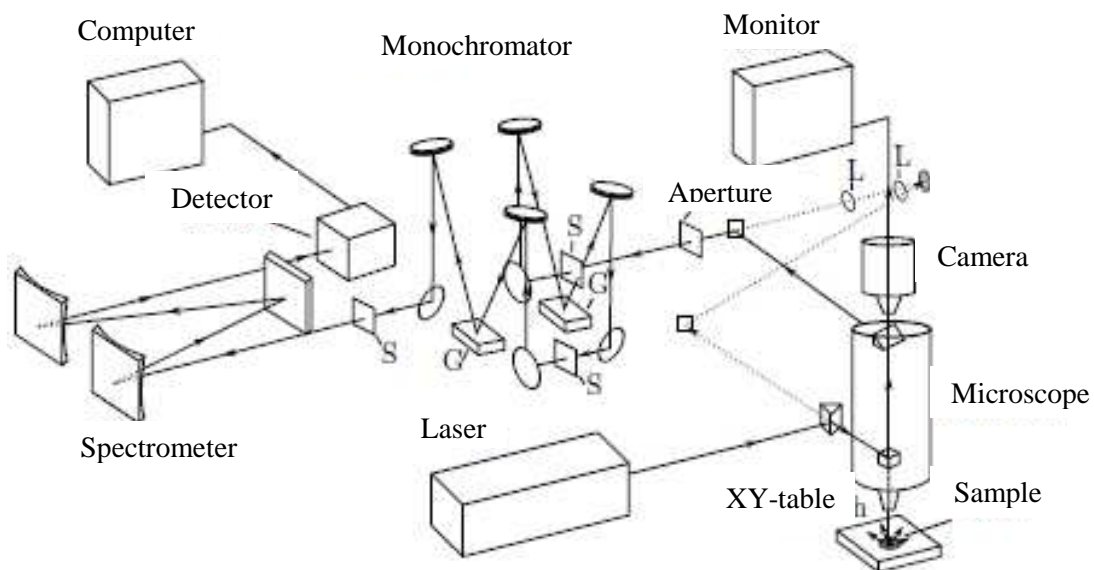


Figure 2.2.2: Raman setup

### 2.3 Typical effects in the analysis of thin-film samples with laser-based techniques

This sub-chapter gives a short summary of some effects, which are typical for laser-based investigation techniques on thin-film samples. With this, it will be easier to follow the detailed investigation processes of several thin-film samples in the following chapters. Most thin-film samples are characterized by specific effects, which must be identified during the investigation/characterization process. Therefore, this chapter describes some typical thin-film effects very roughly. Their exact impact depends on the specific samples. It is very important to consider them before the actual investigation/characterization process starts. It is also possible that some effects can interact with each other. The description is focused on PL analysis of silicon layers on glass substrate. But, it can also be used on other thin-film materials (e.g. CIS) and other techniques, especially laser-based ones (e.g. Raman spectroscopy).

#### **Lower laser power:**

The maximum laser power of the used PL setup is about 1 W at 532 nm with a spot size of about 100  $\mu\text{m}$ . This excitation density does not influence the sample structure in case of bulk mc-Si wafers. But on thin-film samples, it would result in extreme, probably destructive modification of the sample. Thereby two types of modifications can be distinguished.

The first one is a more general modification of the sample induced by radiation. It also appears under excitation by sunlight. The typical timescales are quite long (hours to months). Such light-induced degradation processes are not specific to thin-film materials. They are also present in bulk silicon. An example is the creation of boron-oxygen complexes in mc-Si [Kno1996]. However, in thin-film materials these effects are much more critical. An example is the Staebler-Wronski effect (SWE) [Wro1976, Sta1977]. Such effects result in reduced solar cell efficiency. It can be understood as a background effect, which is often dominated by other modifications of the second type.

Modifications of the sample induced by this type appear much faster and are directly related to the high intensity of laser light. The effects range from phase transformations, e.g. light-induced crystallization of a-Si:H [Der1981, Im1993] to melting and burning. The probability for these effects is amplified due to less heat dissipation because of the low material volume and thermal insulation by the glass substrate. Some of the effects do not exhibit visible modifications at the sample surface, even with an optical microscope. It is necessary to combine the use of low laser powers and simultaneous control of the sample during measurements to avoid these light-induced modifications. A web cam and spot tests of repeated measurements at known positions performed sample control. Nevertheless, the key-point is still the selection of the laser power. There is no simple procedure to determine the correct power. The penetration depth and the heat concentration in the material due to thermal insulation give important evidences by glass substrate. Therefore, it can easily be concluded that CIS/CIGSe samples require much lower laser power than Si, because of the different absorption coefficients ( $\sim 10^5 \text{ cm}^{-1}$  for CIGSe [Wan2010] and  $\sim 10^4 \text{ cm}^{-1}$  for Si). Nevertheless, this is only a very rough evidence for the selection of the exact laser power and must be added by experimental investigations on the specific sample. Suitable values for Si

## 2. Experimental

on glass are in the range of 50 to 100 mW. The actual investigation/characterization process should be realized at lower values, if possible. It is obvious that low laser powers enhance to the low PL signal because of low material volume and the surface recombination additionally. This must be compensated by longer integration times and/or averages series. The problem becomes further amplified in case of investigations requiring very high spatial resolution due to the related higher focusing of the laser beam.

### **Optical interferences:**

Usually thin-film samples consist of many different layers. Therefore, luminescence spectra can be influenced by multiple reflections in the sample structure creating optical interferences. It should be emphasized that the incident laser beam, in case of PL, does not create the optical interferences. The actual source of the interferences is the generated luminescence itself. Therefore, it is also present in other luminescence techniques, e.g. electroluminescence. Of course, optical interferences require plane cell structures on the scale of the laser spot size. Nevertheless, microscopic roughness of the layers, which are desired to improve light trapping, do not affect the creation of interferences pattern.

Fortunately, interferences can be identified easily. Changed incident angles of the laser beam lead to significant peak shifts in case of optical interferences. Therefore, it is possible to reduce the impact of optical interferences and to obtain spectra with suppressed interferences pattern. However, for real interference-free spectra another PL setup must be used.

The 'Standard PL setup' configuration is shown in figure 2.3.1(a). It is well established for bulk materials. In this case, the laser is directed normal to the sample surface and the luminescence is collected above the sample. The advantages of this setup are a very high PL intensity and the possibility for investigations of the spatial distribution by scanning. The main disadvantage is the presence of interferences. This artifact is eliminated in another PL configuration, which is shown in figure 2.3.1(b). It is called 'Cross-section PL setup'. In this geometry, the laser is still directed normal to the sample surface, but the luminescence is collected along the cross-section of the sample. Thereby two properties of this setup must be noted. The first one is that luminescence has to pass much more material before reaching the cross-section surface. Therefore, reabsorption plays a significant role. That is minimized as good as possible by using low distances between cross-section surface and position of laser spot of about 1 mm. The limited distance excludes the possibility of scanning PL. The other property is the difference in collection efficiencies of luminescence from layers of different thicknesses. This is caused by the different propagation of light, which is strongly suppressed in very thin layers, where the wavelength of luminescence is higher than the effective layer thickness. A simple estimation illustrates the problem. Let us assume that the detected luminescence ranges from around 800 nm to 1700 nm and the thickness of the emitting layer is in a range of a few hundred nanometers. So it is very improbable for light to pass a distance of around 1 mm, when the wavelength of luminescence is significantly higher than the layer thickness (the absorption coefficient of Si is around 4). Therefore the collection efficiency of luminescence is the less the thinner the emitting layer becomes.

Temperature dependent measurements were only possible in 'Standard PL setup', because of the geometry of the cryostat. Optical interferences must be considered and reduced during the measurements.

## 2. Experimental

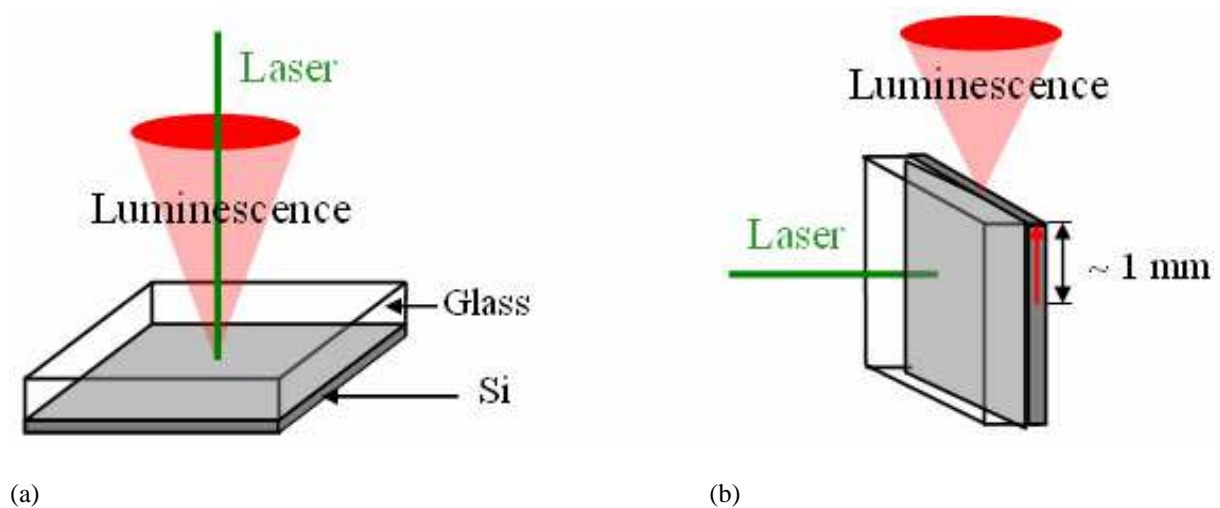


**Figure 2.3.1:** PL setups: Standard PL setup (a); Cross-section PL setup (b)

### Parasitic luminescence signals:

The analysis of the thin-film samples is focused on the absorber materials, usually silicon. However, there are also other components in the solar cell structure emitting luminescence signals. The spectral overlap of these signals makes it more complicated to investigate the interesting luminescence from the absorber. These parasitic luminescence signals can be created in other materials as well as in the entire sample structure, e.g. optical interferences. It was already described how to avoid/reduce optical interferences. Elimination of luminescence from other materials in the sample structure urgently requires detailed investigations of partially processed samples. That allows the attribution of luminescence signals to distinct layers as well as the investigation of the influence of several processing steps on these layers. In case of silicon on glass, the first partially processed sample must be the glass substrate alone. Often luminescence spectra from glass exhibit a complex spectrum with a main peak at around 1.16 eV.

The desired spectra of the absorber layer can be obtained by two different approaches. The first one is to place the sample with the glass substrate on the bottom side and the excitation is directed on the absorber. This approach is restricted to quite thick films, where the penetration depth of the laser is lower than the thickness of the absorber layer. Note that the Lambert-Beer law defines the physical term of penetration depth. That means that penetration depth represents the distance after that incident light intensity is reduced by the factor  $1/e$  ( $\sim 37\%$ ), whereas  $e$  is Euler's number. An efficient suppression of luminescence from glass substrate requires an absorber thickness of at least 3 times the penetration depth. Then the laser power is reduced to less than 5%. In case of the used laser wavelength of 532 nm a Si layer should have a thickness of more than 3  $\mu\text{m}$ . However, such geometry might lead to insufficient cooling of the layer, because of thermal insulation due to the glass substrate (see: Thermal insulation due to glass substrate).

On thinner absorber layers and/or thicker glass substrates, another approach must be used to eliminate luminescence from glass. Thereby the sample is placed with the glass substrate on the top and its luminescence must be eliminated by deconvolution of the measured

## 2. Experimental

spectrum. This geometry is needed because of the spectral broadness of luminescence from glass. The mentioned peak at 1.16 eV is just the dominant peak among others, reaching from about 800 nm to 1700 nm. If the Si layer would be on the top, it would act as a filter for the luminescence from glass. Note that Si is characterized by enormous deviations in absorption/transmission over several orders of magnitude in the investigated spectral range. Therefore, deconvolution of luminescence would require temperature-dependent absorption/transmission curves for every specific Si film. Such data are not available.

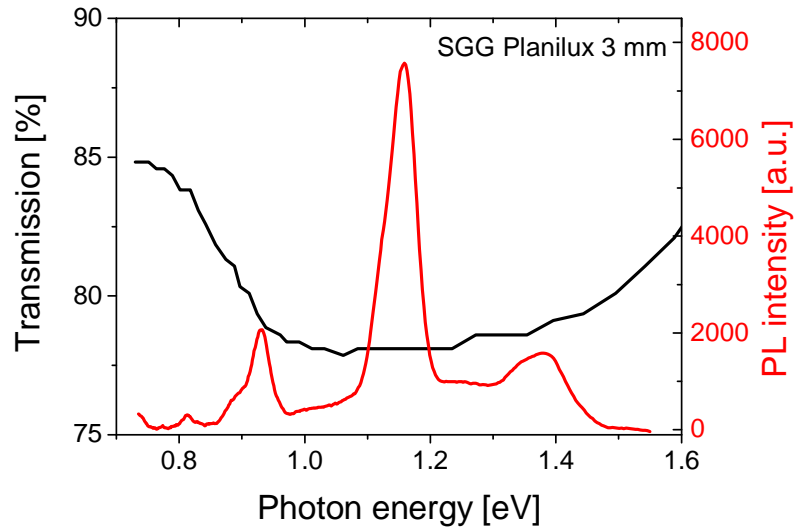


**Figure 2.3.2:** Transmission and PL spectrum of SGG Planilux glass with a thickness of 3 mm. This type of glass was used on the samples in chapter 5. The transmission data are extracted from datasheet of SGG [SGG2007].

Of course, the absorption/transmission of glass is not constant over the entire spectral range and so luminescence from Si is influenced by spectral-dependent filtering, too. However, such measurements are significantly less affected by filtering because of the lower deviations of transmission/absorption of glass compared to Si. That is illustrated in figure 2.3.2 on the example of SGG Planilux glass with a thickness of 3 mm. This type of glass is used for the a-Si:H/ $\mu$ c-Si:H samples in chapter 5. There one can see deviations in the transmission of around 5 %. Nevertheless, in some cases this small deviation must be considered. For instance, it can lead to slight shifts of peak positions, especially when the luminescence from glass is more intense than that one from Si. This was observed in chapter 5.2 and reduced by comparative PL measurements excited from both sides of the sample.

Another problem in the deconvolution can appear if the exact ratio between the luminescence intensities from glass and Si exhibit strong dependences upon external parameters. In general, the ratio of luminescence signals from different layers is not affected by different spot sizes of the laser beam within the sample stack, because of the used non-confocal PL setup with a focal length of around 12 cm. Nevertheless, on very thin absorber layers the luminescence ratio can be affected by another effect. In this case, the ratio between PL signals from glass and absorber must be considered more carefully. The problem is illustrated in figure 2.3.3. The incident laser beam is reflected on the sample holder and passes absorber and glass substrate again. Then the beam can be reflected on the glass/air interface. So the way of the laser beam can be amplified multiple times. It is determined by the temperature-dependent absorption coefficient  $\alpha(T)$  of the Si absorber mainly. Therefore the



## 2. Experimental

exact intensity ratio must be determined for every sample of a series (e.g. different crystallinity of  $\mu\text{c-Si:H}$ ) and every temperature.

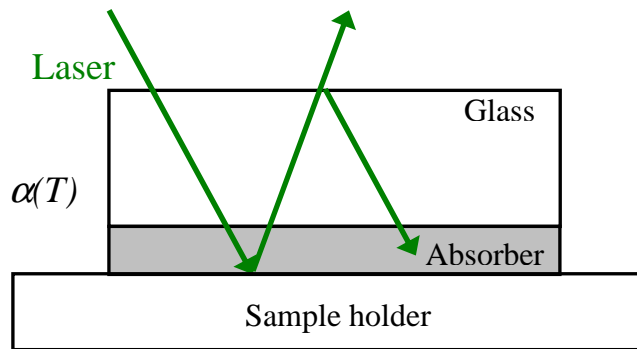


**Figure 2.3.3:** Multiple reflections in thin-film sample leading to changed ratio of luminescence intensities between entire sample and glass substrate. The ratio mainly depends on the absorption coefficient  $\alpha(T)$  of absorber layer.

On such thin samples, when the laser is reflected on the sample holder, it must be secured that the sample holder does not influence the luminescence spectra in any way. For instance, the sample holder could scatter the laser beam. This would affect investigations of the spatial distribution of luminescence and was avoided by a polished aluminum on the sample holder.

### **Thermal insulation due to glass substrate:**

The high thermal insulation of the glass substrate can limit the laser-induced dissipation of heat as well as the efficient cooling of the absorber layer during temperature-dependent measurements in the cryostat. The first point was already discussed (see: 'Low laser power'). The second point becomes important if the glass is localized on the bottom (see: 'Parasitic luminescence signals'). In this case, the poor thermal conductivity/high thermal insulation of the glass substrate leads to not well-defined temperatures of the absorber and sometimes the desired temperature cannot be achieved. The problem can be avoided by placing the glass substrate on the top of the sample. This approach requires plane and unstructured glass substrates. Otherwise, the laser beam would be scattered and that would eliminate the possibility for scanning PL measurements. Note that the problem is always present in EBIC measurements, because of the needed sample geometry with the glass substrate at the bottom of the sample holder [Sei2011].

### **Low material volume/Enhanced non-radiative recombination at interfaces:**

The low material volume is one of the most characteristic properties of thin-film samples. Among others, it becomes noticeable, because of the low signal intensity. This cannot be compensated by the use of higher laser powers (see: 'Low laser power'). The problem is additionally amplified by the enhanced non-radiative recombination at interfaces. It is the

## 2. Experimental

general form of surface recombination, which was already described in sub-chapter 1.1. The word ‘enhanced’ is used intentionally instead of ‘amplified’. It emphasizes the fact that interface recombination does not just reduce the luminescence intensity. It can also affect other features of luminescence on thin films. For instance, interface recombination can lead to specific spatial distributions in case of regular interface structures [Sei2011]. Another point that can be affected is the determination of the deactivation energy by fitting the temperature dependent luminescence intensity [Sue1983a, Sau1985].

### Light trapping and scattering by rough/textured interfaces:

Light scattering and light trapping on rough interfaces by texturing is commonly used to improve the efficiency of solar cells. Its importance in thin-film PV is caused due to the low sample/layer thickness and high probability of total internal reflections within the cell stack. This has a significant impact on the characterization/investigation by laser-based techniques (e.g. PL). For instance, it is hard to compare samples with different interface roughness, considering the different absorptions leading to different signal intensities. One way to reduce this impact is to compare the absorption probability of rough textured interfaces with those on flat ones. Deckman et al. [Dec1983] suggested a procedure for this. Thereby the absorption expected of rough samples can be estimated considering multiple reflections of a light beam inside the layer. The enhanced absorption probability  $F_{en}$  is an infinite geometric progression.

$$F_{en} = \frac{(1 - \exp[-2\alpha l]T)}{1 - \exp[-2\alpha l] + [n_2^2 / n_1^2]T \exp[-2\alpha l]} \quad (2.3.1)$$

Here  $l$  is the mean thickness of the sample,  $\alpha$  is the optical absorption coefficient,  $n_1$  and  $n_2$  are the refractive indices of the textured medium and the surrounding dielectric, respectively, and  $T$  is the Fresnel transmission coefficient of the semiconductor-dielectric interface. The impact of light scattering in different films can be compared by an enhancement factor, which is given by  $E(a) = F_{exp}/F_{flat}$ , where  $F_{exp}$  is the experimentally measured absorption probability in the textured film and

$$F_{flat} = \frac{T(1 - \exp[-\alpha l])}{1 - (1 - T)\exp[-\alpha l]} \quad (2.3.2)$$

is the absorption probability in an equivalent flat sample. It is possible to calculate the enhanced absorption in case of quite simple textures (e.g. regular pyramids). But on typical thin-film samples with total reflection in several layers and random interfaces roughness such calculations do not lead to sufficient results. Another important point of rough interfaces is a higher probability for interface recombination.

This is just a very short overview of effects, which may affect the analysis of luminescence on thin-film samples. It emphasizes the enormous impact of low sample/layer thicknesses and the related importance of interfaces. This sub-chapter will be mentioned as reference during the detailed investigations of the thin-film samples (chapter 3 to 5).

## **Part I**

### **3. Electron-beam crystallized large grained Si thin films**

The investigated samples are partially processed electron-beam crystallized large grained silicon solar cells on glass substrate. They were produced at Helmholtz-Zentrum für Materialien und Energie Berlin (HZB) by Daniel Amkreutz et al. Partially processed refers on this absence of any electrical contacts. The sample structure is selected for focusing on the material properties of the subsequently crystallized silicon. The absorber layer is thicker than typical thin films and the silicon grain sizes are quite high, almost similar to bulk mc-Si. Because of these very specific properties, the samples present a first step in the evolution from bulk mc-Si to Si thin-film phases, such as a-Si:H and  $\mu\text{c-Si:H}$ . Therefore, these samples are a good beginning to discuss the key-questions of this work. The reported results were presented at the 48. Punktdefekttreffen [Klo2011].

#### **Investigated samples:**

The samples consist of a 250 nm thick amorphous SiC:B layer, deposited by RF magnetron sputtering onto a commercial available glass substrate (Corning EagleXG) of around 1 mm thickness. This layer acts as diffusion barrier and supports the wetting of Si. The Si absorber is deposited as amorphous to nanocrystalline Si by a LPCVD process (Low Pressure Chemical Vapor Deposition). The nominal thickness is about 10  $\mu\text{m}$ . After deposition, the absorber becomes subsequently crystallized by using a line shaped electron-beam with a constant scanning speed. So the silicon starts to crystallize to large grains with a typical grain size of a few hundred micrometres in the broadness and a few millimeters in the length. Sketches of the investigated samples and the finally processed cells are shown in figure 3.1(a) and figure 3.1(b), respectively. It should be emphasized that the glass substrate is localized on the backside in this solar cell concept. It will be not transmitted by incident sunlight. Further information about the samples can be found in [Amk2011, Sei2011].

### 3. Electron beam crystallized large grained Si thin films

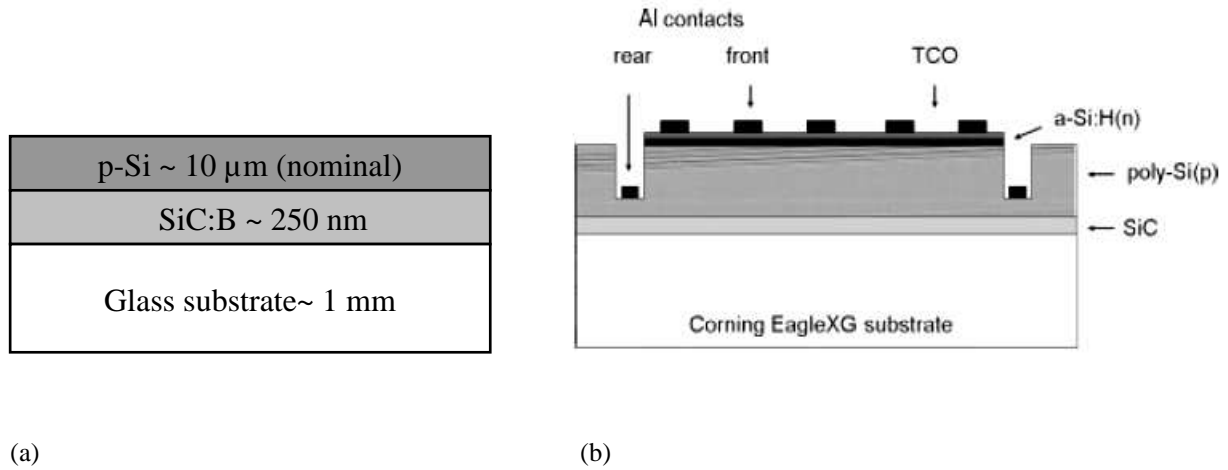


**Figure 3.1:** Sketch of the investigated partially processed sample structure (a) and the finally processed solar cell (Image taken from [Amk2011]) (b)

## 3.1 Results and Discussion – Optical investigations

### Transmission investigations:

Ten micrometres silicon is a quite high thickness for thin-film solar cells. It may allow PL investigations by the PL Imaging setup, which was originally designed for mc-Si wafers [Schm2011, Man2012]. Excitations by various wavelengths were performed to obtain the optimal PL intensity considering the high dependence on the absorption of the incident wavelength.

Despite of this the emitted PL intensity is too low for the sensitivity of the used InGaAs camera. Nevertheless, the transmitted light can be used to obtain an image of the actual layer thickness. Figure 3.1.1(a) shows a transmission image, excited by 660 nm LEDs. The samples exhibit broad bands of more or less thick silicon. Finer linear structures are visible within these bands. It is remarkable that all structures exhibit the same direction. A profile along the red arrow was extracted, which is perpendicular to the band structures to obtain the actual layer thickness. These data were used to estimate the silicon layer thickness, assuming a homogeneous glass thickness and a negligible impact of the very thin SiC:B buffer layer. The calculations obtain an average absorber thickness of around 8.5 μm (Fig. 3.1.1(b)). This is a significant deviation from the expected nominal thickness of 10 μm. Moreover the observed bands correspond to variations in the silicon layer thickness of around  $\pm 1$  μm. The regularity of these bands and finer structures indicates a correlation with the processing of the samples. Discussions with D. Amkreutz suggest that the bands are created during the electron-beam crystallization and not during the deposition. It might be related to some diffusion or segregation processes of the heated Si.

### 3. Electron beam crystallized large grained Si thin films

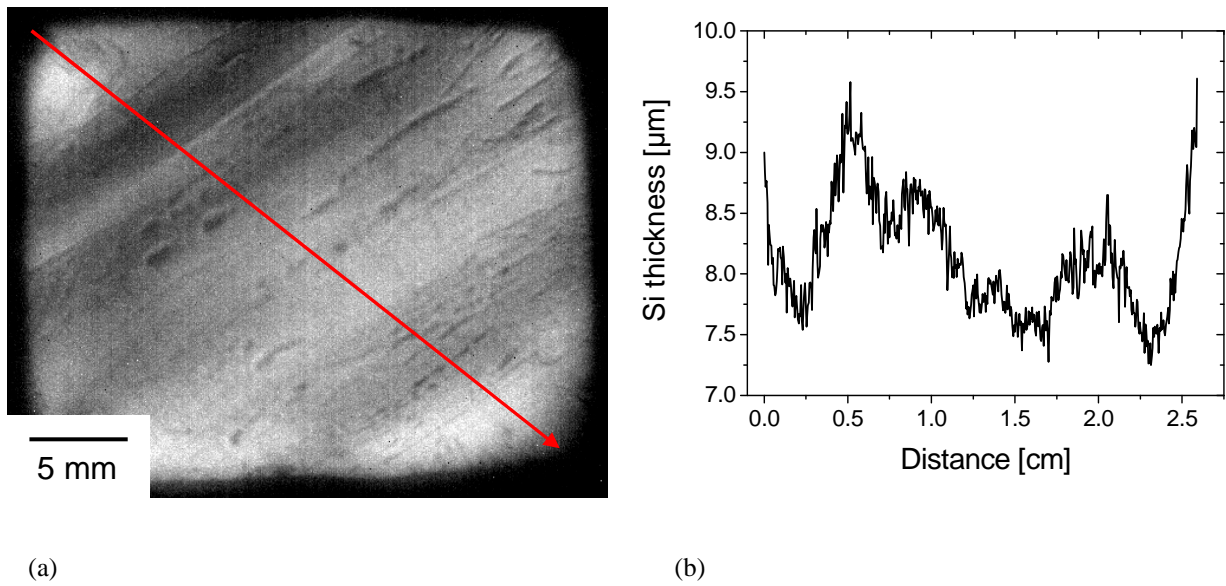


**Figure 3.1.1:** Transmission measurements by PL Imaging setup: Transmission image of the electron-beam crystallized sample with an excitation wavelength of 660 nm (a); calculated profile of the thickness of the silicon absorber layer along the red arrow (b)

At longer wavelength, like 1480 nm, the samples become almost completely transparent. Nevertheless, the incident light is still affected by structures within the samples due to light scattering etc. This allows investigations of the topography of distinct layers by tiny variations of the camera focus. Of course, it is not possible to correlate the images with exact depths in the sample stack. Layers can only be distinguished if there are specific topographical differences between each other. Besides this, the layers must have a detectable thickness. Therefore the very thin Si:C layer cannot be investigated in this way. These requirements do also exclude the application of the PL Imaging setup on most other thin-film samples. But on this specific electron-beam crystallized sample the requirements is fulfilled.

Transmission images at 1480 nm exhibit interesting features, which are illustrated in figure 3.1.2. Both images exhibit a circular distribution of light, which is caused by the inhomogeneous illumination source. The camera is focused on the sample surface in figure 3.1.2(a). It mainly shows the silicon absorber layer. The focus in figure 3.1.2(b) shows the topography of the glass substrate. The silicon layer is characterized by structural inhomogeneities, exhibiting one main direction, marked by a dashed line. The direction is equal to that one in figure 3.1.1(a). Important is that these structures vanish in the image of the glass substrate. Therefore, the structures must represent defects in the silicon layer and could denote the direction of subsequent crystallization by the electron-beam. Perpendicular to this, regular lines become dominant by focusing on the glass substrate, marked by the dashed line in figure 3.1.2(b). The strong correlation between crystallization and Si structures on the one hand and structures in the glass substrate on the other hand might indicate a formation during the electron-beam crystallization. Discussions with D. Amkreutz obtain that the regular structures in Si and glass are probably created during the subsequent crystallization process. Thereby the electron-beam moves step-by-step over the sample. Every step is represented by one line in figure 3.1.2(b). The excitation by electron-beam leads to crystallization of Si as well as thermal instabilities and modification in the glass substrate

### 3. Electron beam crystallized large grained Si thin films

(possibly melting). The perpendicular directions of silicon crystallization and structures in the glass substrate are one of the most characteristic features of these thin-film samples.

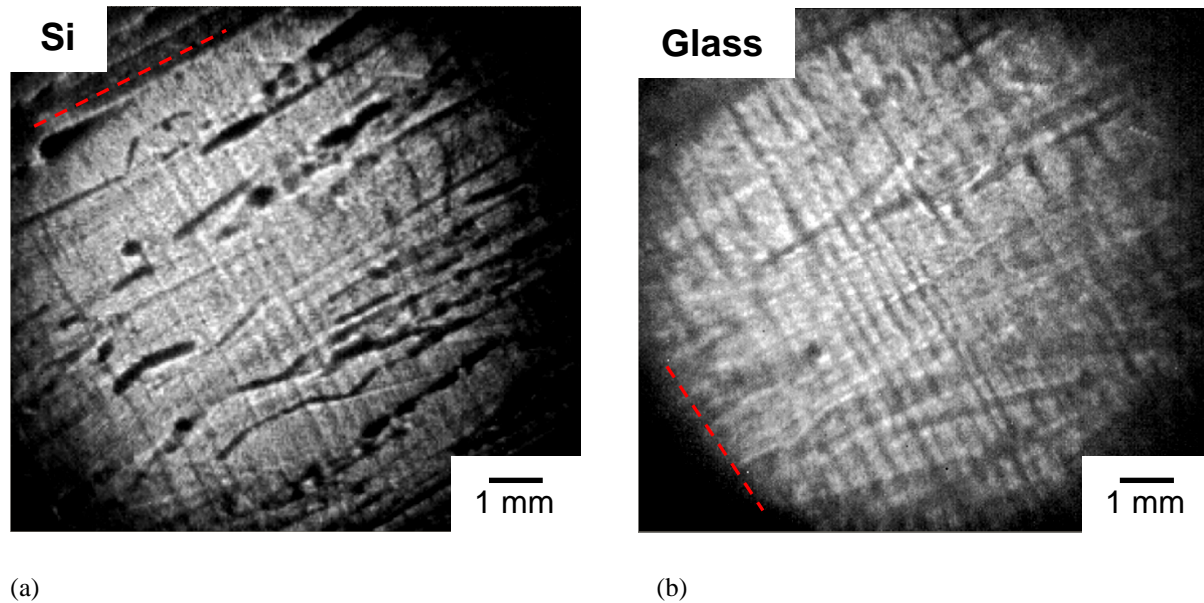


**Figure 3.1.2:** Transmission measurements by PL Imaging setup: Transmission image of the sample with an excitation wavelength of 1480 nm focused on different layers/depths of the sample stack: mainly Si absorber (a); mainly glass substrate (b). Circular intensity distribution is caused by inhomogeneous illumination source.

It is quite surprising that investigations by the PL Imaging setup were able to reveal these important features just by very simple adjustments of the setup. Despite of the fact that the setup cannot be used for most other thin-film samples, because of lower layer thicknesses, the obtained results are very informative and helpful for further steps of characterization and investigation process.

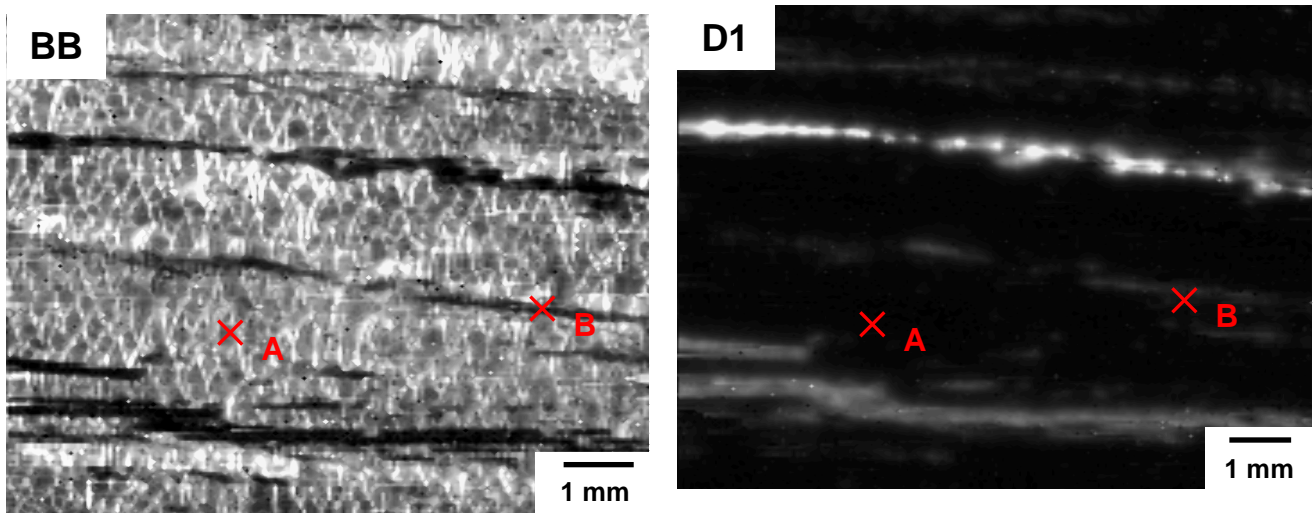
#### PL investigations:

For detailed PL investigations, at the PL Mapping setup, the samples were placed with the glass substrate on the bottom. That avoids possible scattering of the laser in the structured glass substrate. Fortunately, the silicon layer is thick enough to exclude PL signals from the glass. Cooling problems due to thermal insulation of the glass can be neglected, because of the quite thin glass substrate (~ 1 mm). This guarantees sufficient cooling of the Si layer on the PL setup.

The detected PL intensity is quite high considering the low material volume and the missing passivation. The samples exhibit only BB luminescence and no defect-related luminescence (DRL) at room temperature. PL Mapping shows extended defect regions of reduced BB luminescence (Fig.: 3.1.3(a)). The spatial distribution of luminescence is almost independent on the temperature. Therefore, the distribution of the BB Map at 300 K is equal to that one at 80 K, which is shown in figure 3.1.3(a). The defect regions exhibit a main linear direction over the entire sample size. This corresponds to the direction of the defects, which was already observed by transmission measurements. It should be emphasized that these

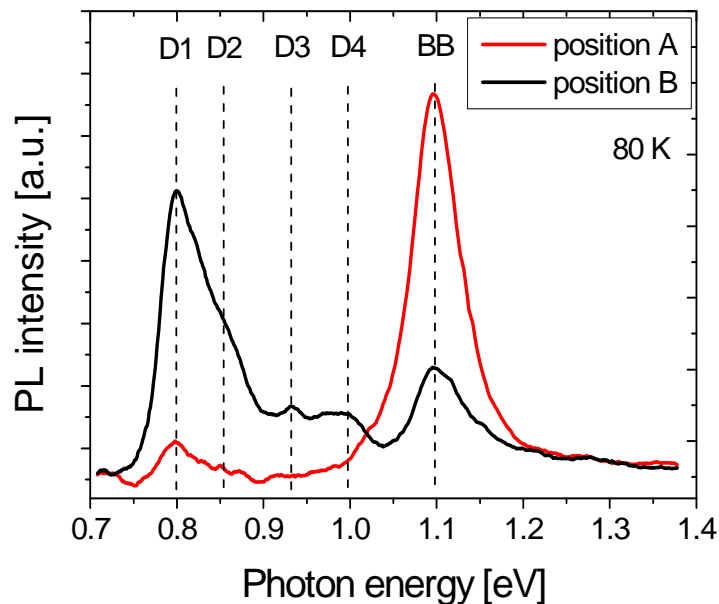
### 3. Electron beam crystallized large grained Si thin films

defect regions are quite extended. That forces the conclusion that the defect regions represent highly dislocated silicon grains and no grain boundaries, according the typical grain size of a few 100 micrometers. Two effects can explain the absence of grain boundaries. The first one is a possibly more ordered crystal growth in comparison to ingot casting of mc-Si due to the high effort in the crystallization process. The second effect considers the fact that optical effects, i.e. scattering and shadowing related to intersections of grain boundaries with the surface [Mch2012] are less important in thin films than in bulk materials.



(a)

(b)



(c)

**Figure 3.1.3:** Scanning PL measurements at 80 K: BB Map (a); D1 Map (b); PL spectra at marked positions A (defect-poor region) and B (defect-rich region) (c).

In addition to the defects, other structures are visible in the BB Map (Fig. 3.1.3(a)). The main direction of these structures is perpendicular to the defects. That corresponds to the topography of the glass substrate. However, the exact structures are more complex than the

### 3. Electron beam crystallized large grained Si thin films

simple lines in the transmission images. The structures can be described as regularly ordered fish scales. Note that the structures are not present within the defects. However, the regions exhibit almost no defect-related luminescence (Fig. 3.1.3(b)), even at low temperatures.

Regions exhibiting the fish scale structure will be referred as defect-poor regions. They are characterized by a very homogenous BB intensity over wide ranges of the sample, neglecting the regular oscillations of the fish scale structure. That indicates silicon grains of quite high and possibly more important homogeneous quality. In contrast to the BB luminescence, there are very strong temperature dependences of the defect-related luminescence (DRL). As mentioned, no luminescence from defects can be observed at room temperature. But at lower temperatures there are very intense PL signals. A D1 Map shows this in figure 3.1.3 (b). Note that the DRL intensities vary over more than 1 order of magnitude depending on the spatial position. PL spectra are given in figure 3.1.3(c) of a defect-poor region (position A) and a defect-rich region (position B). There one can see that defect-poor regions show a rather low intensity of D1 and D2. In contrast to this, defect-rich regions show intense luminescence of all four D-lines. It should be emphasized that position B exhibits quite low DRL intensity compared to other regions (see: very intense DRL in upper part of figure 3.1.3(b)). That indicates a wide range of defect concentrations within the samples.

The presence of these well-known luminescence features (BB and all four D-lines) without any other luminescence signals shows that thin films of large grained silicon exhibit the same PL spectra as bulk mc-Si. Nevertheless, due to the specific properties of the samples the interpretation of the PL spectra is still different to bulk mc-Si. In case of bulk mc-Si, the defect-poor regions would be classified as silicon with a quite low concentration of defect and a quite high material quality, according of the low intensities of D1 and D2. But in case of the investigated thin-film samples the PL spectra represent luminescence averaged above grains and grain boundaries, despite of the fact that the grain boundaries are not visible in PL Mapping. Therefore the grains, in the defect-poor regions, can be classified as almost defect free. The remaining luminescence of D1 and D2 has to be attributed to the grain boundaries.

Up to now, it can be summarized that the PL spectra in large grained Si thin films are the same as in bulk mc-Si. However, from bulk materials it is known that detailed investigations of several PL features can reveal further information. In the next part, it will be checked if this is the same on large grained Si films. Therefore, some PL features will be discussed more detailed.

At first, the temperature behavior of the BB luminescence will be investigated on several positions of the sample. It is determined by two factors in case of bulk Si. One is the radiative recombination coefficient  $B(T)$  and the other is the minority carrier lifetime  $\tau(T)$  (see: [Klo2011] and sub-chapter 1.2.1). Both parameters are associated with the material quality. Therefore, the temperature behavior allows an indirect and restricted approach to non-radiative defect.

The temperature behaviors of defect-rich (A-D) and defect-poor regions (E-G) are shown in figure 3.1.4. Note that the positions A and B differ to those in figure 3.1.3. An increase of BB intensity can be observed with decreasing temperature in defect-poor regions. This is well known as normal temperature behavior of BB luminescence. It should be emphasized that there are just slight difference in the increase of the BB intensity over the entire sample. This confirms the suggested homogeneity of the defect-free regions. Defect-rich regions show various temperature behaviors, reaching from normal temperature behavior (decreasing BB intensity with increasing temperature) to the opposite anomalous temperature behavior



### 3. Electron beam crystallized large grained Si thin films

(increasing BB intensity with increasing temperature). Also remarkable are the strong deviations of the BB intensity in defect-rich regions. All this denotes enormous variations in the defects concentration.

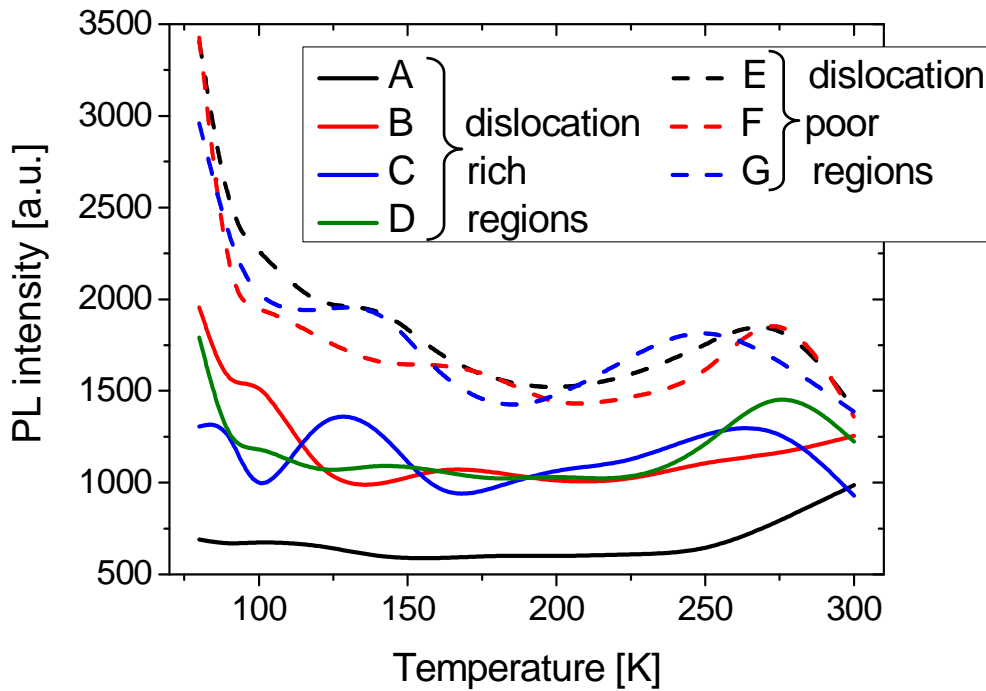
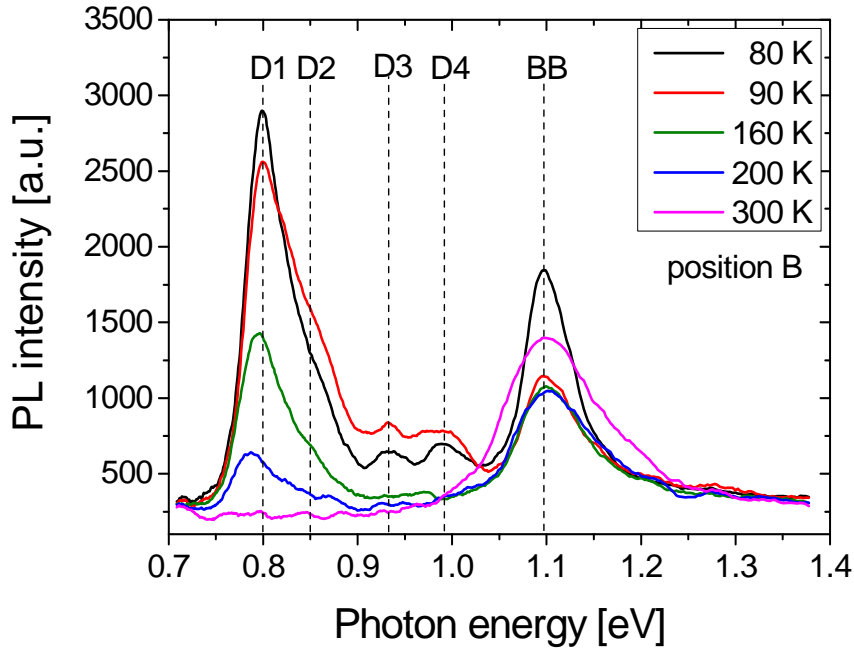


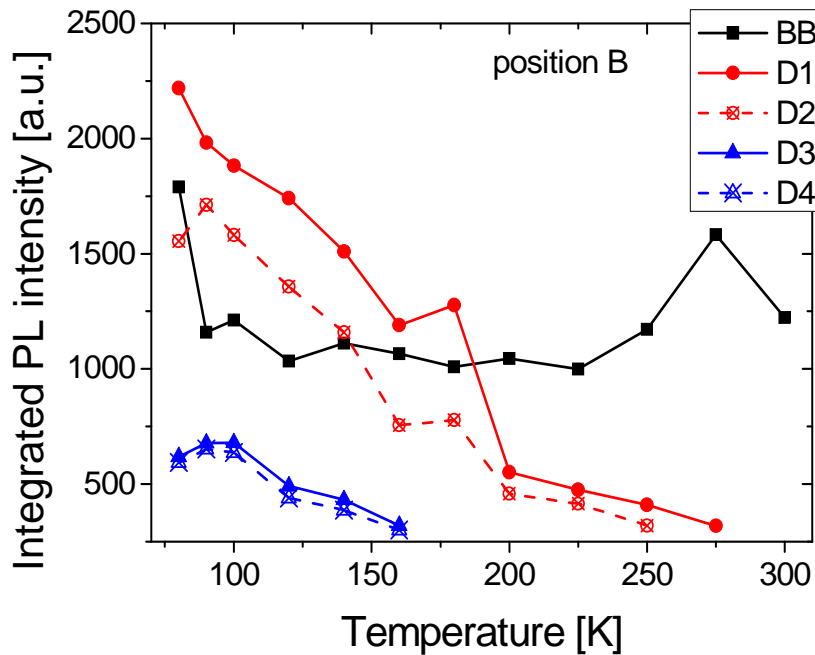
**Figure 3.1.4:** Temperature behavior of BB intensity: Defect-poor regions show homogeneous normal temperature behavior; defect-rich regions are show various temperature behaviors.

The other PL feature, which shall be investigated, is the temperature behavior of the D-lines. Thereby the relation between D1 and D2 on the one hand and D3 and D4 on the other hand will be discussed here. That is illustrated in figure 3.1.5 at the position B in figure 3.1.3. It represents the investigated temperature behaviors of several positions in defect-rich regions. D3 and D4 can only be detected at temperatures below 160 K. Both exhibit a strong relation in this temperature range, which is characterized by an almost constant ratio of the intensities. In contrast to this, no clear relation can be detected between D1 and D2. These behaviors can be explained by changing participations of excess carriers on several radiative transition paths. Where excess carriers change between the participation of several radiative transitions (BB, D1, D2 and the pair D3, D4). That is well illustrated in figure 3.1.5(a). The increase of temperature from 80 K to 90 K leads to an enormous drop of the BB intensity and a weaker drop of D1. These drops represent a change of an amount of excess carriers to other radiative transitions paths related to D2 and the pair D3, D4, which are characterized by increasing PL intensities. Almost all carriers take part in the radiative transition related to BB luminescence at higher temperatures. Of course, there is also a change of carriers between radiative and non-radiative transitions, which become dominant at higher temperatures. The important point here is the pairing of D3 and D4, which was previously observed by T. Arguirov et al. [Arg2003]. It is one of the key-arguments for the widely accepted theory of D3 as phonon replica of D4. T. Arguirov et al. suggested the pairing of D3 and D4 as reason for the observed constant intensity ratio found by investigations of the spatial distribution of the D-lines on mc-Si. In this way, the measured constant temperature dependence obtained on electron-beam crystallized thin-film samples add and support the previous work. That proves the transferability of knowledge from bulk mc-Si to the investigated Si thin films.

### 3. Electron beam crystallized large grained Si thin films



(a)



(b)

**Figure 3.1.5:** Temperature behavior of several PL peaks: PL measurements were performed at position B in Fig. 3.1.3. PL spectra at selected temperatures (a); integrated PL intensity of BB, D1, D2, D3 and D4 in a temperature range from 80 K to 300 K (b). The ratio D3/D4 is almost constant in contrast to the ratio D1/D2.

Another interesting defect-related feature is the spatial distribution of DRL. This is shown by a closer look on the spatial distribution of the luminescence of BB and D-lines in figure 3.1.6. It is a higher magnification of the region around the very strong DRL in the upper part of figure 3.1.3(a, b). The BB Map shows sharply bounded defects, with a special focus on the ring-shaped structure in the middle. The distributions of D1(D2) and D3(D4) are shown in the middle and right image, respectively. Thereby the relations between D3 and D4, as phonon

### 3. Electron beam crystallized large grained Si thin films

replica, and D1 and D2, unknown origin, are used. The D3(D4) Map shows a very clear anti-correlation with the BB Map. But the luminescence in the D1(D2) Map is not sharply bonded but rather spatially blurred. For a better comparability, profiles were extracted along the red arrows of BB and all four D-lines. The plot below the maps shows these profiles in normalized PL intensities. The luminescence intensities of BB and D3, D4 are characterized by a very clear spatial anti-correlation, marked by dashed lines. Contrary to this, D1 and D2 exhibit an overlap with defect-poor BB intensity of almost 400  $\mu\text{m}$ , marked by the arrows.

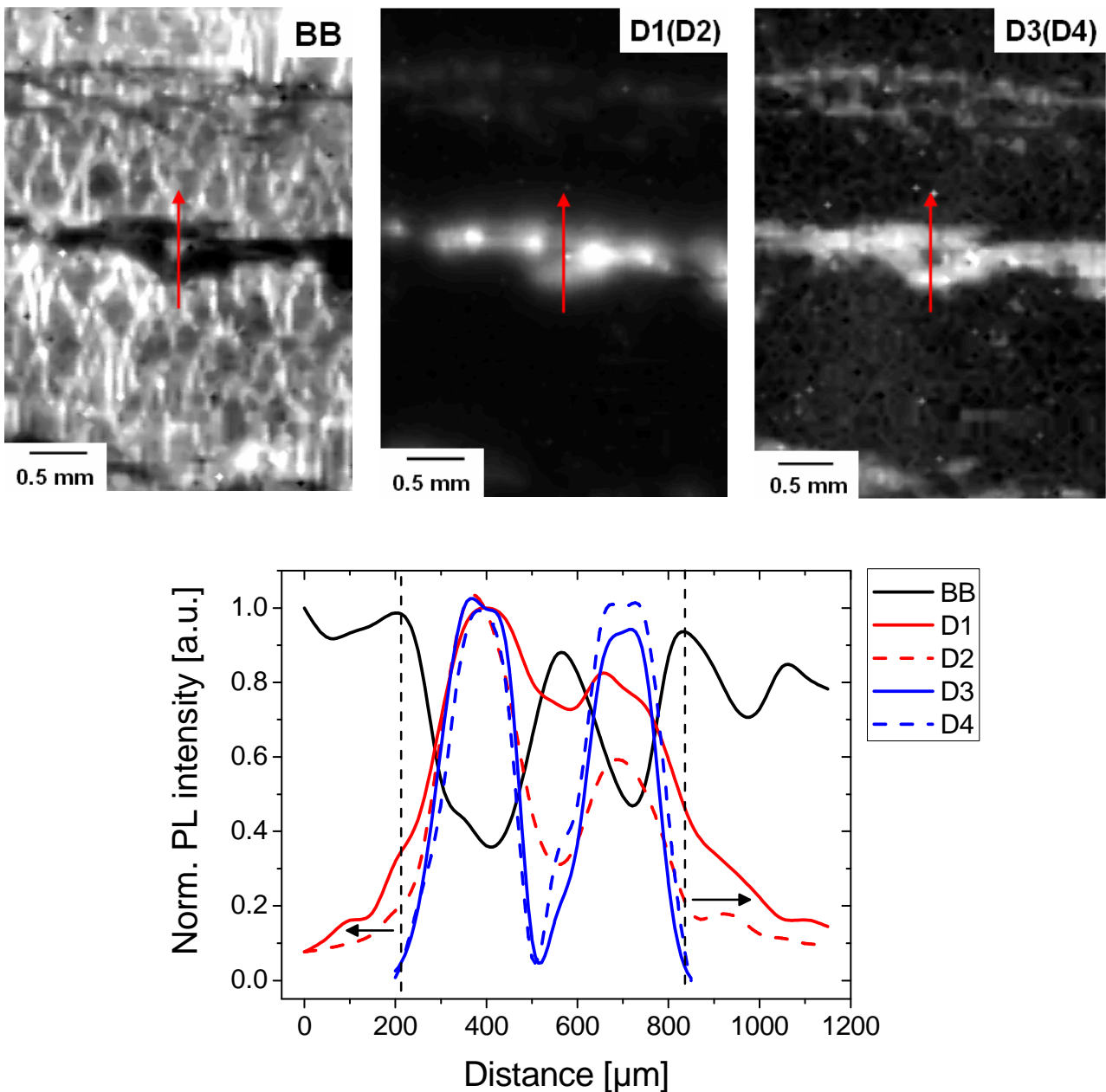


**Figure 3.1.6:** Spatial distribution of PL at 80 K: BB and D3(D4) show sharply bonded defects (clear anti-correlation) in contrast to D1(D2). Profiles along the red arrows of BB and D-line luminescence show an overlap of D1 and D2 of almost 400  $\mu\text{m}$  with the defect-poor BB intensity.

### 3. Electron beam crystallized large grained Si thin films

Interpretation of this feature needs an approximation of the spatial resolution of PL at the specific samples. In general, the spatial resolution of PL is limited by two factors. The first one is the laser spot size of about 100  $\mu\text{m}$ . This value is just a rough limit of resolution. It can be reduced by using lower step sizes during the scan considering the higher generation of excess carriers in the center of the Gaussian laser beam profile. The profiles in figure 3.1.6 were obtained by using a step size of 30  $\mu\text{m}$ . However, this amplification of the spatial resolution could be compensated in case of high diffusion length of the generated excess carriers. In case of very high diffusion length, the spatial resolution could be even worse than 100  $\mu\text{m}$ . But at these samples, the diffusion length was estimated to 7.5  $\mu\text{m}$  to 8  $\mu\text{m}$  by EBIC and time resolved PL measurements [Sei2011, Amk2011]. This is in good agreement with the actual thickness of the silicon layer, extracted from the transmission measurements. That means the diffusion length is limited by the layer thickness due to interface recombination. Therefore, the influence of diffusion on the spatial distribution can be neglected, in this specific case. In summary, the spatial resolution of PL at these samples can be expected to be less than 100  $\mu\text{m}$  and the observed overlap of D1 and D2 is no artifact.

The overlap is hard to explain. After discussions with D. Amkreutz it seems to be possible that the overlap could indicate an uncompleted gettering process. The SiC:B layer includes aluminum, which was identified as very efficient for defect gettering in EFG-wafers (edge defined film fed growth) [Hah2003]. According to D. Amkreutz EFG can be used as reference for the investigated samples. Of course, this is a highly speculative explanation and should be understood as a weak evidence for uncompleted gettering. Another approach of explanation deals with the fact that such behavior was previously observed in bulk mc-Si [Mch2012]. Normally, grain boundaries appear 'broader' for D1 or D3 than for BB signal at low temperatures. This may be a result of extended diffusion length nearby the grain boundaries due to gettering of impurities by grain boundaries and 'cleaning' of the nearby grain regions from non-radiative defects. The clear anti-correlation of D3/D4 and BB at 80 K, despite the increased carrier diffusion length suggests a strong suppression of BB due to non-radiative recombination on D3/D4-related dislocations. This more general explanation seems to be more reliable. However, both approaches deal with the impact of gettering.

## 3.2 Results and Discussion – EBIC investigations

One of the most characteristic features of the samples is the specific spatial distribution of BB luminescence in defect-poor region – the fish scale structure. This feature is also present in EBIC images. That leads to the conclusion that the structure indicates variations of carrier recombination at the Si/SiC:B interface [Sei2011]. In that case, the fish scale structure represents more or less enhanced non-radiative interface recombination at the interface. It would be interesting to compare the impact of this on PL and EBIC. This could allow better estimations of the magnitude of interface recombination in both techniques, which is one requirement to correct or minimize this thin-film effect.

PL BB Maps and EBIC images give almost the same information in case of bulk mc-Si. Both images show a rough distribution of carrier lifetime, despite of the fact that PL is an optical and EBIC an electrical technique. A direct comparison of both techniques urgently requires the equal depth of carrier generation in PL and EBIC, especially in case of thin-film samples. Therefore, the EBIC beam energy was fixed at 10 keV. This gives a penetration

### 3. Electron beam crystallized large grained Si thin films

depth of around  $1\ \mu\text{m}$  [Kan1972]. C. Krause performed the EBIC measurements at room temperature to avoid cooling problems due to the thermal insulation of the glass substrate (see: sub-chapter 2.3).

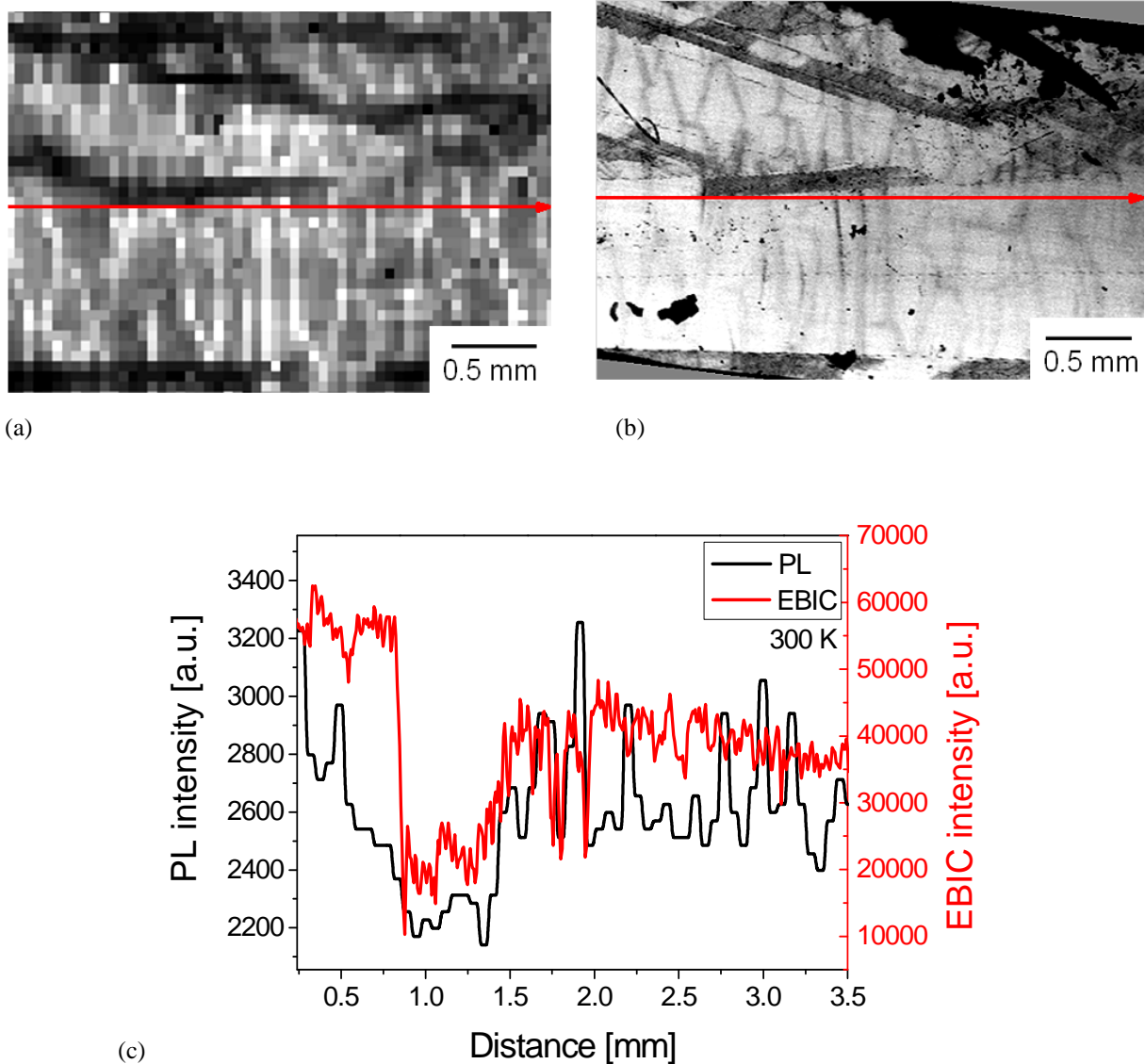


**Figure 3.2.1:** Comparison of the impact of interface recombination in PL and EBIC at 300 K: PL BB Map (a); EBIC image (b); profiles along the red arrows show dominance of interface effects in case of PL and dominance of defects in case of EBIC (c).

Figure 3.2.1 show the BB Map and the EBIC image of the same area. As expected in both images defects are characterized by low intensity. But the interface-related fish scale structure appears as regular peaks in case of PL and as regular drops in case of EBIC. Moreover, profiles extracted along the red arrows show that the impact of the interface is more dominant than the impact of defects in case of PL. In EBIC, the defects are the dominating feature and the interface signals are quite low. The reason for these contrary behaviors could be the difference in the detection of the signal. An excess carrier, which recombines non-radiative at the interface, leads to a reduced EBIC current directly. So the EBIC signal is only influenced by the recombination activity at the interface. But in PL, luminescence light has to leave the sample structure to become detected additionally. This process of light uncoupling might be

### 3. Electron beam crystallized large grained Si thin films

influenced by optical properties of the interface, such as regular scattering of the luminescence. Therefore, the image of the interface recombination obtained by EBIC seems to be more reliable. However, it can be summarized that PL Maps are dominated by the interface structure and EBIC images by the defect structure on these specific electron-beam crystallized Si thin-film samples.

#### **Summary and conclusion:**

Investigations of the electron-beam crystallized large grained Si thin-film samples on glass substrate can be used as a first step to answer the key-question about the transferability of knowledge/methods from bulk mc-Si to thin-film Si.

It is possible to use the PL Imaging setup for transmission measurements to investigate the actual layer thickness as well as the topography of the layers just by easy adjustments because of the quite thick absorber layer. The obtained results are helpful to understand specific spatial distributions in PL and EBIC.

Scanning PL spectroscopy exhibits luminescence features known from bulk mc-Si, such as BB and all four D-lines. Moreover, these luminescence features behave like in bulk Si, including the temperature behaviors and the spatial distribution between BB and DRL. Nevertheless, note that the interpretation of the luminescence features must be still related to the sample properties. For instance, the missing grain boundaries in the BB Map can only be explained considering the lower sample thickness and/or the special process of crystallization.

It was possible to eliminate parasitic luminescence (e.g.: luminescence from glass) due to the thick Si layer at this specific sample. Nevertheless, at thinner samples the corrected silicon spectrum should be available by deconvolution of the measured spectra into parasitic luminescence and luminescence from Si.

The critical point for the presence of luminescence features, known from bulk mc-Si, is the grain size. It can be summarized that large grained Si films exhibit luminescence spectra like bulk mc-Si, possibly overlapped by thin-film effects. Note that the spatial distribution can be still affected by thin-film effects. PL investigations are limited by two critical distances. The first one is the generation depth of excess carriers (Attention: physically defined penetration depth is not equal to actual generation depth (see: sub-chapter 2.3 – Parasitic luminescence signal)), which determines the observed luminescence spectra. The second distance is the diffusion length of the carriers, which determines the spatial distribution of luminescence due to interface recombination. The need of this separation is clearly visible at the investigated thin-film samples. The laser light does only excite the silicon absorber. Therefore, the detected spectra show only luminescence from Si. Nevertheless, the diffusion length is limited by the layer thickness and so the spatial distribution is dominated by the interface. Moreover, the strong impact of the recombination at interfaces reveals the different distribution of diffusion length within the silicon layer. Regions of high silicon quality/diffusion length exhibit a spatial distribution, which is dominated by recombination at the interface (defect-poor regions). Regions of low Si quality/diffusion length (defect-rich regions) do not show the regular interface-related fish scale structure (see: figure 3.1.3(a)). These regions are

### 3. Electron beam crystallized large grained Si thin films

characterized by a diffusion length of 1  $\mu\text{m}$  or even less [Sei2011]. Therefore the excess carriers are not able to reach the Si/SiC:B interface there.

The process of interface recombination is well understood, but the actual impact seems to be more complicated than expected. Its influence differs between several investigation techniques, such as EBIC and PL. This can lead to incorrect interpretations of the sample properties, but it can also offer possibilities to avoid misinterpretation by comparisons of several techniques. That emphasizes the need of combined techniques for the characterization/investigation of thin-film samples. Thereby it is probable that the effect cannot be corrected completely. However, it is necessary to identify interface recombination to give a rough estimation of its impact on the measured data.

## 4. Solid-phase crystallized poly-Si thin films with subsequent rapid-thermal processing

The investigations in this chapter represent the middle step in the evolution from bulk mc-Si to pure thin-film Si phases. The deposited Si layer is originally deposited in amorphous form and subsequently crystallized by solid-phase crystallization (SPC). The typical grain size is in the order of a few micrometres [Ber1997]. The obtained material is called poly-Si to separate it from mc-Si (grain sizes of few millimeters) on the one side and microcrystalline silicon (grain sizes of 10 to 30 nm) on the other side. For further improvements of the material quality the silicon is additionally treated by hydrogen passivation (HP) and several rapid-thermal processes (RTP). That allows the investigation of the impact of the RTP-treatments. Due to the lower absorber thickness ( $\sim 1.6 \mu\text{m}$ ) the cell structure is more complex in comparison to the previous chapter, where the thick Si layer absorbs the entire laser light. Therefore deconvolutions of the spectra are necessary, especially to eliminate the luminescence from glass. The main questions in this chapter will be focused on the observed PL features and their comparability with bulk mc-Si. This could give a lower limit of grain sizes, where Si exhibits luminescence like in mc-Si. It is already known that the luminescence of a-Si:H and  $\mu\text{c-Si:H}$  differs significantly. The other question deals with the influence of RTP-processes, which are typical for subsequently crystallized thin films. A group around C. Becker and S. Steffen at HZB produced the samples. The reported results are focused on the PL investigations of the samples. Further results and descriptions that are more detailed can be found in [Bec2011].

### Investigated samples:

A  $1.6 \mu\text{m}$  thick a-Si film with about  $2 \times 10^{16} \text{ cm}^{-3}$  boron doping was deposited by electron-beam evaporation of silicon and co-evaporation of boron from an effusion cell on 1 mm thick glass substrate (Schott Borofloat 33).

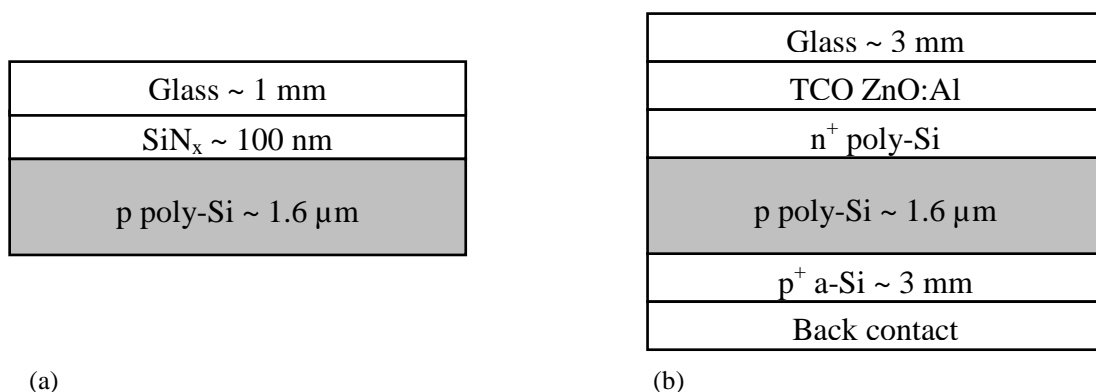


**Figure 4.1:** Sketch of the samples for PL investigations (a); and completely processed solar cell structure (b)



#### 4. Solid-phase crystallized poly-Si thin films with subsequent rapid thermal processing

Figure 4.1 shows the partially process solar cell structure for PL investigations (Fig. 4.1(a)) in comparison to the completely processed one (Fig. 4.1(b)) with additional contacts (back contact), etc. The glass was coated with a 100 nm thick SiN<sub>x</sub> as wetting-layer and diffusion barrier in an industrial PECVD reactor. The deposited a-Si was crystallized by a SPC-process at 600 °C for 20 hours. The achieved grain size is in the order of 1 to 3 μm. In a next step hydrogen passivation (HP) was applied to passivate dangling bonds. A remote plasma source has been used to expose the samples to atomic hydrogen for 20 minutes at 620 °C [Kee2005] in this work. During cool down the plasma is maintained active in order to avoid re-effusion of hydrogen. The plasma is extinguished at a temperature of 340 °C.

After that several RTP-processes, either Rapid-thermal annealing (RTA) or Laser-annealing (LA) or Zone-Melting-Recrystallization (ZMR), the excitation by focused halogen lamp [Poo2006], were used for subsequent treatment of the samples. Table 4.1 gives an overview of all investigated samples with the corresponding RTP-processes and temperatures. A sample only treated by HP is used as reference. Note that treatment by ZMR and LA create wave-like structures on the surface of the poly-Si film. These structures are visible to the naked eye (probable structure size of few tens of micrometres) and can affect PL investigations by light scattering etc.

<b>Treatment</b>	<b>RTP-temperature</b>
<b>only HP</b>	/
<b>HP + RTA</b>	1050°C
<b>HP + LA</b>	860°C 1230°C 1400°C
<b>HP + ZMR</b>	1050°C 1060°C

**Table 4.1:** Overview of the investigated samples treated with several RTP-processes and the corresponding RTP-temperatures (hydrogen passivation (HP), Rapid-thermal-annealing (RTA), Laser-annealing (LA) and Zone-Melting-Recrystallization (ZMR)).

## 4.1 Results and Discussion – PL investigations

For the PL investigation, the samples were placed with the glass side on the top. That guarantees good thermal contact to the sample holder. But the most important reason is that it avoids luminescence from glass, which is strongly and unpredictable filtered by the Si layer (see: sub-chapter 2.3).

PL spectra at 80 K exhibit no BB luminescence but very intense luminescence around the spectral position of the D1-line, which is related to dislocations in mc-Si. The absence of BB luminescence might be a result of the high density of grain boundaries due to the low grain size. That indicates low diffusion lengths and high defect concentrations. Note that previous

#### 4. Solid-phase crystallized poly-Si thin films with subsequent rapid thermal processing

PL investigations on similar samples treated by SPC, RTA and/or HP exhibit very similar luminescence spectra [Mch2012a].

Two peaks can be distinguished, whereas the first one is localized between 0.79 and 0.805 eV (labeled as ‘Peak 1’) and the second one between 0.815 and 0.865 eV (labeled as ‘Peak 2’). The exact peak parameters (peak positions, ratios of the peak intensities and temperature behaviors) strongly depend on the RTP-processes (RTA, LA or ZMR) and the RTP-temperatures. The impact of the several processes is illustrated in figure 4.1.1.

Note that the spectra are normalized to focus on spectral deviations. The different PL intensities are partially caused by changes between the two radiative transitions paths represented by the peaks (see: chapter 3). In case of only HP treated samples the dominant amount of excess carriers take part in the radiative transition responsible for ‘Peak 1’. That leads to a very high maximum PL intensity. But with increasing RTP-treatment more and more carriers take part in the radiative transition related to ‘Peak 2’. Therefore, the maximum PL intensity decreases, because of a constant level of generated electron-hole pairs. This change is more intense in case of LA and ZMR, but rather low in case of RTA. That is clearly visible in figure 4.1.1, where the intensity of ‘Peak 2’ differs strongly between the ZMR sample and the RTA one, despite of the same RTP-temperature. Additionally to that, there is a decrease of the total PL intensity with increasing RTP-treatment/-temperature. One can see that all RTP-processes lead to various blueshifts of both peaks. The influences on the intensity ratio of the two peaks are more complicated. The temperature behavior (Fig. 4.1.1(b)) differs strongly between only HP-treated poly-Si samples and those treated by RTP-processes additionally. A dominant ‘Peak 1’ and a rather low ‘Peak 2’ characterize HP-samples. Both exhibit a strong increase of intensity with decreasing temperature of more than three orders of magnitude. In contrast to this, the PL intensities of LA- and ZMR-treated samples show a strong saturation at lower temperatures and the splitting into the two peaks becomes more significant. Surprisingly the RTA samples show only a slight increase of ‘Peak 2’ and the temperature behaviors are very similar to that one of only HP-treated poly-Si. Another very important feature is that both peaks shift to lower energies with increasing temperature, whereas ‘Peak 1’ achieves  $\sim 0.77$  eV at room temperature.

These results allow first statements about the nature of the luminescence in RTP-treated poly-Si. The deviations in the peak position from D-lines at 80 K and the peak position around 0.77 eV at room temperature indicate oxide precipitates (OP’s) [Taj1994, Taj1995] as origin for the luminescence instead of dislocations associated with D1. The presence of high oxygen concentrations were proved by TOF-SIMS measurements obtaining values up to  $10^{19}$  cm<sup>-3</sup>. It can be assumed that the impact of thermal donors (TD’s) is negligible, according to the high RTP-temperatures. TD’s should be completely transformed into oxygen complexes. The dashed curve shows the spectrum of OP’s, which are often observed in mc-Si wafers. The clear spectral deviation can be associated to different thermal treatments leading to other types of OP’s. It can be assumed that the deviations between the several RTP-processes is related to transformations of OP’s present in only HP-treated poly-Si (‘Peak 1’) to other types of precipitates (‘Peak 2’), whereas the effect of RTA is quite low. The excitation by panchromatic light (ZMR) seems to be slightly more efficient than the excitation by monochromatic light (LA) accordingly to the temperatures in table 4.1.

#### 4. Solid-phase crystallized poly-Si thin films with subsequent rapid thermal processing

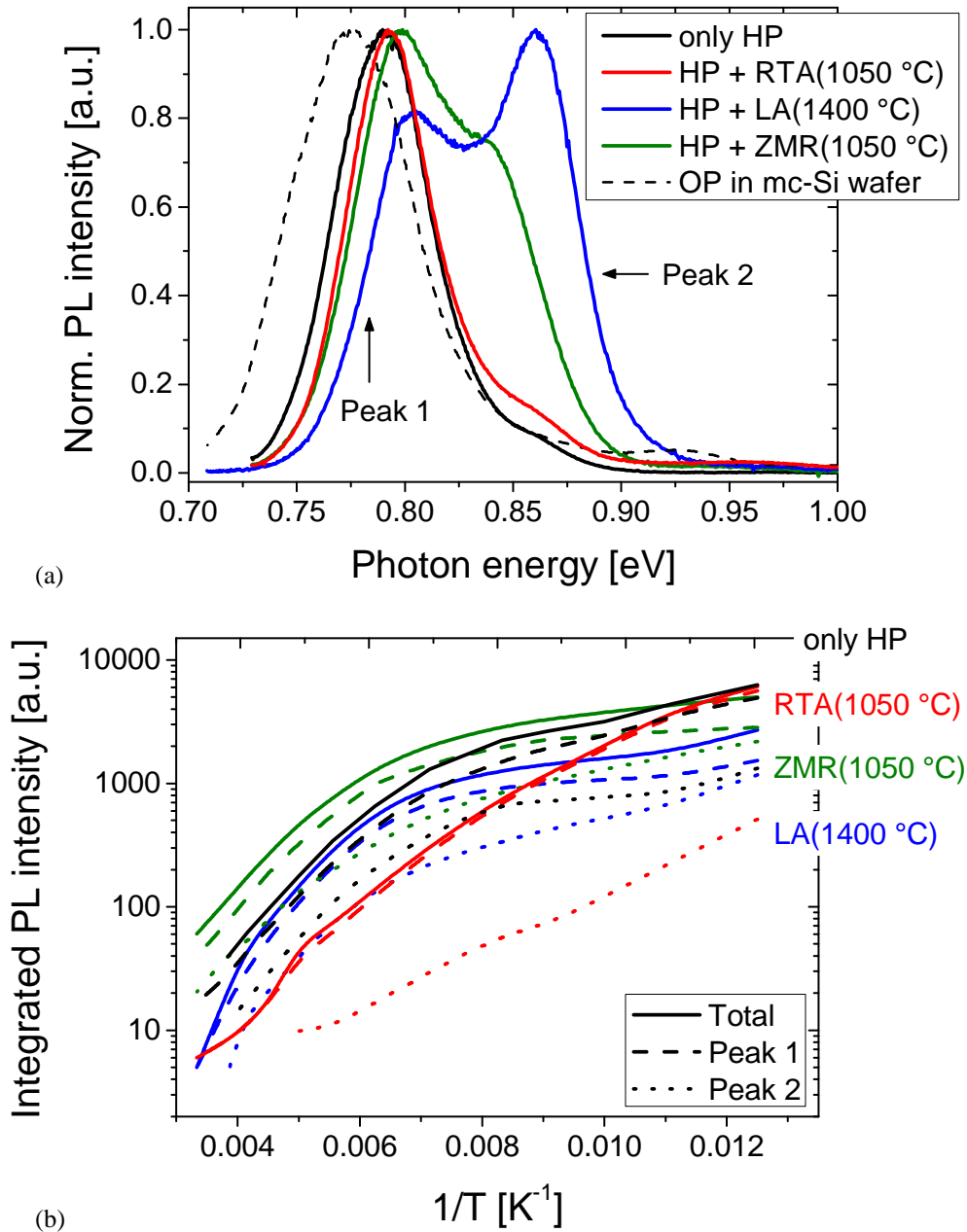


**Figure 4.1.1:** PL investigations on subsequently treated poly-Si samples: Spectra of only HP-treated samples, additionally RTA, LA and ZMR treated ones at 80 K. The dashed curve shows spectrum of oxide precipitates (OP) in bulk mc-Si wafer (a); temperature behaviors of the single peaks and the total luminescence intensity (b)

PL Mapping investigated the spatial distribution of luminescence at 0.79 eV and exhibits more or less strong deviations (Fig. 4.1.2). These deviations are mainly related to variations of the thickness of the silicon layer. In case of LA and ZMR samples, it is additionally amplified by light scattering at the surface topography. It should be emphasized that even samples without wave-like structures (only HP, HP+RTA) do exhibit small variations of the Si layer thickness. That is proved by spatial variations of the luminescence intensity coming from the glass substrate. The deviations of the PL intensity are caused by two factors. The first and dominating one is caused by differences in the layer thickness. The much smaller second one is caused by probable variations of Si quality. Unfortunately, it is not possible to separate both factors. This would be necessary to decide if the oxide precipitates are gettered at grain

#### 4. Solid-phase crystallized poly-Si thin films with subsequent rapid thermal processing

boundaries [Cav1993] or possibly strongly localized as more extended precipitates. However, a spatial correlation on the investigated samples was very improbable from the beginning because of the low grain size in comparison to the spatial resolution of the PL setup. The dominating part of spatial deviations is clearly caused by variations of the Si layer thickness, which becomes additionally amplified by interface recombination and light scattering at the rough sample surface.

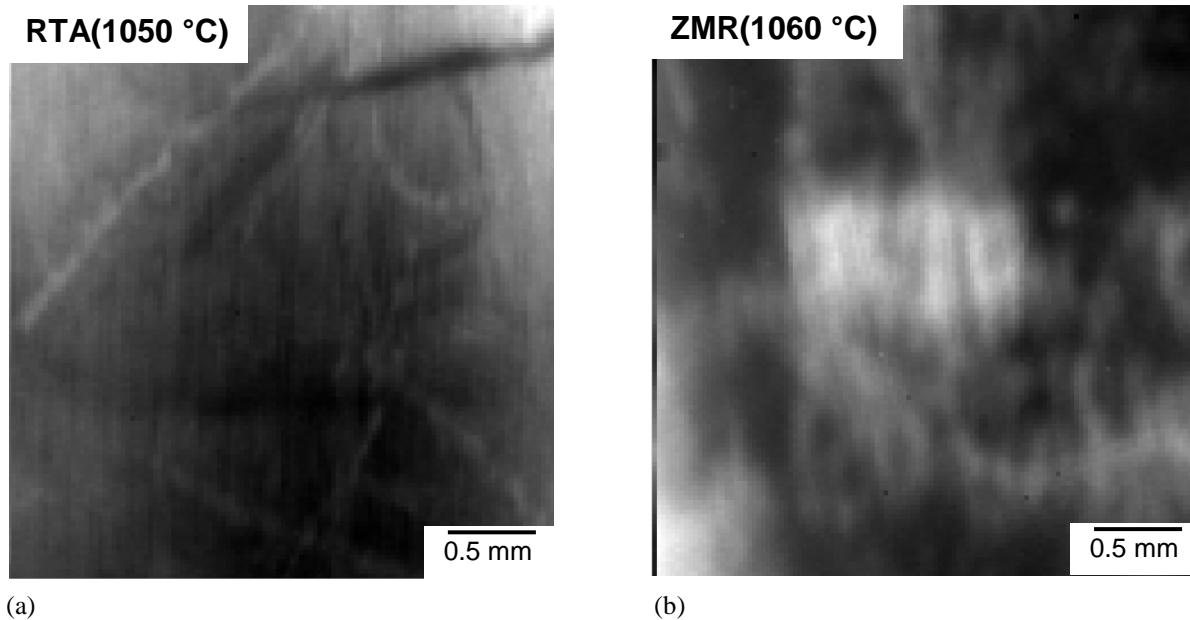


**Figure 4.1.2:** PL Maps of poly-Si samples at 0.79 eV: Spatial deviations are mainly caused by variations of the Si layer thickness. RTA treated samples exhibit deviations in the order  $\pm 10\%$  (a); ZMR and LA treated samples exhibit much higher deviations ( $\pm 50\%$ ) amplified due to wave-like structures on the surface (b).

The impact of the exciting laser power on the spectra was investigated, too. It turned out that both peaks show linear dependences up to  $\sim 60$  mW (standard power for investigation: 50 mW). That limits the low injection regime. At higher laser powers ( $\sim 75$  mW) the intensity of 'Peak 2' begins to increase stronger, relatively to 'Peak 1'. This might be an evidence for further laser annealing. However, the sample starts to degrade and therefore it cannot be investigated further.

The exact peak position of 'Peak 1' was studied more detailed to investigate the influence of the RTP-temperature. In case of 'Peak 2', such investigation seems less promising, because of the higher peak width indicating a mixture of several types of OP's. It is well known that the peak position of DRL can be affected by internal electric fields, application of stress etc. So it can be expected that the peak shift is related to one of these parameters, which might be caused by the several RTP-processes. That is illustrated in figure 4.1.3. There one can see that the blueshift of 'Peak 1' correlates with the RTP-temperature. Different slopes, depending on the exact RTP-process, characterize the increase of peak energy with increasing RTP-temperature. According to Drozdov et al. [Dro1977], a blueshift is an indication for compressive stress. This approach seems to be quite reliable here. Dashed lines mark the magnitude of increasing stress, but note that these lines are guides for the eyes only. The stress level is rather low in case of RTA contrary to LA and ZMR. That can be explained

#### 4. Solid-phase crystallized poly-Si thin films with subsequent rapid thermal processing

considering the specifics of the RTP-processes. In a RTA-oven, the entire cell structure is heated and so the poly-Si layer is quite relaxed. In contrast to that, LA and ZMR only heat poly-Si and the glass substrate keeps cold. The induced temperature gradient must create stress within the Si layer and this is visible in more intense slopes in figure 4.1.3.

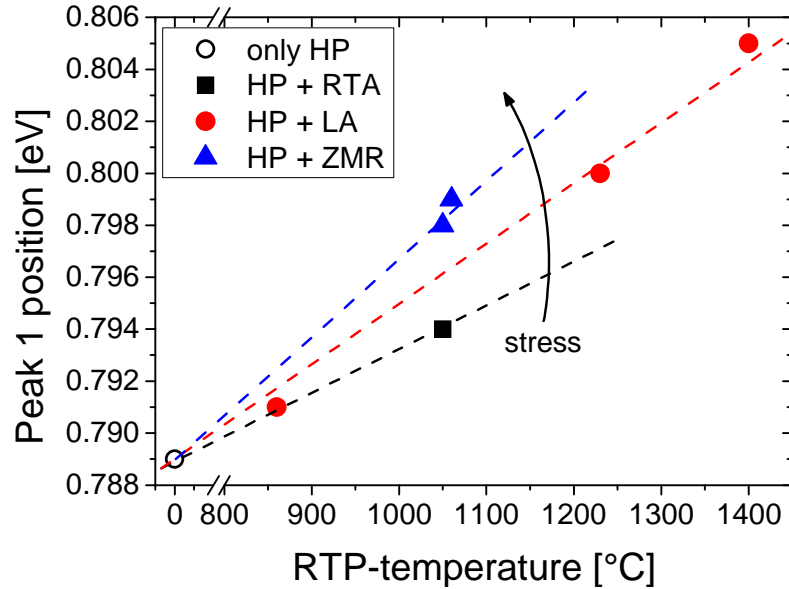


**Figure 4.1.3:** Position of ‘Peak 1’ depending on the RTP-process and –temperature: The different slopes might indicate different levels of stress in poly-Si layer induced by temperature gradient between cold glass substrate and heated Si. The dashed lines are guides for the eye only.

In the next step, the investigations were focused on the LA-series, because of the widest range of RTP-temperatures. The temperatures range from 860 °C to 1400 °C. The corresponding normalized PL spectra are shown in figure 4.1.4 at 80 K.

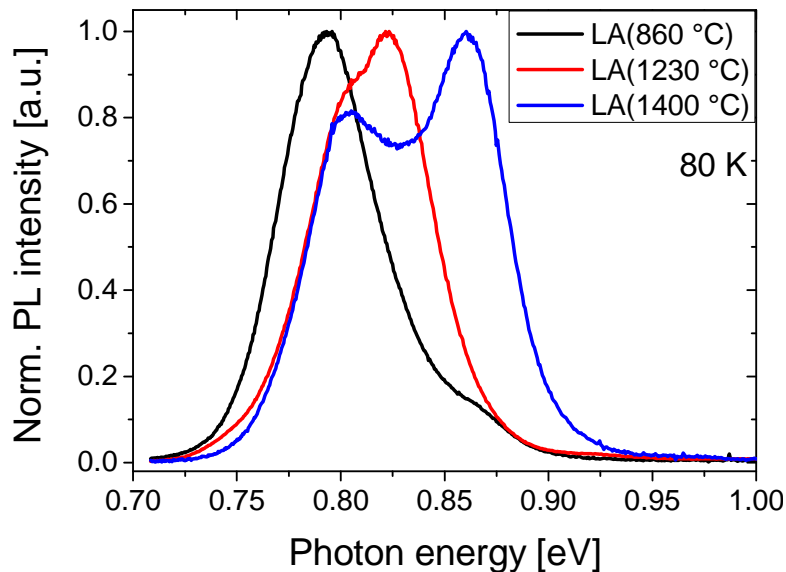


**Figure 4.1.4:** Normalized PL spectra of LA-treated poly-Si at 80 K at several RTP-temperatures.

#### 4. Solid-phase crystallized poly-Si thin films with subsequent rapid thermal processing

It is obviously clear that ‘Peak 1’ represents other types of OP’s as ‘Peak 2’. But it is not clear if the blueshift of ‘Peak 2’ is also related to stress, like in case of ‘Peak 1’, or to further transformation of the oxide precipitates. Interactions between the two types of OP’s are possible, too. The detected thermal broadening of the two peaks supports the possibility of such interactions. In case of one dominant type of precipitates (LA at 860 °C) exhibits ‘Peak 1’ a temperature-induced broadening of the peak width (FWHM) from 41 meV (80 K) to 65 meV (300 K). In contrast to this, in case of two almost equal types of precipitates (LA at 1400 °C) no significant broadening is observed. Moreover, between 80 K and 150 K a slight shrinking of the width of ‘Peak 1’ is detectable with increasing temperature, which is possibly compensated by a stronger broadening of ‘Peak 2’.

A plot of the temperature dependent peak energies of both peaks (Fig. 4.1.5) shows indications for interactions between the precipitates, too. The blueshift of ‘Peak 1’ is not detectable at temperatures above 220 K. Thermal effects hide the deviation in this temperature range. The shift becomes clearly visible at lower temperatures, up to the level illustrated in figure 4.1.3.

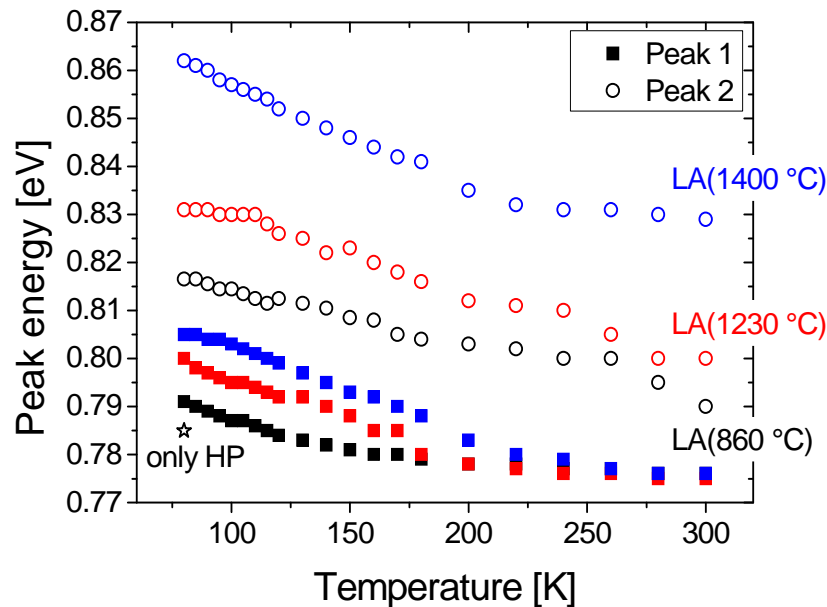


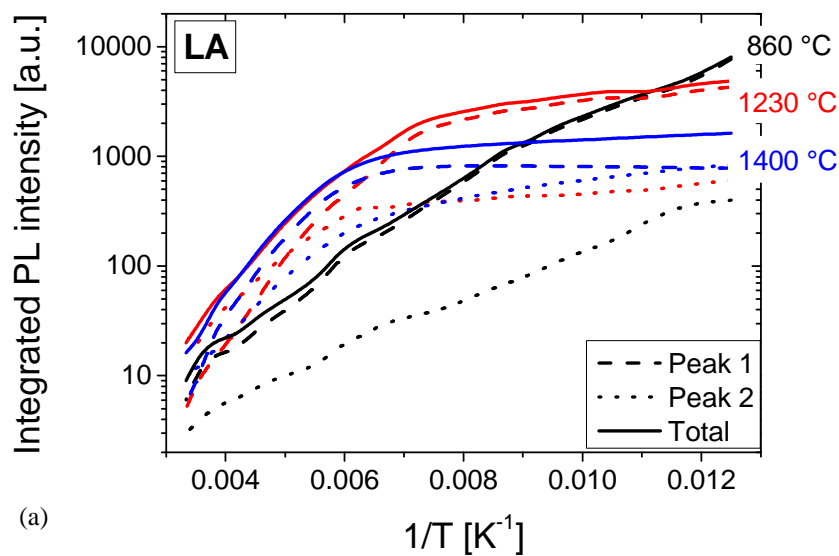
**Figure 4.1.5:** Peak energies of LA-treated poly-Si samples: The splitting of the peak energies of ‘Peak 1’ at lower temperatures indicates internal stress. The peak position of the only HP-treated sample (star) is similar to the C-line from literature, which is associated to  $C_i-O_i$ -complexes [Kür1989].

Following the assumption of interacting OP’s, the sample only treated by HP should be the one, which is most suitable to study the type of oxide precipitates represented by ‘Peak 1’. Then SPC process itself would create the original OP structure. Its peak position is shown as a star in figure 4.1.5. It should be almost unaffected by stress-induced peak shifting. The corresponding peak energy is 0.789 eV at 80 K. That is very close to the spectral position of the C-line of 0.79 eV at 10 K [Kür1989]. It was observed in carbon- and oxygen-rich samples and therefore associated with carbon-oxygen complexes ( $C_i-O_i$ ). It must be separated from the more popular P-line at 0.767 eV [Piz2000, Min1981]. The P-line is related to OP’s created at about 450 °C and vanishes at 550 °C - 600 °C. So the temperature range is another point, which excludes the presence of the P-line in the investigated samples, considering the temperature of 600 °C for 20 h (SPC) and above 1000 °C (RTP). However, these comparisons

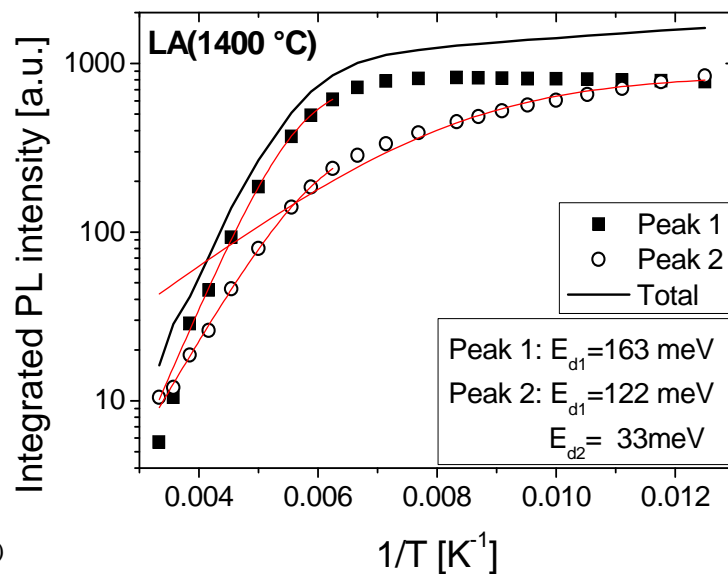
#### 4. Solid-phase crystallized poly-Si thin films with subsequent rapid thermal processing

with literature data should not suggest that ‘Peak 1’ is equal to the C-line. This is not true according to the broadness of ‘Peak 1’ and the very restricted comparability between Cz-Si/FZ-Si (literature) and the investigated poly-Si thin films. It should just indicate that the observed OP’s might be similar to those associated with the C-line. TOF-SIMS measurements revealed carbon concentrations up to  $10^{18} \text{ cm}^{-3}$ . Therefore, the presence of carbon-oxygen complexes is very probable.

The exact origin of ‘Peak 2’ is less clear. It keeps quite broad even at low temperatures. That could indicate a mixture of several types of OP’s within this peak. However, oxygen-related precipitates were observed previously around 0.85 eV [Ken2003]. Thereby it was found that sharp lines, such as P- and C-lines, vanish after higher/longer heat-treatment. Instead of these single lines broad bands appear. That was partially understood as further evolution of the OP’s to more complex and extended oxygen complexes [Taj1994].



(a)



(b)

**Figure 4.1.6:** Temperature behavior of PL intensities of LA-series: Comparison of all three LA-samples with a focus on increasing splitting into two peaks (a); Fitting of the LA-samples exhibit two deactivation energies  $E_{d1}$  and  $E_{d2}$  in several temperature ranges on the example of 1400 °C RTP-temperature (b)

#### 4. Solid-phase crystallized poly-Si thin films with subsequent rapid thermal processing

Another approach to the physical nature of the oxygen-related defects can be obtained by careful analysis of the deactivation energies from the temperature dependent PL measurements. That is demonstrated for the LA-series in figure 4.1.6. At first, it is clearly visible that the total PL intensity at 80 K decreases with increasing RTP-temperature. This could be explained by out diffusion of oxygen during the RTP-process. That would lead to a decreasing concentration of radiative impurities (OP's) with increasing RTP-temperature and therefore to a reduced PL intensity. This assumption was also assisted by TOF-SIMS measurements.

In case of one dominant peak (LA at 860 °C) shows the plot an almost linear behavior over the entire temperature range. The corresponding deactivation energy was extracted by fitting to 91 meV. With increasing RTP-temperature decreases the absolute PL intensity at 80 K and starts to saturate at certain level of PL intensities and saturation temperatures  $T_{Sat}$ . This is obviously correlated with the increasing splitting into the two peaks. Other features of the plot are also affected by the increasing RTP-temperature. These features are the deactivation energies. Attempts to fit these energies exhibit significant deviations between fitting curves and data points (Fig. 4.1.6(b)). That can be explained by the fact that both fitting models (bound-to-free and bound-to-bound deactivation model (equations (1.2.2.7) and (1.2.2.9)), assume the presence of only one deactivation mechanism over the entire temperature range. Therefore, the existence of two temperature dependent deactivation mechanisms must be assumed, whereas the saturation temperature marks the transition between them. Therefore, it is possible to extract two deactivation energies. One for the high temperature range  $E_{d1}$  and one for the low temperature range  $E_{d2}$ . All these parameters are summarized in table 4.1.1.

LA-series	Peak energy at 80 K [eV]	Deactivation energy $E_{d1}$ [meV]	Deactivation energy $E_{d2}$ [meV]	Saturation temperature $T_{Sat}$ [K]
860 °C	0.791	$91 \pm 3$	/	/
	0.817	$57 \pm 4$	/	/
1230 °C	0.800	$124 \pm 5$	$34 \pm 6$	~ 140 K
	0.831	$96 \pm 4$	$9 \pm 4$	
1400 °C	0.805	$163 \pm 3$	Not able to fit	~ 160 K
	0.862	$126 \pm 2$	$31 \pm 2$	

**Table 4.1.1:** Overview of parameters of the temperature behaviors of LA series

The data were obtained by fitting the bound-to-free deactivation model (equation (1.2.2.7)), but note that no significant differences exist between both models. It should be emphasized that the sum of the deactivation energies and luminescence peak energy is not equal to the bandgap of silicon. Therefore, the second deactivation mechanism does not represent the barrier between a lower defect level and the valence band as suggested by Dreckschmidt et al. [Dre2011]. The exact band diagram is unclear but a possible model is shown in figure 4.1.7. The deactivation energy  $E_{d1}$  represents the barrier between a deep trap ('Peak 1') and the conduction band. Following this,  $E_{d2}$  represents the barrier between the deep trap and a shallow trap ('Peak 2'). This transition becomes preferred at lower temperatures. It is indicated that both trap levels shift deeper into the bandgap with increasing RTP-temperature. This trap shifting is illustrated as grey bars in figure 4.1.7.



#### 4. Solid-phase crystallized poly-Si thin films with subsequent rapid thermal processing

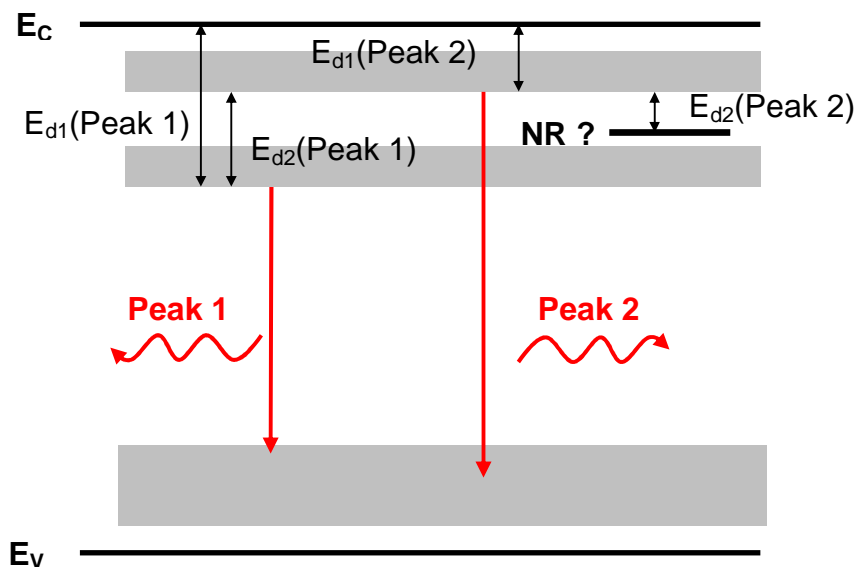


**Figure 4.1.7:** Model of the band diagram in case of the LA-sample. The grey bars mark the shift of the trap levels with increasing RTP temperature and probable band-like defect levels. Small deviations of the energy might be caused by fitting errors. The exact position of the non-radiative trap (NR) is unknown.

The bars are also used to indicate the probability of band-like defect levels instead of discrete ones. That is very probable because of the broadness of both defect peaks in PL. Note that this model seems to be quite good considering the fact that the deviations of the equation (4.1.1) are in the order of the fitting errors.

$$E_{d1}(Peak 1) - E_{d1}(Peak 2) - E_{d2}(Peak 1) = 0 \pm Error \quad (4.1.1)$$

It is probable that both radiative transitions end in a band-like trap level, as illustrated in the figure. A special case represents the sample treated at 1400 °C, where the PL intensity of ‘Peak 1’ exhibits a maximum around the saturation temperature (see: Fig. 4.1.6(b)). Therefore, it was not possible to fit the corresponding energy  $E_{d2}$ . This behavior can be explained by transitions of excess carriers from the deep trap ( $E_{d1}(Peak 1)$ ) to the shallow trap ( $E_{d1}(Peak 2)$ ). Such changes in the participation of excess carriers on several transitions were already discussed in this work (see: chapter 3). However, two approaches of explanations can be suggested. The first one is that the real value of  $E_2$  is hidden due to a higher occupation of excess carriers from the deep trap  $E_{d1}(Peak 1)$ , which would lead to an amplification of the luminescence signal. The second approach assumes the presence of an additional non-radiative trap (NR). This possibility is assisted by the fact that even the total PL intensity can only be fitted by two temperature dependent deactivation mechanisms. It is not possible to determine the exact position of this non-radiative trap within the bandgap. But it must be energetically close to both trap levels as shown in figure 4.1.7.

Actually, the oxide precipitates represent a very complex defect structure, which cannot be completely understood by PL investigations alone. A better approach could be given by Deep-level transient spectroscopy (DLTS), but it requires pn- or Schottky-junctions from front side and glass side. Such junctions mark a high challenge in sample preparation and are not fulfilled, up to now.

## 4.2 Results and Discussion – Raman investigations

All poly-Si samples were also investigated by Raman spectroscopy. The main idea of this was to check the assumed presence of stress within the Si films due to the RTP-processes. Figure 4.2.1 shows normalized Raman spectra of the LA-series compared as example for the other RTP-processes. Cz-Si was used as reference for Si without significant level of stress. There one can see that the crystalline Raman peak of poly-Si shifts to the peak position of Cz-Si with increasing RTP-temperature. This behavior is also typical for the other RTP-processes. It seems to disagree with the expected increase of stress with increasing RTP-temperature. Increasing stress should lead to an increasing shift of the peak position. Another important feature of the spectra is a significant broadening of the peak compared to Cz-Si. This broadening is an evidence for the actual reason of the unexpected direction of peak shifting. It is well known that the peak position and peak width of the crystalline Raman peak are related to the crystalline quality of silicon. Therefore, there are two contrary effects affecting the Raman spectra of the investigated poly-Si samples. The first one is an increasing crystalline quality with increasing RTP-treatments and the other one is an increase of stress.

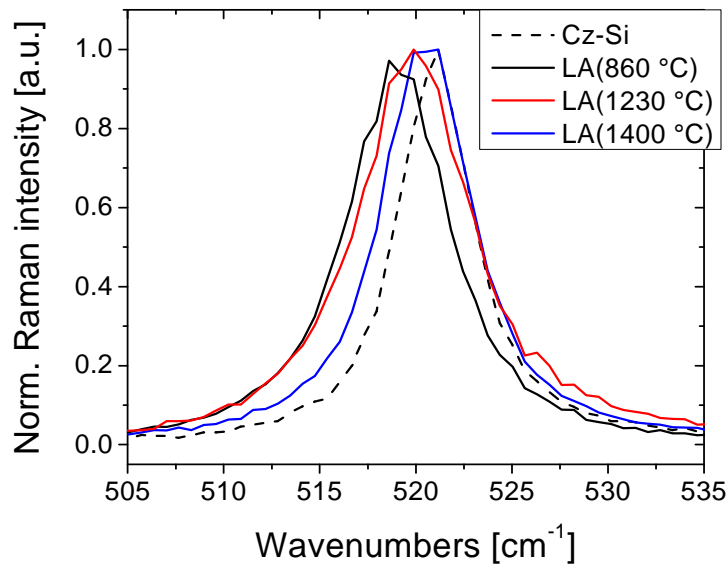


**Figure 4.2.1:** Normalized Raman spectra of LA-samples: Shift and broadening of the peak can be observed in comparison to Cz-Si.

The peak position and peak width (FWHM) are extracted from Raman spectra of all samples and summarized in figure 4.2.2 for a detailed analysis of these two features. Thereby two different reference levels are considered. The first one is Cz-Si (dashed lines) as highly crystalline silicon without a significant level of stress. The other one is the sample only treated by hydrogen passivation (HP). Peak position and peak width do not show a clear dependence on the RTP-temperature as observed in PL (see: Fig. 4.1.3). In general, there is a rough shift to higher Raman frequencies and lower peak widths with increasing RTP-temperature. Nevertheless, the relations between the different RTP-processes do not agree with the PL measurements completely. That means especially the quite moderate peak width/peak position of the only HP-treated sample compared to the samples treated by LA. At

#### 4. Solid-phase crystallized poly-Si thin films with subsequent rapid thermal processing

higher RTP-temperatures, the features become closer to those of Cz-Si. In case of LA-samples treated at 860 °C there is a slight shift to lower Raman frequencies and peak widths. This might be an indication for tensile stress within the poly-Si samples. That is contrary to PL, where compressive stress is indicated. This can be explained considering the high surface sensitivity of Raman in comparison to PL, which is sensitive to the entire sample thickness. It might be possible that different types of stress are induced in the surface and the bulk of the sample. A comparison of the induced stress between the different RTP-processes allows the conclusion that LA-samples are mostly affected by stress. This is contrary to PL, where higher stress is indicated in ZMR-treated poly-Si. However, both techniques exhibit RTA-treatment as the technique, which exhibits the most relaxed poly-Si at the corresponding temperature. This is probably due to the simultaneous heating of Si and glass.

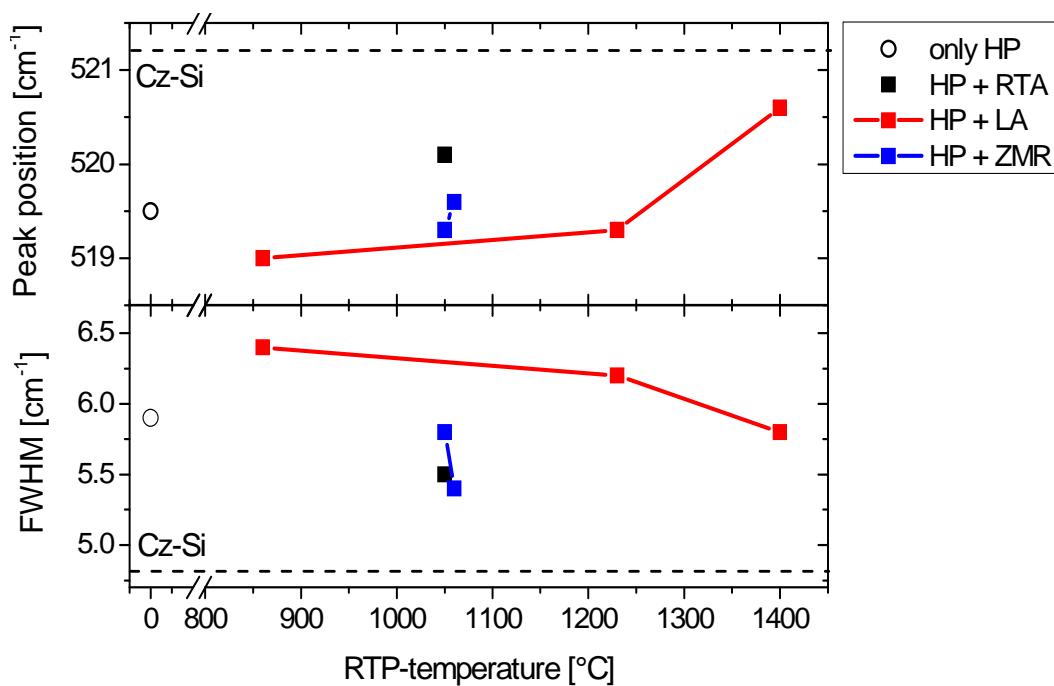


**Figure 4.2.2:** Peak parameter of Raman spectra at poly-Si: Peak position and peak width (FWHM) exhibit complex dependences on RTP-temperature. Probable reasons are contrary directions of the peak shift due to increasing crystalline quality and increasing stress level with increasing RTP-temperature. Data for Cz-Si are shown as reference for highly crystalline Si without significant stress.

However, the main effect on the Raman spectra is the increasing crystallinity at higher RTP-temperatures. Therefore, the peak parameter of the LA-treated sample at 1400 °C are quite close to those of Cz-Si despite of the expected high level of stress. It would be extremely risky to extract a value of the induced stress from Raman spectra, even at RTA-samples due to the contrary influence of the increasing crystallinity. Despite of all treatments the obtained crystalline quality of the poly-Si films exhibit significant deviations compared to Cz-Si. This is probably the main reason for the quite worse solar cell parameters of the thin-film solar cells compared to those of wafer-based Si. Therefore, further improvements of the crystallization and treatment processes are necessary.

#### 4. Solid-phase crystallized poly-Si thin films with subsequent rapid thermal processing

### **Summary and Conclusion:**

PL investigations on poly-Si thin films with subsequent RTP-processes exhibit luminescence features, which are clearly related to several types of OP's. These precipitates differ from those observed in bulk mc-Si. That is mainly caused by different temperature treatment during the RTP-processes. It is important that the lower layer thickness or other thin film effects (e.g. luminescence from glass) do not cause the deviations. It is very probable that the high density of grain boundaries causes the absence of BB luminescence. It can be concluded that PL investigations on such Si films with very low grain sizes and high defect concentrations should be focused on defect-related luminescence (DRL). In such cases, BB luminescence is not more the characteristic feature of silicon.

The used PL setup cannot resolve the spatial distribution due to the small grain size. This would require setups that are more complex. However, it is not clear if such setups would be able to resolve the grains because of light scattering at the wave-like surface structures. PL Maps just exhibit variations of the layer thickness. Interface recombination might also affect the spatial distribution of PL.

In summary, the investigations confirm that Si grains with a size of a few micrometres exhibit PL features that are comparable to bulk mc-Si. Of course, effects of the thin-film sample (e.g. luminescence from glass substrate) must be still considered. That allows knowledge transfer from bulk Si to thin-film ones and backwards. For instance, the observed oxide precipitates could be further evolution steps of those observed in bulk mc-Si at elevated temperatures.

Comparative investigations by PL and Raman lead to supplementary results about the stress, which is induced during the RTP-processes, and the increasing crystalline quality of poly-Si. Thereby it turned out that both effects have a strong impact on Raman. Nevertheless, it is still possible to separate them due to the fact that PL is not sensitive to the increasing crystalline quality. Therefore, it is more adequate to investigate the stress. But note that different types of stress are assumed within the samples. Thereby Raman is sensitive to tensile stress on the surface of the sample and PL to compressive stress within the entire sample, especially at the interface to the substrate.

## 5. Other thin-film Si phases – amorphous and microcrystalline Si

In the last chapter thin-film samples were investigated, which are characterized by thin layers and small Si grains, but a quite simple structure. That will be changed now. This chapter marks the last step in the evolution from bulk mc-Si to thin film Si phases. That is related to an increasing complexity of the entire sample stack and silicon phases, which do not exist or do not have any applications in thin-film form. These phases are hydrogenated amorphous (a-Si:H) and microcrystalline silicon ( $\mu\text{c-Si:H}$ ). They are characterized by high absorption coefficients (see: sub-chapter 1.3). This advantage allows reduced thicknesses of the absorber layer of about one micrometer. One of the main disadvantages of a-Si:H and  $\mu\text{c-Si:H}$  is the affinity to light-induced degradation (LID). That includes phase modification by laser (e.g. laser-induced crystallization [Im1993]) as well as high sensitivity to light exposure by sunlight (e.g. Staebler-Wronski effect [Sta1977]). It should be mentioned that the affinity for LID is significantly higher in a-Si:H than in  $\mu\text{c-Si:H}$ . This must be considered during investigations by laser-based techniques (e.g. PL, Raman). Currently used solar cell concepts reduce LID by using thinner layers of a-Si:H layers or using  $\mu\text{c-Si:H}$  instead of a-Si:H. Both ways are combined in tandem cells, whereas a very thin a-Si:H top cell is used to absorb the blue part of the solar spectrum. The remaining red part is absorbed in a  $\mu\text{c-Si:H}$  bottom cells. There are various techniques to deposit Si, but in the last years chemical-vapor deposition (CVD) becomes commonly used. A special form, plasma-enhanced CVD (PECVD) was used to deposit all investigated samples in this chapter.

A completely processed a-Si:H/ $\mu\text{c-Si:H}$  tandem cell on glass substrate will be investigated in the first part of this chapter. The second part describes more detailed investigations on a substructure of this cell - 500 nm thick  $\mu\text{c-Si:H}$  layers on glass. All three key-questions of this work will be discussed in these two parts of the chapter. It is obviously clear that the first key-question ('How to correct/minimize thin-film effects?') will be especially important during the investigations of the entire tandem cell. The second key-question will be less important due to the fact that a-Si:H and  $\mu\text{c-Si:H}$  do not have any applications or do not even exist in bulk thickness (especially  $\mu\text{c-Si:H}$ ). Nevertheless, it is still possible that investigation techniques/methods, which were originally designed for bulk mc-Si, can be transferred to thin-films after adjustments. The main key-question in this chapter is the third one: 'What can be learned about the physical aspects of typical thin-film Si-phases?' This will be discussed in the second part of this chapter, whereas a focus will be on observations of the transformation process from amorphous to microcrystalline silicon.

## 5.1 Characterization of thin-film a-Si:H/ $\mu$ c-Si:H tandem solar cells on glass substrate

The challenging investigation process of a-Si:H/ $\mu$ c-Si:H tandem solar cells on glass substrate will be presented on a state-of-the-art tandem cell produced by Competence Centre Thin-Film- and Nanotechnology for Photovoltaics Berlin (PVcomB). First, energy dispersive X-ray spectroscopy (EDX) measurements were conducted to investigate the composition of the individual layers. Then, for detailed investigations of the a-Si:H and  $\mu$ c-Si:H layers scanning PL spectroscopy and EBIC were used. Both techniques were performed in different setup conditions on completely processed tandem cells as well as on partially processed ones. Therefore, it was possible to identify thin-film effects and to eliminate or minimize these effects on the characterization of the entire tandem solar cell – the first key-question of this work. The Raman-crystallinity of the  $\mu$ c-Si:H layer is determined by Raman spectroscopy. The results were published in [Klo2013].

### Investigated samples:

The investigated samples were a-Si:H/ $\mu$ c-Si:H tandem cells. They consisted of a hydrogenated amorphous silicon top cell (340 nm) to absorb the shorter wavelength of the sun spectrum. A hydrogenated microcrystalline silicon bottom cell (1.6  $\mu$ m) was placed above the a-Si:H top cell to absorb the longer wavelength of the sun spectrum. The Raman-crystallinity of the  $\mu$ c-Si:H cell should be slightly above 50 %. Both cells were p-i-n structures. The p- and n-layers had a thickness of around 15-40 nm, respectively. The silicon layers were deposited by PECVD on a 3.2 mm glass thick glass substrate (Float glass SGG Planilux). This was coated with front TCO consisting of SnO<sub>2</sub>:F (0.7  $\mu$ m). As a back contact a ZnO:Al/Ag layer with a total thickness of about 70 nm ZnO:Al and 200 nm Ag was deposited by sputtering. A sketch of the tandem cell design is shown in figure 5.1.1.

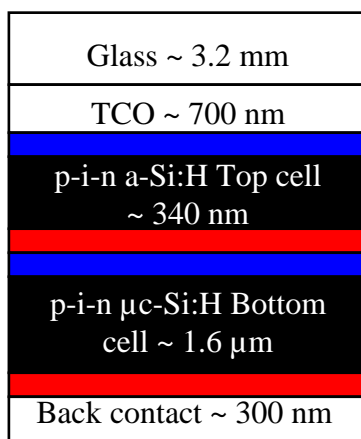


**Figure 5.1.1:** Sketch of the a-Si:H/ $\mu$ c-Si:H tandem cell. Blue, black and red are the p-, i- and n-layers, respectively.

## 5. Other thin-film Si phases – amorphous and microcrystalline Si

A laser scribing process of absorber and back contact layers structures the cells. Small areas of 1 cm x 1 cm solar cells on 30 cm x 30 cm mini-modules have been manufactured on a single substrate. A more detailed description of the process is given in [Ros2003]. Partially processed cells like a-Si:H single-junction cells were investigated, too. The cells were cut into small pieces for investigations in cross-section geometry.

### EDX investigations:

The complex cell design makes misinterpretations of the layer properties probably. That is amplified by the expected roughness of the layers. Therefore the planed solar cell structure was checked by EDX line scan along the cross-section of completely processed a-Si:H/ $\mu$ c-Si:H tandem cells. The measurements were performed by H.-M. Krause at 10 kV in an EVO MA 25 Scanning Electron Microscope (SEM) equipped with an EDAX drift detector. The normalized elemental signals are shown in figure 5.1.2 as function of the depth in the cell stack, counted from the back contact side. The depth distribution of the elemental components is in quite good agreements with the expected thickness of all layers. It should be mentioned that ZnO:Al and Ag are just the main components of the back contact. Smaller amounts of other components are added to improve the brazeability. The absence of abrupt elemental transitions corresponding to the different layers is caused by the experimental parameters, such as preparation process of the cross-section surfaces and the limited resolution of EDX. The sample itself contributes to this elemental overlap, too. A certain roughness of the layers improves the lateral current flow and light scattering. In general, EDX confirms the expected structure of the solar cell (see: Fig. 5.1.1).

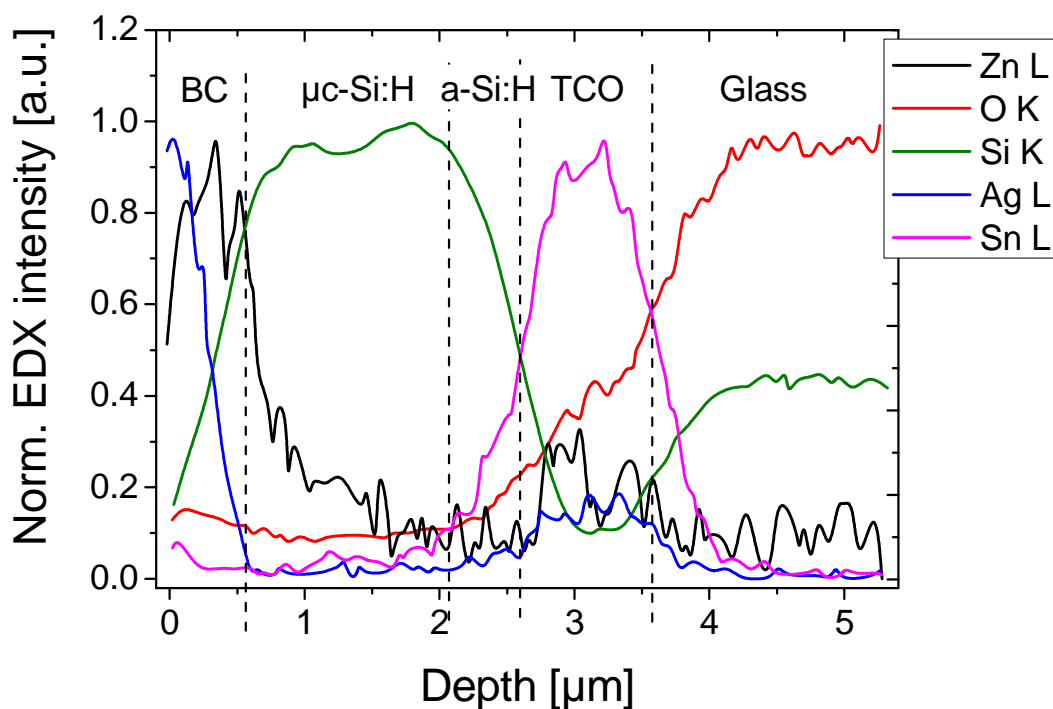


**Figure 5.1.2:** EDX line scan along the cross-section of a-Si:H/ $\mu$ c-Si:H tandem cell confirming the expected cell structure. The mixture of the layers is probably caused by the preparation of the sample cross-section, limited resolution of EDX and desired layer roughness.

### 5.1.1 Results and discussion – Optical investigations

#### PL investigations:

PL signals are characterized by very strong PL intensities, considering the typical effects of thin-films, such as interface recombination, low material volume etc. Actually, it is two times higher than the intensity of a completely processed bulk mc-Si solar cell at room temperature. At lower temperatures, the difference even increases. For scanning PL spectroscopy measurements, the samples were placed with the glass substrate on the top. This is necessary to prevent cooling problems due to the thicker glass.

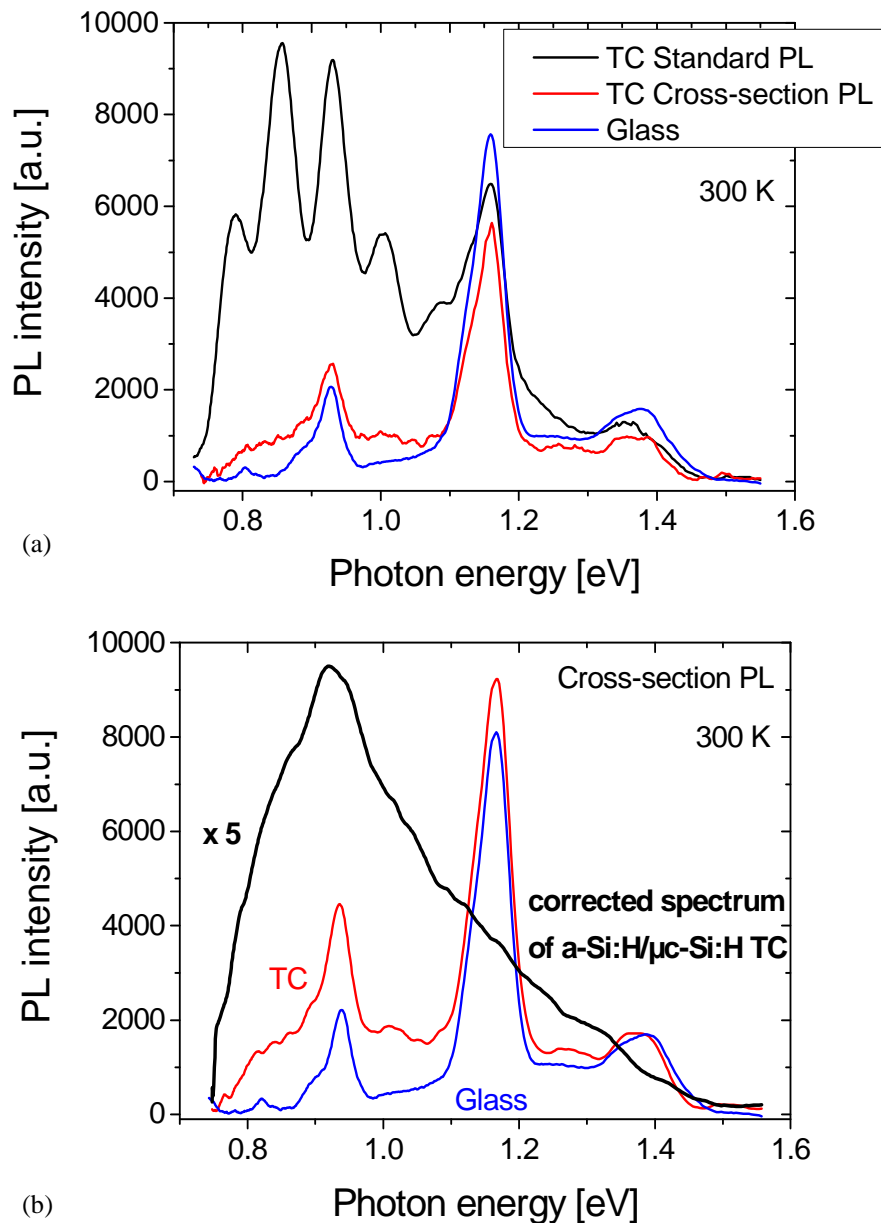


**Figure 5.1.1.1:** PL investigations on completely processed tandem cells (TC): Interference patterns created by specific cell structure are detectable in ‘Standard PL setup’ (a); corrected spectrum of a-Si:H/μc-Si:H TC only exhibits luminescence from a-Si:H layer in ‘Cross-section PL setup’ (b). Note that the low intensity is caused by inefficient collection of luminescence.



## 5. Other thin-film Si phases – amorphous and microcrystalline Si

Completely processed tandem cells (TC) are characterized by strong interference patterns because of the specific cell stack. Surprisingly these patterns are localized at the spectral positions of all four D-lines. This is illustrated by a comparison of measurements performed in ‘Standard PL setup’ and ‘Cross-section PL setup’ (Fig. 5.1.1.1(a)). Additionally a spectrum of the glass substrate alone is given for the sake of completeness. Spectral shifts of the interference peaks denote deviations in the stack thickness, especially on the borders of the mini-modules.

A deconvolution of the spectrum measured in ‘Cross-section PL setup’ leads to the spectrum of the silicon layers alone (Fig. 5.1.1.1(b)). Here the impact of a thin-film effect and ways to correct or minimize it is presented very impressive. The TCO does not contribute any PL signal in the investigated spectral range. It should be emphasized that the intensity of the spectrum is strongly affected by the different collection efficiency of luminescence signal from the thick glass layer and the thin silicon layers. Indeed, in ‘Standard PL setup’ the intensity of Si is much higher but dominated by specific interference patterns as mentioned in sub-chapter 2.3. As a result, the detected luminescence is a superposition of an intense part from glass and a strongly reduced part from silicon. This is why the intensity of the calculated spectrum is very low.

Comparisons of the calculated spectrum in figure 5.1.1.1(b) with spectra of pure a-Si:H and literature data [Eng1977, Str1980] show surprisingly that there is only PL signal detectable from the amorphous silicon layer. Microcrystalline silicon cannot be detected.

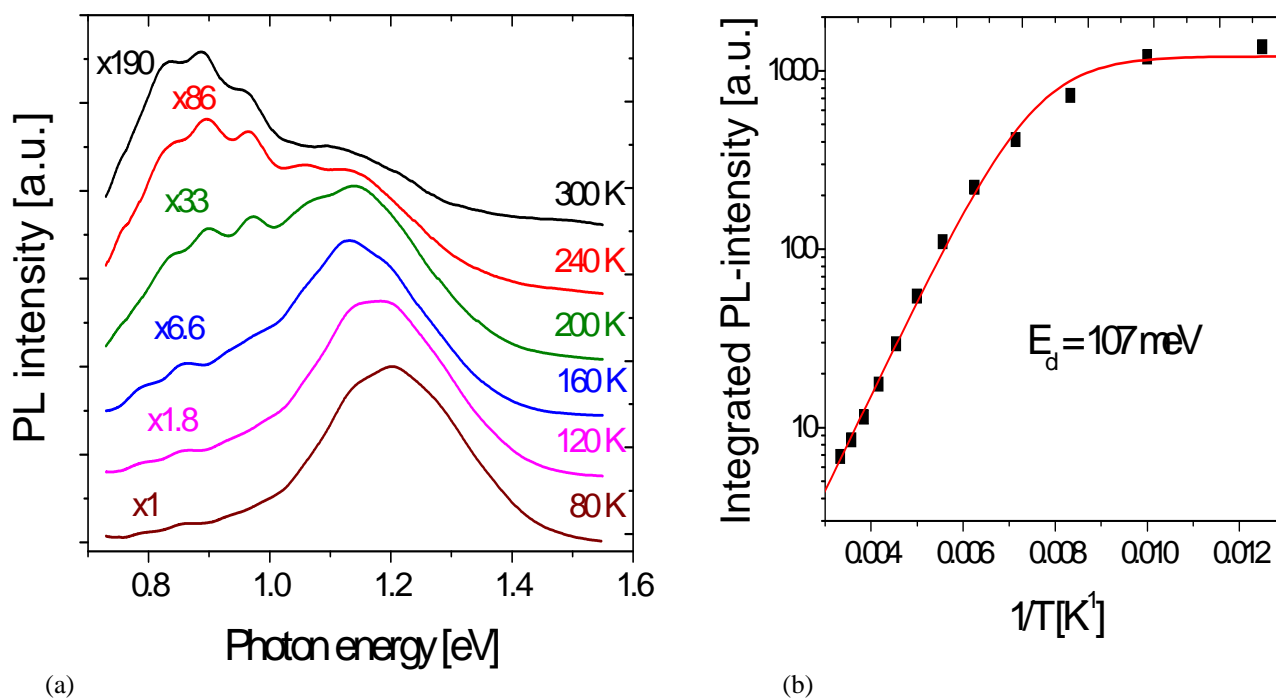


**Figure 5.1.1.2:** Temperature dependence of PL on completely processed a-Si:H/ $\mu$ c-Si:H tandem cells, obtained in standard PL setup: Corrected spectra from tandem cells (luminescence from glass removed and optical interferences suppressed) (a); integrated PL intensity vs. inverse temperature to extract the deactivation energy  $E_d$  (b).

To minimize any interface-related effects, which could influence the measurements the results were compared with investigations obtained in ‘Standard PL setup’ condition.

## 5. Other thin-film Si phases – amorphous and microcrystalline Si

Interferences appear in the spectra in this setup geometry. The temperature dependence of the PL spectra is shown in figure 5.1.1.2. The spectra are normalized on the maximum. The strong differences between the temperatures require multiplication factors are shown. Those are given for each curve. Luminescence signal from glass is removed and interference patterns are suppressed in the shown spectra. The smaller peaks between 0.8 eV and 1 eV at higher temperatures are induced by remaining interferences. At lower temperatures these peaks are less significant because of the very strong increase of the a-Si:H signal with decreasing temperature. Two material specific PL peaks can be distinguished. The first one is localized at 0.9 eV and dominant at high temperatures. It is related to traps within the bandgap of a-Si:H and often observed in doped a-Si:H with higher defect concentrations. At lower temperatures, the peak around 1.2 eV becomes dominant. It is related to transitions between tail states. The intensities of both peaks increase with decreasing temperature, but the increase of the tail-to-tail peak is much stronger. The deactivation energy  $E_d$  was extracted by fitting and is equal to 107 meV and shown in figure 5.1.1.2(b). This is just slightly lower as the 120 meV for bulk a-Si:H [Eng1977].

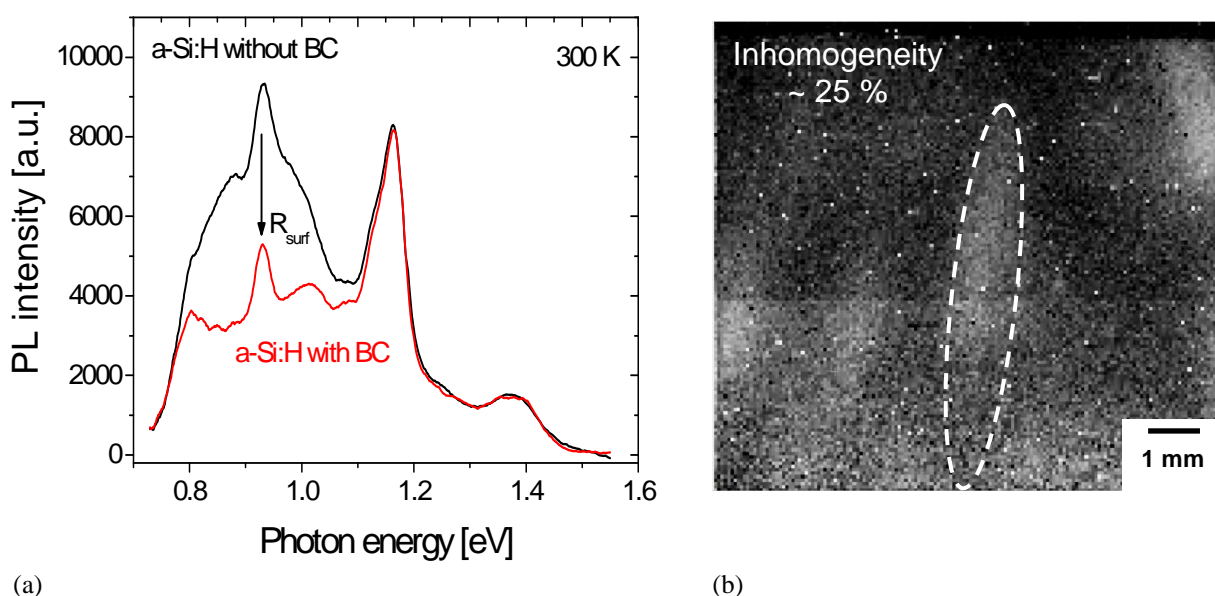


**Figure 5.1.1.3:** Influence of interface recombination on PL: Spectra of single-junction a-Si:H cell without and with back contact (BC) (a); spatial inhomogeneities in a-Si:H layer only detectable on cells without back contact (b).

Further, investigations of the spatial distribution were realized by scanning PL, which is only possible in ‘Standard PL setup’. Completely processed a-Si:H/ $\mu$ c-Si:H tandem cells were found to be characterized by a very homogeneous distribution of the entire PL features over wide ranges of the mini-modules. But investigations on partly processed cells show that this homogeneity is a result of thin-film effects, too. That is illustrated by investigations on single-junction a-Si:H cells, because of the strongly reduced impact of interference patterns. Figure 5.1.1.3(a) shows the luminescence spectra of single junction a-Si:H cells with and without back contact (BC). The typical defect-related peak at about 0.9 eV is only overlaid by the spectrum of the glass substrate (see Fig. 5.1.1.1). This defect-related peak strongly decreases on samples with back contact due to the enhanced interface recombination. A similar magnitude of recombination at the interface to the back contact was observed on completely processed tandem cells. The interface recombination suppresses spatial inhomogeneities in

## 5. Other thin-film Si phases – amorphous and microcrystalline Si

the amorphous silicon layer, which are only detectable on samples without back contact (Figure 5.1.1.3(b)). It should be emphasized that these inhomogeneities are not related to regions of nano- or microcrystalline silicon in the amorphous silicon matrix, which is often observed in PECVD processes [Ros2003]. The inhomogeneous regions are completely amorphous and could indicate regions of different defect densities. It is also implied that the interface between a-Si:H ( $\mu\text{c-Si:H}$ ) and the metallic back contact are characterized by a higher affinity to interface recombination than the interface to air. This result is very important concerning the transferability of knowledge from bulk materials to thin-film ones. Here the interface recombination does not only influence the spatial distribution of PL but also the PL spectrum.

More detailed investigations of several partially processed cells (e.g. single-junction a-Si:H cells, tandem cells without back contact, etc.) allowed a rough estimation of the contribution of each layer to the integrated PL intensity. That is illustrated in a scheme (Fig. 5.1.1.4).

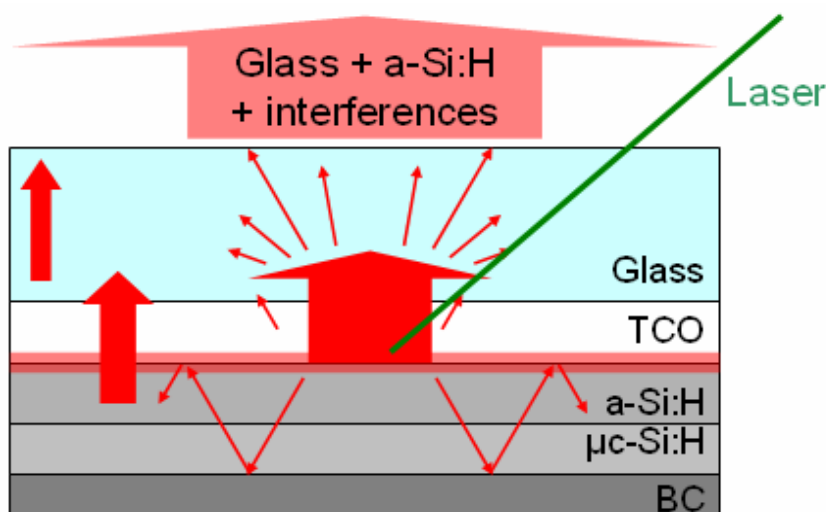


**Figure 5.1.1.4:** Sketch of the luminescence created in the a-Si:H/ $\mu\text{c-Si:H}$  tandem cell: Main luminescence generated in a-Si:H/TCO interface. Detected PL signal is mixture of luminescence from glass and a-Si:H overlapped by interferences.

It was found that the main part of the luminescence is generated in the region of the a-Si:H/TCO interface. That indicates a high defect density there, which is probably assisted by the rough interface structure. Other luminescent regions are the glass substrate and the ‘bulk of the a-Si:H layer’. Next the generated luminescence creates optical interferences in the cell stack, mainly in the  $\mu\text{c-Si:H}$  layer. At the end the detected PL signal is a mixture of material specific luminescence from glass and a-Si:H overlapped by specific interference patterns. The most important result of PL investigations on partially processed cells is that no significant dependence on the kind of excitation could be observed. Typically PL measurements were carried out by excitation of the a-Si:H cell by the incident laser beam. The back contact restricts the ability to excite the  $\mu\text{c-Si:H}$  layer directly. So it could be suggested that the missing PL signal from the  $\mu\text{c-Si:H}$  cell is caused by this specific setup configuration, where more than 90 % of the laser light is absorbed in the a-Si:H cell. To eliminate this effect experiments were performed on cells without back contacts and used excitation from side of

## 5. Other thin-film Si phases – amorphous and microcrystalline Si

the  $\mu\text{-Si:H}$  cell. Even in this conditions only signal from the a-Si:H can be detected. Therefore, the absence of PL signal from the microcrystalline layer must be caused by a very low level of radiative recombination in the bottom cell, which is additionally overlaid by the much more intense PL signal from the top cell. So measurements on single-junction  $\mu\text{-Si:H}$  cells are necessary to get information about this layer.

In summary, there is only PL signal detectable from the amorphous silicon layer, independent on the setup.

### Raman investigations:

Raman measurements were performed on several types of partially processed a-Si:H/ $\mu\text{-Si:H}$  tandem cells. Unfortunately, it turned out that the excitation from the glass side is not possible, because of insufficient Raman intensities. A probable reason for this is the high sensitivity of the Raman signal on the laser focus. This is enormously complicated due to the overlying glass and TCO layers. Therefore, only measurements on samples without back contact and excitation from the backside were possible.

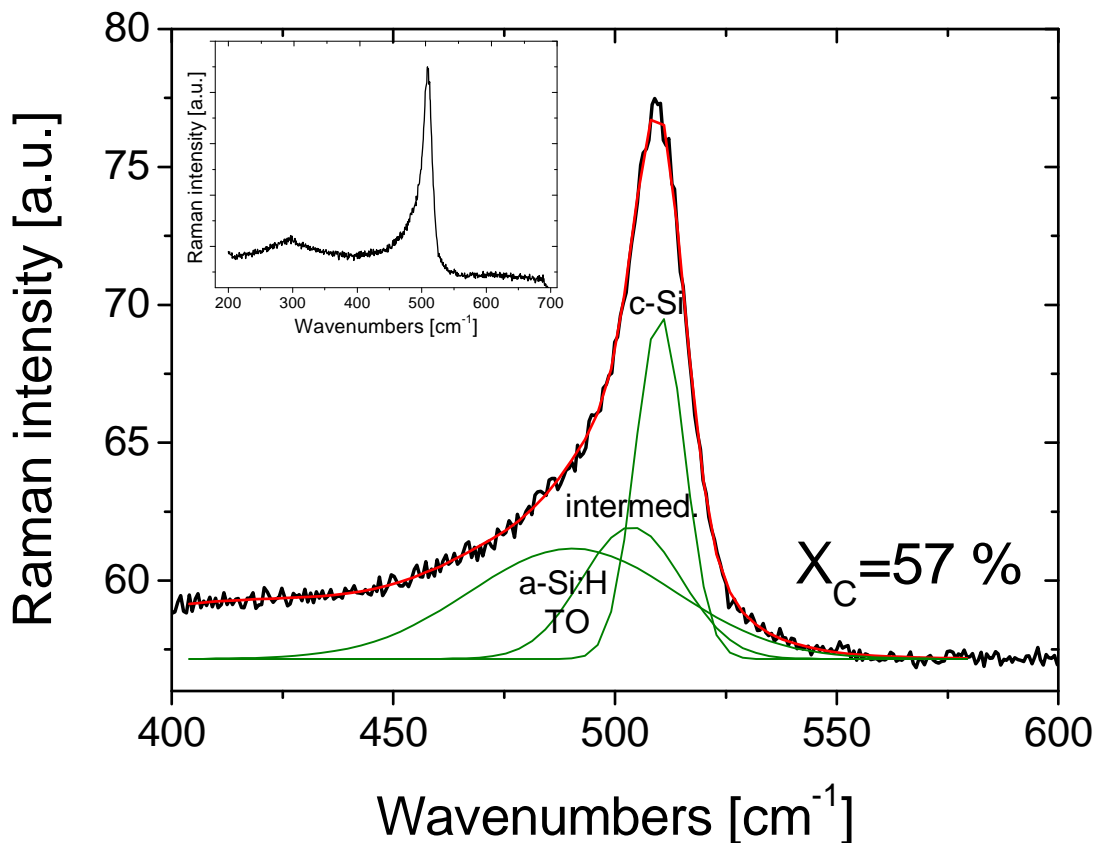


**Figure 5.1.1.5:** Raman spectrum of a-Si:H/ $\mu\text{-Si:H}$  tandem cell without back contact excited from  $\mu\text{-Si:H}$  cell. The inset shows the entire spectrum. The main figure is a magnification of the important part, which is used for the determination of the Raman-crystallinity  $X_C = 57\%$  by deconvolution into the different components (see: sub-chapter 2.2).

## 5. Other thin-film Si phases – amorphous and microcrystalline Si

The Raman spectrum of the completely processed tandem cell excited in this geometry is shown in figure 5.1.1.5. The inset shows the entire spectrum and the main figure shows the important spectral range, which is used for the deconvolution of the crystalline, intermediate and amorphous peaks. They are used to determine the Raman-crystallinity  $X_C$  by equation (2.2.1). The obtained value is 57 %. This is in good agreement with the desired crystallinity of the  $\mu\text{c-Si:H}$  cell. That is a surprising result. The expected value should be lower than that one of the pure  $\mu\text{c-Si:H}$  cell, because of the additional excitation of the a-Si:H cell. Note that PL and Raman are excited by the same laser wavelength. PL measurements do not exhibit any signal from the  $\mu\text{c-Si:H}$ , even under direct excitation of the  $\mu\text{c-Si:H}$  layer (same geometry used for Raman measurements). A part of the explanation might be the shorter focal length of the laser beam ( $\sim 2$  cm) in the Raman setup compared to PL. That makes Raman measurements more sensitive to the surface. However, the entire reason for the missing signal from the a-Si:H layer is still unknown. It might be probable that the Raman intensity of the a-Si:H layer is rather low. In this case it would be extremely complicated to separate both signals. However, Raman and PL are complementary techniques on completely processed a-Si:H/ $\mu\text{c-Si}$ : tandem cells, whereas PL is only sensitive to a-Si:H and Raman to  $\mu\text{c-Si:H}$ .

### 5.1.2 Results and Discussion – EBIC investigations

EBIC investigations of the a-Si:H/ $\mu\text{c-Si:H}$  tandem solar cells were performed by C. Krause. The measurements were carried out on an SEM equipped with a Gatan Digital Micrograph system for quantitative EBIC. The beam energy varies from 10 kV to 30 kV with a beam current less than 100 pA. The used EBIC contacts are the TCO and the back contact of completely processed cells.

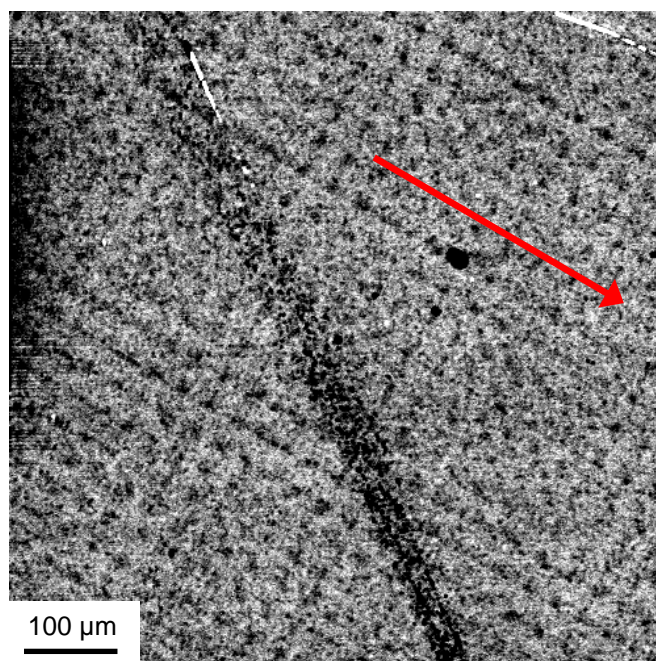


**Figure 5.1.2.1:** Degradation effects in EBIC on tandem cells: Regular point structure activated by the electron-beam, but already latent in cell structure.

## 5. Other thin-film Si phases – amorphous and microcrystalline Si

Standard EBIC investigations of the lateral distribution were not possible because of the high interface roughness, which dominates all EBIC images. It is not possible to minimize this effect by imaging from different material depths, where selected beam energies are related to specific penetration depths. Such investigations were additionally complicated due to the unknown composition of the back contact. An additional problem is the very high sensitivity of the samples to light-induced degeneration. That leads to fast degeneration (few seconds), even at extremely low EBIC currents. That is clearly visible in figure 5.1.2.1, where the degradation causes a regular point structure, with a distance of 30  $\mu\text{m}$ . Thereby the sample was twisted 30° to the scan-direction of the electron-beam to exclude a direct correlation between the point structure and the excitation. It should be emphasized that the structure is independent in the beam energy and therefore present in all layers. All this indicates that the structure is already latent in the cell structure due to a production process and just permanently activated by the electron-beam.

Surprisingly EBIC measurements on the cross-section were possible, which require higher demands to the setup. Of course, parasitic effects, such as electrical charging of the glass, are still present. Contrary to PL, the EBIC signal was collected only from the microcrystalline layer in the tandem cell. This is shown by a comparison of the secondary-electron image (SE) giving topological information, and the EBIC image giving the electrical activity (Fig. 5.1.2.2). One can clearly see that no signal is detectable in the a-Si:H layer.

The missing EBIC signal from a-Si:H cell is probably caused by a very high amount of non-radiative recombination there. That is a very surprising result, because of the investigations performed by PL, where a strong radiative recombination was detected from a-Si:H. A possible explanation of these contrary observations in PL and EBIC could be related to high non-radiative recombination in both layers. It can be assumed that the total recombination rates in a-Si:H are higher than in  $\mu\text{c-Si:H}$ . That is shown by EBIC, which reflects the total recombination activity and is detectable only in the  $\mu\text{c-Si:H}$  cell. However, the probability for radiative transitions in  $\mu\text{c-Si:H}$  is much lower than in the a-Si:H due to indirect transition and the necessary momentum conservation. That is why despite of its lower total recombination it is not observable in PL. In contrary a-Si:H is characterised by high total recombination rate but due to the partially relaxation of the momentum conservation rule it appears in PL.

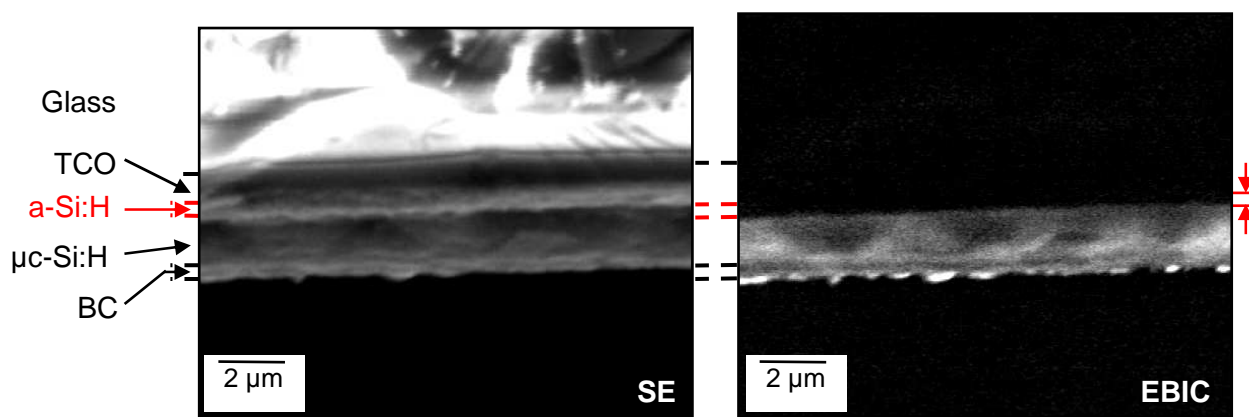


**Figure 5.1.2.2:** Cross-section EBIC on tandem cells: Comparison of secondary-electron image (SE), giving topological information, and EBIC showing electrical activity. No EBIC signal from a-Si:H layer can be detected.

## 5. Other thin-film Si phases – amorphous and microcrystalline Si

However, EBIC and PL are complementary techniques, too. To our knowledge, these are the first cross-section EBIC measurements on thin-film tandem cells. Based on the above investigations, it was demonstrated that the a-Si:H/ $\mu$ c-Si:H tandem cell is a good example for high challenging characterisation of complex thin-film samples. By adapting two, techniques (PL and EBIC), which are well-established and originally designed for investigations of bulk material, preliminary investigations on such layer systems were carried and allowed to identify other features of these analysis techniques, which need to be further modified to overcome these challenges.

### **Summary and conclusion:**

Measurements along the cross-section of solar cell stacks depict high requirements to sample preparation as well as investigation/characterisation techniques. If these requirements are not fulfilled, then interpretation of the measured data becomes very complicated. Another requirement is exact knowledge of the cell structure and the analysis technique. But even if this is fulfilled a combination of several techniques is absolutely necessary to investigate the entire cell structure, especially at very complex cell stacks. Combined techniques can reveal complementary sensitivities, such as between PL/EBIC and PL/Raman. The reasons for the missing a-Si:H signal in PL and EBIC are different sensitivities to radiative and total recombination. That is contrary to bulk mc-Si, where PL and EBIC show a (slightly limited) image of the distribution of excess carrier lifetime.

In general, complex sample structures require investigations of partially processed samples under different setup conditions, e.g. excitation from different sides of the sample.

PL is highly influenced by interference patterns at complex cell stacks consisting of layers with thicknesses between a few hundred nanometers and a few millimeters. Estimations of the layer thickness from the interference patterns reveal thicknesses of around 2  $\mu$ m. This indicates sensitivity to the sum of both Si cells.

Measurements on a-Si:H/ $\mu$ c-Si:H tandem cells exhibit PL features, which are comparable to those on a-Si:H of bulk thickness. That indicates that thin a-Si:H layer behave like bulk a-Si:H. Nevertheless, thin-film effects thin-film effects must be considered carefully. The strong impact of interface recombination is restricted by the fact that excess carriers can move freely from the bottom to the top cell. Therefore, the effective layer thickness is not limited to 340 nm (top cell) but rather to around two micrometers (top cell + bottom cell). However, the impact of non-radiative recombination is still detectable. One example is the spatial specific distribution of luminescence. That is clearly proved by comparative measurements on samples with and without back contact. Here the interface recombination does affect the spectral and spatial distribution luminescence.

The applicability of Raman is limited by the requirement of direct excitation of the Si layers. Therefore, it can only be used on cells without back contact. Raman exhibits only signal from the  $\mu$ c-Si:H layer, without detectable signal from the a-Si:H layer. That includes the Raman-crystallinity of the  $\mu$ c-Si:H layer on the entire tandem cell. It is probable that this is partially caused by low Raman signal from a-Si:H.

## 5. Other thin-film Si phases – amorphous and microcrystalline Si

All these facts emphasize the need of measurements on partially processed cells, such as single  $\mu\text{c-Si:H}$  layers.

### 5.2 Characterization of 500 nm $\mu\text{c-Si:H}$ on glass substrate

One of the characteristic features of the a-Si:H/ $\mu\text{c-Si:H}$  tandem cells on glass substrate is the absence of PL signal from the  $\mu\text{c-Si:H}$  bottom cell. A very low PL intensity was assumed as reason. This signal would be overlaid by much more intense signals from a-Si:H. Therefore, PL investigations of the  $\mu\text{c-Si}$  layer were not possible on completely processed tandem cells. However, the  $\mu\text{c-Si:H}$  cell is one of the basic component of the tandem cell and information about its PL features are still necessary. That becomes clear by considering the enormous impact of the exact deposition conditions on the optical properties of  $\mu\text{c-Si:H}$ , especially in PL. This impact is extremely high and was previously reported in many publications. PL investigations on  $\mu\text{c-Si:H}$  films show very different spectra. Small deviations of the deposition conditions (gas flow, temperature, etc.) as well as substrate properties (thickness, type of glass, etc.) are extremely critical. Thereby two ‘typical’ PL peaks appear more or less frequently at low temperatures ( $\sim 10$  K). The first one is related to the tail states of the remaining a-Si:H and localized between 1.2 eV and 1.3 eV. The second one is localized between 0.9 eV and 1 eV and is related to tail states of the  $\mu\text{c-Si:H}$  [Bha1983, Mer2006, Yue2000]. However, almost every PL feature is possible in a wide spectral range, including that no one of the ‘typical’ peaks appear [Bou1983, Das2003]. Therefore PL measurements on single-junction  $\mu\text{c-Si:H}$  cells are necessary to characterize the deposition process of the solar cells. But, more important are information about the physical aspects of microcrystalline silicon – third key-question of this work. One example for such aspects is the transformation process from amorphous to microcrystalline silicon.

#### Investigated samples:

The investigated samples are a series of 500 nm thick intrinsic  $\mu\text{c-Si:H}$  layers on the same glass substrate, which was used for the tandem cells. They differ in their crystallinity. This is controlled by variations of the silane concentration. Unfortunately, it was not possible to deposit  $\mu\text{c-Si:H}$  directly onto the glass substrate or on TCO. A 10 nm to 20 nm thick  $\text{Si}_x\text{N}_y$  layer was placed between glass and silicon to prevent spalling due to mechanical instabilities. This layer supports the wetting and adhesion of the  $\mu\text{c-Si:H}$  layer. Despite of this effort the stabilized thickness of the layer is limited to 500 nm instead of 1.6  $\mu\text{m}$  as in the tandem cells. A sketch of the investigated samples is shown in figure 5.2.1. The crystallinity of the  $\mu\text{c-Si:H}$  layers were controlled by different silane to hydrogen concentration. No back contact is deposited on the samples to reduce the impact of interface recombination, which is higher on Si/metal interfaces than on Si/air.



## 5. Other thin-film Si phases – amorphous and microcrystalline Si

Glass substrate ~ 3.2 mm
Si <sub>x</sub> N <sub>y</sub> 10 nm - 20 nm
μc-Si:H ~ 500 nm

**Figure 5.2.1:** Sketch of the μc-Si:H samples: The μc-Si:H layers differ in their crystallinity.

### 5.2.1 Results and Discussion – Raman investigations

Standard Raman measurements were performed to determine the Raman-crystallinity  $X_C$  of the μc-Si:H films (see: sub-chapter 2.2). Figure 5.2.1.1 shows Raman spectra of samples with various crystallinities. These samples were selected for further PL investigations. The analyses of the Raman spectra by equation (2.2.1) obtain Raman-crystallinities of 8 %, 23 %, 37 %, 54 % and 77 %.

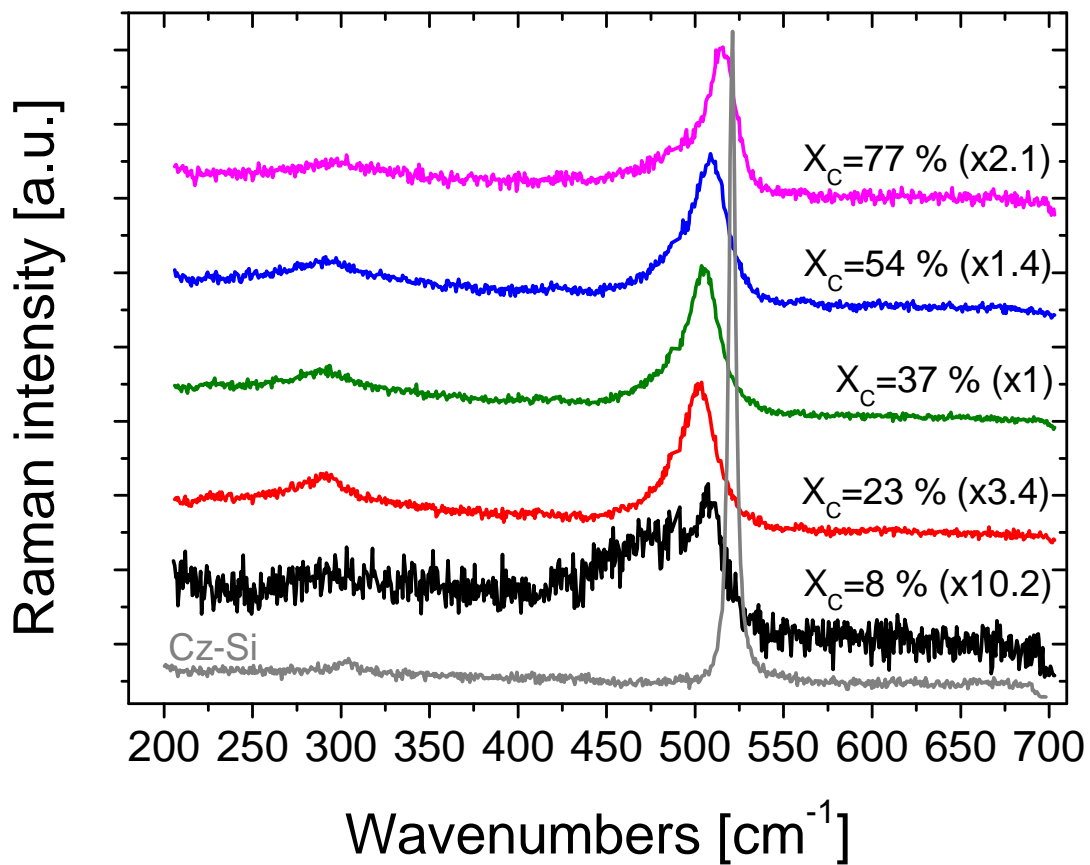


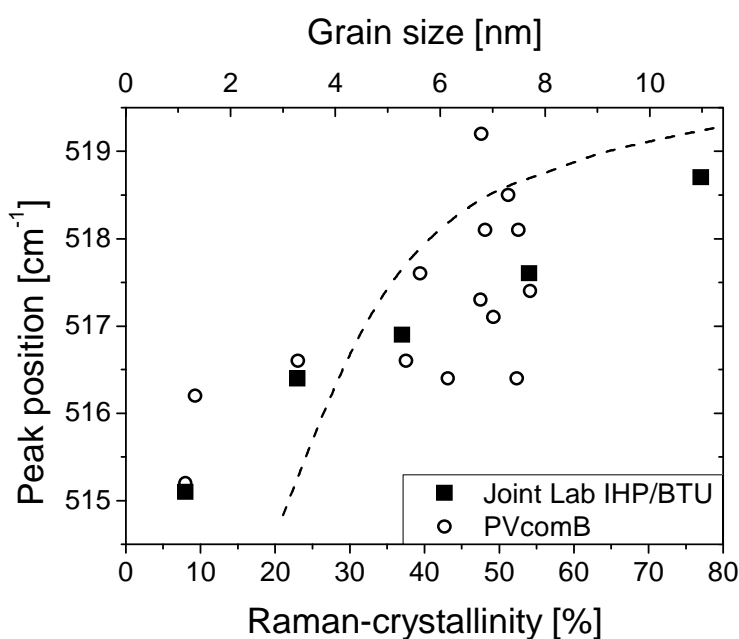
**Figure 5.2.1.1:** Raman spectra of several μc-Si:H samples with different Raman-crystallinity  $X_C$ . The spectra are multiplied by the factors in brackets for better spectral comparability. The grey spectrum shows Cz-Si as reference.

## 5. Other thin-film Si phases – amorphous and microcrystalline Si

Note that the sample with 54 % represents the crystallinity, which is desired for tandem cells. A massive drop of the open-circuit voltage  $V_{OC}$  [Kle2003] characterizes microcrystalline cells with higher crystallinity. So the sample with 77 % Raman-crystallinity is added to this series for a complete overview of the entire transformation process from amorphous to microcrystalline silicon.

The spectra exhibit strong deviations in the Raman intensities. Therefore, they are multiplied by several factors to give a better comparability of the spectral features. These factors are written in brackets. One can see that the intensity of samples with very low crystallinity is rather low compared to the sample with 54 % Raman-crystallinity. That proves the assumption from sub-chapter 5.1, where a low intensity from a-Si:H was assumed as one reason for the missing Raman signal on the tandem cells. The increasing crystallinity is characterized by increasing intensities of the Raman modes associated with the crystalline and intermediate components at around  $520\text{ cm}^{-1}$  and  $505\text{ cm}^{-1}$ , respectively. The amorphous modes decrease (e.g. the transversal optical mode (TO) around  $480\text{ cm}^{-1}$  (see: sub-chapter 2.2)), simultaneously. Two other spectral features also denote the increasing crystallinity. The first one is a shift of the crystalline and intermediate peaks to the spectral position of pure c-Si, which is represented by the grey spectrum of Cz-Si. The other feature is the shrinking of the corresponding peak widths (FWHM).

These two parameters are related to the average size of the forming nanocrystalline grains (nc-Si:H). It is very important to note that Raman spectroscopy cannot distinguish between isolated grains in a-Si:H matrix and grains agglomerated to  $\mu\text{c-Si:H}$  columnar structures. This must be considered during interpretation of the obtained data. Figure 5.2.1.2 shows an attempt to extract the grain sizes on this basis, depending on the crystallinity. The dashed lines are fits extracted from Ossadnik et al. [Oss1999]. It is important to emphasize that the lines show the correlation between the grain size and the peak position/peak width without the additional impact of internal stress. Such assumption is unrealistic in the investigated  $\mu\text{c-Si:H}$  films. Therefore, the strong deviations from the dashed lines are not surprisingly. To reduce this effect the data measured at Joint Lab IHP/BTU are combined with data measured at the PVcomB. Despite of this the plots exhibit enormous stress-induced variations.



(a)

## 5. Other thin-film Si phases – amorphous and microcrystalline Si

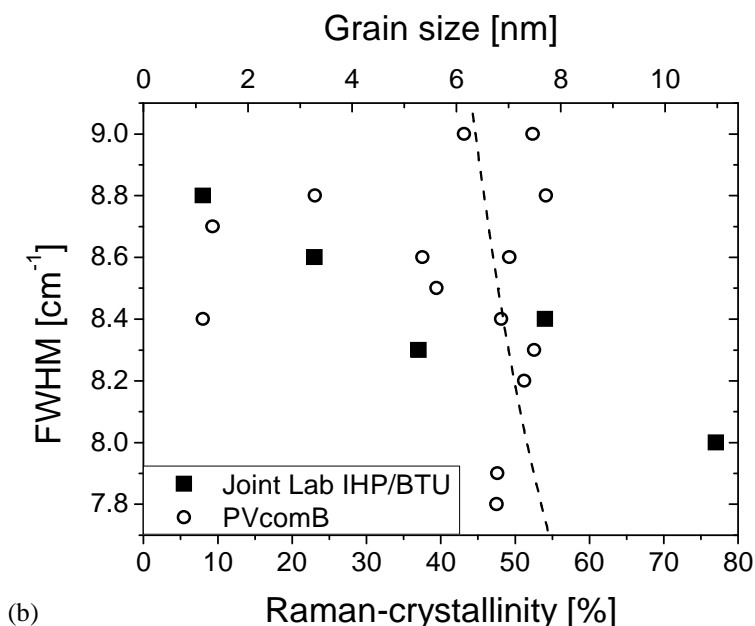


**Figure 5.2.1.2:** Raman peak position (a) and peak width (FWHM) (b) as function of the Raman-crystallinity: It is possible to estimate average grain sizes by using dashed lines from [Oss1999]. Strong deviations between data points and dashed line are mainly induced by stress. Plots include Raman data from PVcomB and Joint Lab IHP/BTU for higher statistical validity.

However, a tendency of increasing peak position and decreasing peak width is clearly visible. An average grain size of around 1 nm can be extracted at low Raman-crystallinities. It can be assumed that these grains are isolated in the a-Si:H matrix. In contrast to this, the grain size at high crystallinities of around 11 nm is an average of isolated grains and those agglomerated to microcrystalline columns.

### 5.2.2 Results and Discussion – PL investigations

The five samples measured at Joint Lab IHP/BTU were selected for PL investigations. They exhibit the widest range of Raman-crystallinity. The corresponding Raman spectra are shown in figure 5.2.1.1. PL measurements on these samples are highly influenced by typical thin-film effects, such as strong PL signal from glass substrate. Therefore it is necessary to deconvolute the measured spectra to obtain specific information about  $\mu\text{c-Si:H}$ . All presented results are corrected in this way.

The general dependences of PL of all samples are shown in figure 5.2.2.1. Thereby the dependence of the integrated PL intensity on the Raman-crystallinity is of special interest. It decreases of more than two orders of magnitude in an exponentially (Fig. 5.2.2.1(a)). The error bars represent spatial deviations of the PL intensity (see: Fig. 5.2.2.5 and text). This enormous decrease can partially explained by the reduction of PL intensity in the crystalline/intermediate parts of the samples. These regions behave like indirect semiconductors and are therefore characterized by a very low probability for radiative

## 5. Other thin-film Si phases – amorphous and microcrystalline Si

recombination. That can be also described as a much lower amount of trapped carriers in localized tail states.

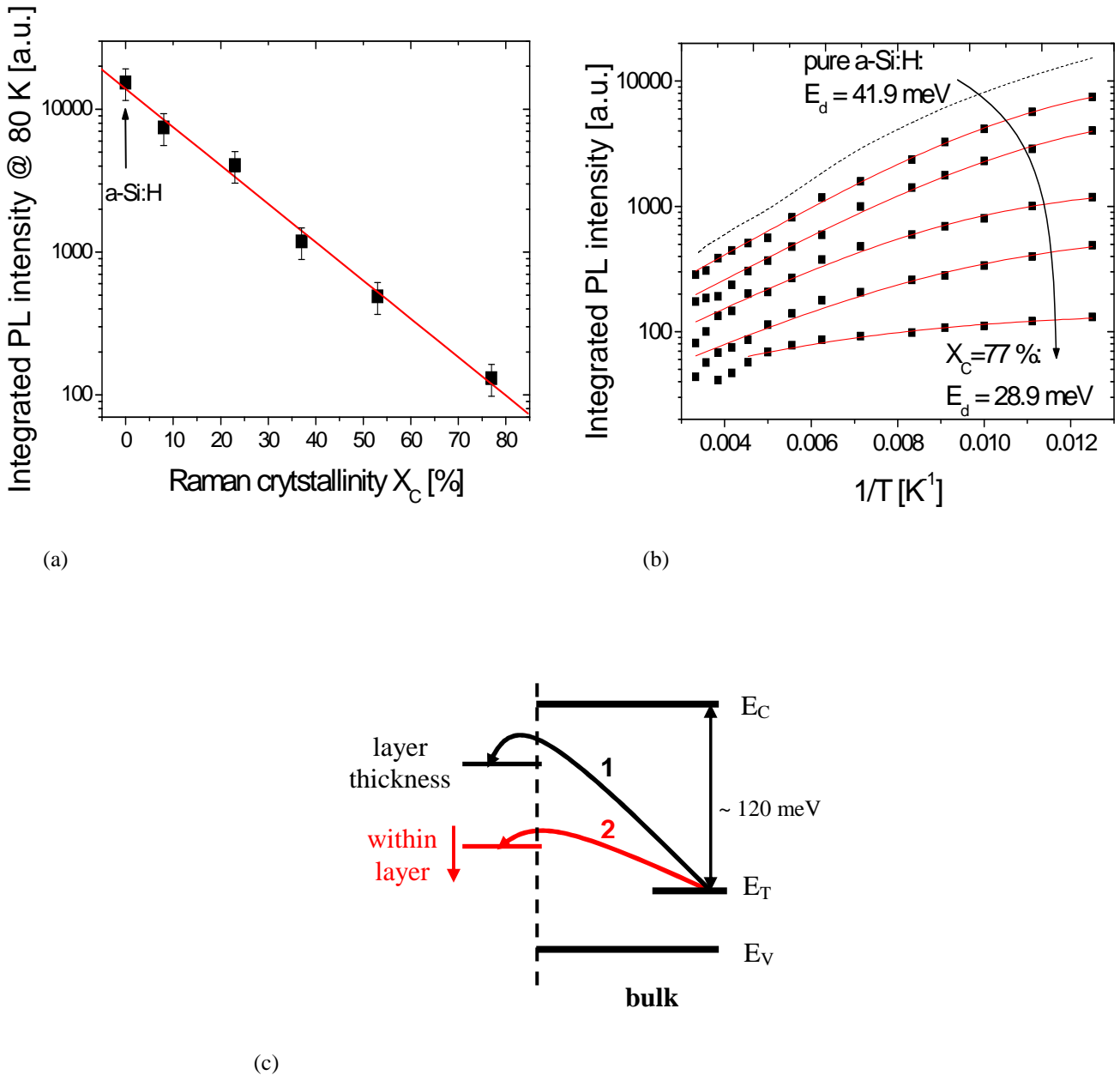


**Figure 5.2.2.1:** Dependences of integrated PL intensity on Raman-crystallinity  $X_C$  and temperature: The PL intensity at 80 K decreases drastically with increasing  $X_C$  (a). The deactivation energies  $E_d$  are mainly dominated by interface recombination at the sample surfaces and interfaces within the samples (e.g. a-Si:H/ $\mu$ c-Si:H interfaces) (b). Sketch of the non-radiative surface/interface recombination paths in thin  $\mu$ c-Si:H films (c).

Nevertheless, a simple estimation indicates that this approach is not sufficient to explain the entire decrease of the PL intensity. Let us assume that the crystalline components of  $\mu$ c-Si:H layers do not exhibit any luminescence. In that case the integrated PL intensity of the sample with 8 % Raman-crystallinity should be 8 % less than the intensity of the pure a-Si:H. But the actually measured PL intensity decreases of more than 50 %. The reason for this unexpected decrease of the PL intensity is the additional presence of non-radiative recombination

## 5. Other thin-film Si phases – amorphous and microcrystalline Si

processes at interfaces. That includes recombination at grain boundaries formed during the transformation process from amorphous to microcrystalline silicon. Such recombination processes can appear at two different kinds of grain boundaries. It can be grains in the a-Si:H matrix as well as  $\mu\text{c-Si:H}/\mu\text{c-Si:H}$  grain boundaries. That is proved by analysis of the temperature dependence in figure 5.2.2.1(b).

The extracted deactivation energies  $E_d$  decrease from meV for pure a-Si:H to 28.9 meV for the 77 %  $\mu\text{c-Si:H}$  sample. At first, it must be emphasized that these energies are significantly too low for amorphous as well as for microcrystalline silicon. For example the expected value for bulk a-Si:H should be around 120 meV [Eng1977]. Even for the a-Si:H/ $\mu\text{c-Si:H}$  tandem cells a deactivation energy of 107 meV was extracted.

These energies represent the barrier height between two bulk states (e.g. defect level  $E_T$  and conduction band  $E_C$ ). So the measured strong deviation is partially caused due to the lower thickness of the layer. That makes interface recombination more important as in bulk materials or tandem cells, where excess carriers can move freely through bottom and top cell ( $\sim 2 \mu\text{m}$ ). Therefore, the deactivation energy  $E_d$  on the thin  $\mu\text{c-Si:H}$  layers does not represent a barrier between different material specific bulk states, but rather between a bulk state and interface states. That is illustrated by transition 1 in figure 5.2.2.1(c). So the different sample geometry/layer thickness leads to a constant deviation from energies obtained on bulk material. But the further decrease of the energies with increasing crystallinity can not be explained by that because of the constant sample thickness. Therefore, differences within the layers must be considered. The increase of crystallinity manifests in an increasing amount of interface states, additionally to those caused by the layer thickness itself. These interface states are related to interfaces within the layers and become created during the crystallization of silicon. At low Raman-crystallinities the interfaces are formed by isolated nc-Si:H grains in the amorphous matrix. But at higher values the interfaces at the  $\mu\text{c-Si:H}/\mu\text{c-Si:H}$  grain boundaries become more and more important. These sample-intern interface recombination processes are illustrated by transition 2 in figure 5.2.2.1(c).

PL spectra of the five samples investigated by Raman are shown in figure 5.2.2.2 at 80 K. A spectrum of pure a-Si:H is added for getting a complete overview of the transformation process from amorphous to microcrystalline silicon. The spectra are normalized to focus on the spectral distribution of the luminescence, because of the very strong differences in PL intensity (see: Fig. 5.2.2.1(a)). The spectra are fitted by several Gaussian peaks and labeled accordingly to the corresponding radiative transitions.

Pure amorphous silicon shows a well-known spectrum consisting of two very broad peaks. The main one at 1.2 eV is related to transitions between the tail states and the smaller one belongs to transitions between defects and tail states. This peak is localized at about 0.9 eV. In case of  $\mu\text{c-Si:H}$  four peaks can be distinguished, which exhibit specific dependences on the crystallinity. The use of inverted commas in the peak labels was originally adopted from Merdzhanova et al. [Mer2006]. But during the analysis it turned out that the use of the inverted commas helps to separate transitions originating in the same phase of silicon but characterized by different physical properties. The first peak in  $\mu\text{c-Si:H}$  is localized between 1.3 eV and 1.4 eV. It is probably related to nanocrystalline silicon and therefore labeled ‘nc’-Si:H. It was previously detected by Yue et al. [Yue1999], but not associated with nanocrystals. The other three peaks can be compared with literature data quite well. The ‘a’-Si:H peak (1.2 eV - 1.1 eV) represents the transitions between tail states in the remaining a-

## 5. Other thin-film Si phases – amorphous and microcrystalline Si

Si:H matrix. The ‘ $\mu\text{c}$ ’-Si:H peak between 0.9 and 1 eV and the ‘defect’  $\mu\text{c}$ -Si:H peak at around 0.8 eV are related to tail states of  $\mu\text{c}$ -Si:H and radiative defects in  $\mu\text{c}$ -Si:H, respectively. The attribution of these three PL peaks to specific transitions in silicon is quite reliable. Similar results can be found in various papers, despite of the fact that the exact PL features are characterized by differences caused by different deposition conditions. An example for this is the defect-related peak. Its spectral position varies between 0.7 eV [Mer2006] and more than 0.8 eV [Yue1999]. The important point is that these peaks appear quite frequently and so they can be considered as reproducible. This is in contrast to the ‘nc’-Si:H peak between 1.3 eV and 1.4 eV, which was only observed by Yue et al. [Yue1999, Yue2000] at low crystallinities. Therefore, its attribution to silicon nanocrystals is more hypothetically.

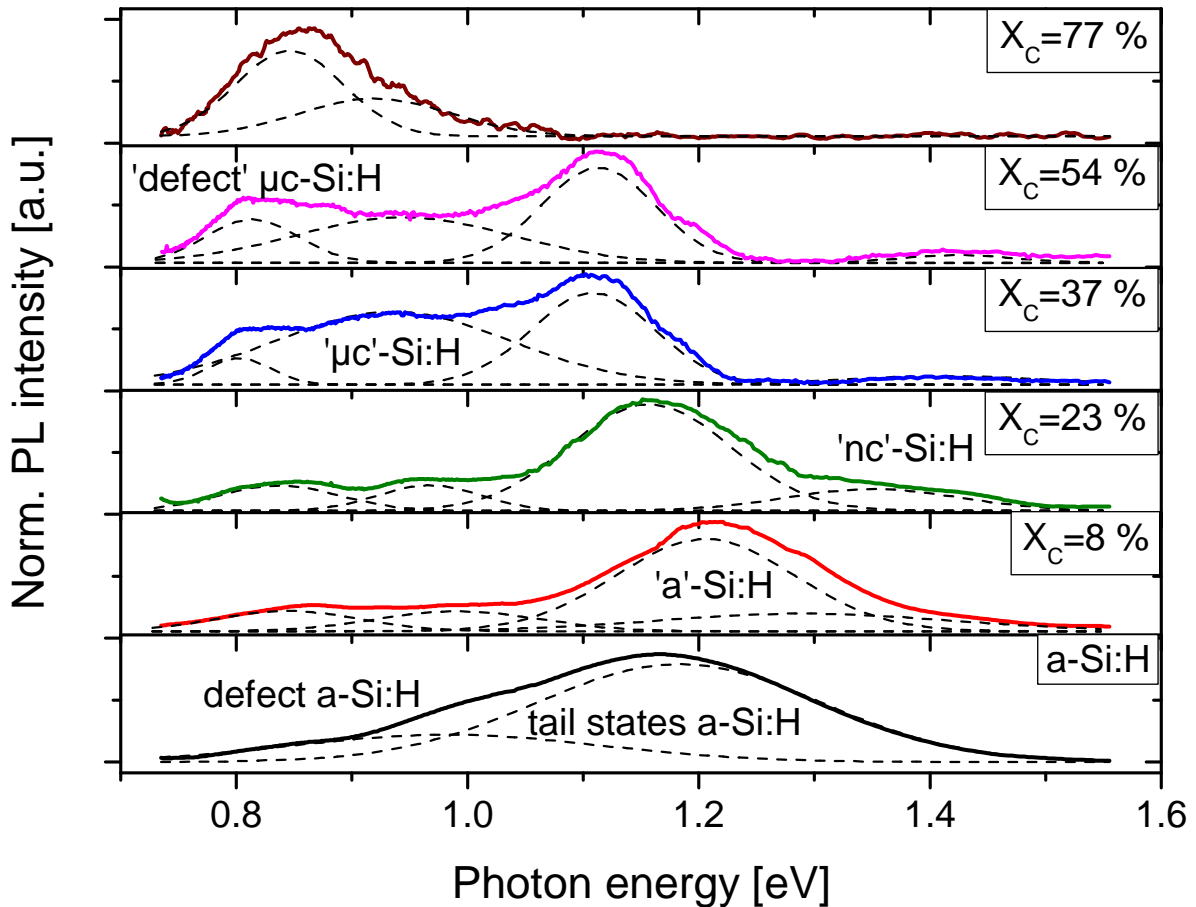


**Figure 5.2.2.2:** Normalized PL spectra of  $\mu\text{c}$ -Si:H samples with different Raman-crystallinity  $X_C$  and pure a-Si:H at 80 K. Spectra are fitted by Gaussian peaks (dashed lines). The peak labels are explained in the text.

The most important parameters of all four peaks are the peak energy  $E_{peak}$  and the intensity relative to the intensity of the entire spectrum  $I_{rel}$ . These values are summarized in table 5.2.2.1 depending on the Raman-crystallinity  $X_C$ . Note that the indicated spectral accuracy is lower than in chapter 4 due to the higher impact of glass luminescence during the deconvolution of the spectra. But on the investigated  $\mu\text{c}$ -Si:H layers it is not critical because of the high broadness of the peaks instead of the quite sharp peaks in case of oxide precipitates.

## 5. Other thin-film Si phases – amorphous and microcrystalline Si

The ‘nc’-Si peak shifts to higher energies of around 1.4 eV with increasing crystallinity. Its relative intensity decreases to a very low level and vanishes completely at very high crystallinities. This behavior can be explained considering the fact that the isolated nc-Si:H grains within the amorphous matrix start to agglomerate to microcrystalline columnar structures with increasing crystallinity.

$X_C$	$E_{\text{peak}}$ ‘nc’-Si:H [eV]	$E_{\text{peak}}$ ‘a’-Si:H [eV]	$E_{\text{peak}}$ ‘ $\mu\text{c}$ ’-Si:H [eV]	$E_{\text{peak}}$ ‘defect’ $\mu\text{c}$ - Si:H [eV]	$I_{\text{rel.}}$ ‘nc’- Si:H [%]	$I_{\text{rel.}}$ ‘a’- Si:H [%]	$I_{\text{rel.}}$ ‘ $\mu\text{c}$ ’- Si:H [%]	$I_{\text{rel.}}$ ‘defect’ $\mu\text{c}$ -Si:H [%]
8 %	1.29	1.21	0.99	0.85	18.5	61.3	8.8	11.3
23 %	1.35	1.16	0.97	0.84	14.9	63.2	10.3	11.6
37 %	1.41	1.12	0.94	0.81	1.8	42.3	47.2	8.6
54 %	1.43	1.11	0.93	0.82	4.3	40.5	40.3	14.8
77 %	/	/	0.93	0.83	/	/	49.8	50.2

**Table 5.2.2.1:** Comparison of parameters (peak energy  $E_{\text{peak}}$ , relative intensity  $I_{\text{rel.}}$ ) of the  $\mu\text{c}$ -Si:H PL peaks in figure 5.2.2.2 depending on the Raman-crystallinity  $X_C$ .

Nanocrystalline silicon is characterized by a strong correlation between the PL peak energy and the grain size. The smaller the grain size  $g$  the bluer is the maximum of the PL signals  $E_{\text{PL}}^{\text{corr}}$ . This relation is given by following equation [Led2000]:

$$E_{\text{PL}}^{\text{corr}} = E_0 + \frac{3.73}{g^{1.39}} + \frac{0.881}{g} - 0.245 \quad (5.2.2.1)$$

where  $E_0$  is the bandgap of c-Si 1.17 eV. The detected peak energy can be understood based on quantum-confinement, i.e. by the radiative recombination of electron–hole pairs confined in silicon nanocrystals. In this model, the emitted luminescence energy of the electron–hole pair is shifted towards higher energies [Led2002]. The broadness of the ‘nc’-Si:H peak denotes a wide distribution of grain sizes. According to equation (5.2.2.1), it is possible to determine the grain size from the PL spectra in figure 5.2.2.2. The estimated grain sizes vary from around 13 nm (1.1 eV) to around 4.5 nm (1.55 eV). The upper grain size is quite high but still in the order of previous results obtained by TEM measurements [Hou1998, Luy1997]. The lower one is highly limited by the sensitivity of the Ge-detector at higher photon energies. According to this, the presence of smaller grains is very probable, especially when the grains start to form in amorphous silicon. The peak width (FWHM) of the ‘nc’-Si:H peak represents the size-distribution of grains. It decreases from 0.27 eV (8 %  $\mu\text{c}$ -Si:H) to 0.13 eV (54 %  $\mu\text{c}$ -Si:H). That is illustrated in figure 5.2.2.3, where the broadness of the ‘nc’-Si:H peak and equation (5.2.2.1) are combined to determine the size-distribution of single nanocrystalline grains within the amorphous matrix. There one can see that bigger grains seem to vanish anywhere with increasing crystallinity and only smaller grains remain. This might indicate that bigger grains are favored for agglomeration to  $\mu\text{c}$ -Si:H columns (see: sub-chapter 1.3). After agglomeration, these grains emit luminescence in the spectral range associated with the ‘ $\mu\text{c}$ ’-Si:H peak instead of the ‘nc’-Si:H one. It is probable that these grains can growth slightly further. The remaining ‘nc’-Si:H signal comes from smaller grains and is

## 5. Other thin-film Si phases – amorphous and microcrystalline Si

therefore shifted to higher energies and the peak width decreases. This suggestion is in agreement with the expected transformation process from a-Si:H to  $\mu\text{c-Si:H}$ , where nc-Si:H is an intermediate phase. The 'nc'-Si:H peak vanishes completely at high crystallinities just like the 'a'-Si peak. It is probable that newly formed nc-Si:H grains become directly embedded into the  $\mu\text{c-Si:H}$  columns at very high crystallinities.

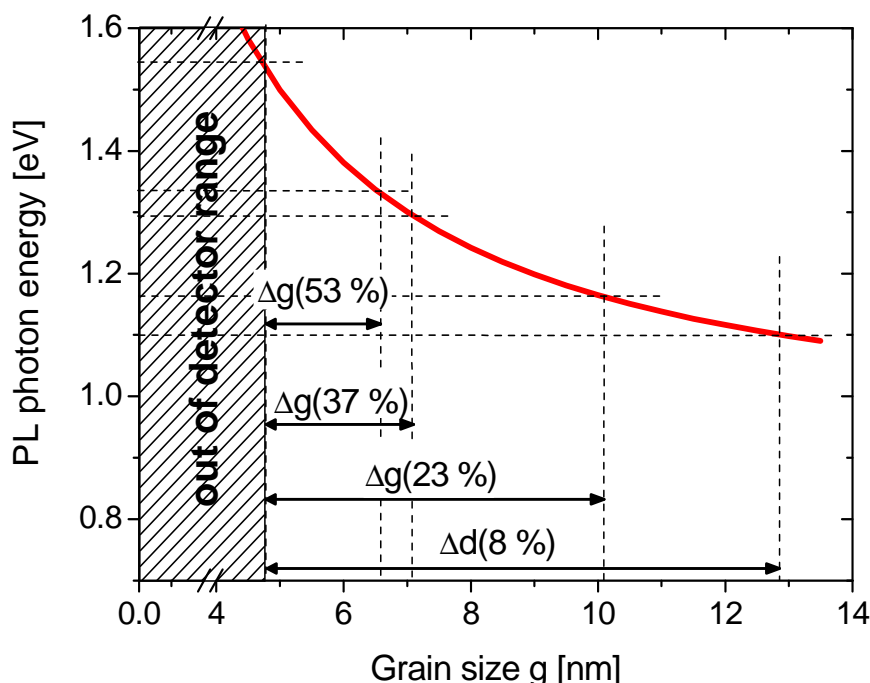


**Figure 5.2.2.3:** Distribution of nanocrystalline grain sizes in  $\mu\text{c-Si:H}$  samples: The grain sizes are extracted from the broad 'nc'-Si:H peak in the PL spectra (Fig. 5.2.2.2) and calculated according to equation (5.2.2.1) [Led2000]. Bigger grains become preferably embedded in  $\mu\text{c-Si:H}$  columns. Attention: The detection of lower grain sizes is highly limited due to the sensitivity of the Ge-detector at higher photon energies.

In the next step the grain size estimated from PL are compared with those obtained from Raman measurements. One big difference between both techniques is obviously clear. At low crystallinities (8 %) Raman exhibits an average grain size of around 1 nm. In contrast to this PL yields a broad distribution up to 13 nm. Note that PL is limited by the sensitivity of the detector. Therefore, smaller grains can not be detected and so bigger grains are overestimated. Raman seems to be more reliable in this range of crystallinity. At high crystallinities, Raman yields an average grain size of around 11 nm, which is higher than the values obtained by PL of 5 to 7 nm. In this case it must be considered that PL is only sensitive to single nc-Si:H grains in the a-Si:H matrix, because of the selected PL peak. But Raman gives an average size of both types of grains, single ones and agglomerated ones. Therefore the value extracted from Raman spectra must be a little bit higher because of the further growth in the  $\mu\text{c-Si:H}$  columns. In summary, it is not possible to obtain reliable data of the grain size by only one technique. But combined data from Raman and PL can give a quite good estimation of the actual grain size. At low crystallinities, PL overestimates the grain size and Raman should be preferred. At high crystallinities PL and Raman give reliable values for the grain size, considering the neighborhood of the grains – other grains or a-Si:H.

The 'a'-Si peak shifts to lower energies and the relative intensity decreases with increasing crystallinity. It vanishes completely at crystallinities of about 77 %. Thereby the peak width



## 5. Other thin-film Si phases – amorphous and microcrystalline Si

(FWHM) decreases significantly from 0.29 eV (pure a-Si:H) to 0.11 eV (54 %  $\mu\text{c}$ -Si:H). It is not totally clear if these changes are related to any interactions of a-Si:H with the forming silicon grains or if it denote a real change of optical/structural properties of amorphous silicon. Assuming a real change, the decrease of peak width could be explained as a process of ordering within the amorphous silicon. So the lower peak width would represent a reduced deviations of bond length and bonding angles in an ordered 'a'-Si:H phase, compared to ordinary a-Si:H. Such approach of explanation is used to describe the reduced width of the ' $\mu\text{c}$ '-Si:H peak compared to pure a-Si:H and it seems plausible to use it here, too. However, the use of the inverted commas is absolutely necessary to separate the 'a'-Si:H phase from the ordinary form of a-Si:H.

Simultaneously with the decreasing intensities of the 'a'-Si:H and 'nc'-Si:H peaks an increase of the microcrystalline ones (' $\mu\text{c}$ '-Si:H and 'defect'  $\mu\text{c}$ -Si:H) can be observed. The redshift of the ' $\mu\text{c}$ '-Si:H peak (from 1 eV to 0.93 eV) is similar to the redshift of 'a'-Si:H. This could indicate an ordering process, too. Thereby the grains would growth closer to each other forming a higher density of Si grains within the  $\mu\text{c}$ -Si:H columns. The relative intensity of the defect-related peak keeps quite constant up to the range of crystallinity, which is desired for solar cells. But at higher Raman-crystallinity it increases drastically. It even exceeds the contribution of transitions between the tai-states of ' $\mu\text{c}$ '-Si:H peak. That agrees with observations made by Yue et al. [Yue1999]. They detected a strong increase of low energy luminescence (defects in  $\mu\text{c}$ -Si:H) at high crystallinity and associated this with the strong impact of the grain boundaries.

A careful view on table 5.2.2.1 shows that the peak energies of the 'a'-Si:H and the ' $\mu\text{c}$ '-Si:H peaks changes quite drastically at lower crystallinities. But at higher values the energies start to stabilize at a certain level. That might indicate the point of transformation from the ordered 'a'-Si:H phase to a more or less disordered ' $\mu\text{c}$ '-Si:H and further ordering within the  $\mu\text{c}$ -Si:H columns, respectively.

The temperature behavior of the PL spectra is shown in figure 5.2.2.4 on the example of the  $\mu\text{c}$ -Si:H sample with 37 % Raman-crystallinity. There are no significant differences between the temperature behaviors of the other samples. All four peaks show a shift to lower energies with increasing temperature, which is caused by bandgap shrinking. It should be emphasized that the 'nc'-Si:H peak is only detectable at temperature below 200 K. Note that the redshift of the 'a'-Si:H peak is more intense ( $\sim 30$  meV) than the shifts of the peaks, which are related to microcrystalline Si (' $\mu\text{c}$ '-Si:H and 'defect'  $\mu\text{c}$ -Si:H) ( $\sim 10$  meV). The difference in the magnitude of the temperature shift can be explained by the attribution of the peaks to different phases of silicon. The 'a'-Si:H peak behaves similar to ordinary amorphous Si, whose temperature shift is more intense than that one of crystalline silicon. This was calculated by Luckas et al. [Luc2011] using the Varshni formula. Investigations of the 'nc'-Si:H peak shift are limited by the lower temperature range but it is roughly comparable with reference data [Fuj1998]. The same magnitude of the temperature shifts of the 'defect'  $\mu\text{c}$ -Si:H and the ' $\mu\text{c}$ '-Si:H peak supports the assumption that the radiative defects are related to microcrystalline and not to amorphous Si.

## 5. Other thin-film Si phases – amorphous and microcrystalline Si

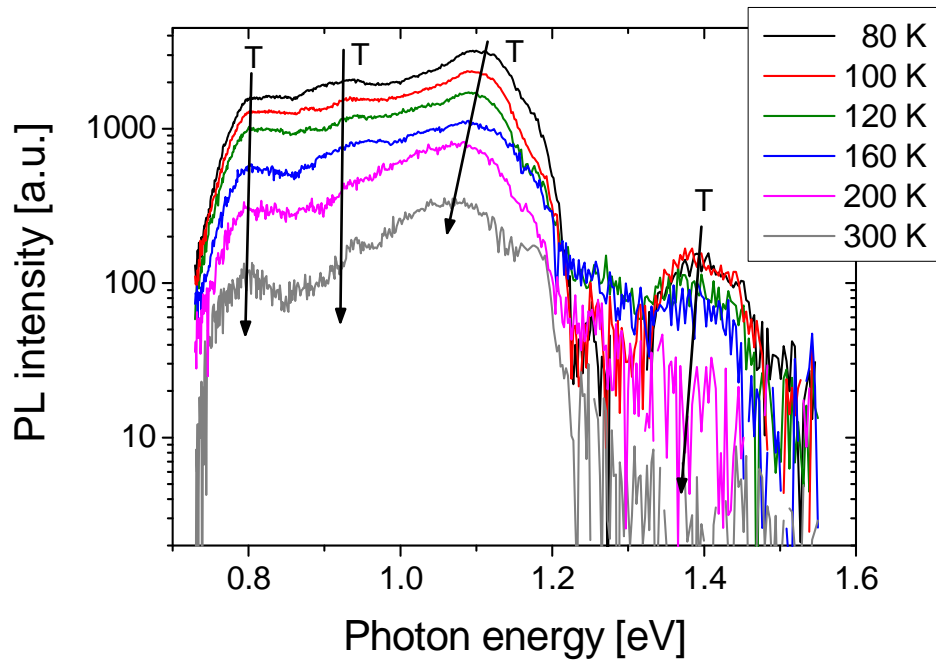


**Figure 5.2.2.4:** Temperature dependence of the PL spectra on the example of the  $\mu\text{c-Si:H}$  with 37 % Raman-crystallinity. Arrows mark the temperature shift.

PL Mapping performed investigations of the spatial distribution of luminescence. Two examples are given in figure 5.2.2.5. There one can see PL Maps of the samples with 23 % and 77 % Raman-crystallinity. The maps exhibit extended (mostly dark) and finer (mostly bright) regions within a quite homogeneous background of the  $\mu\text{c-Si:H}$  signal.

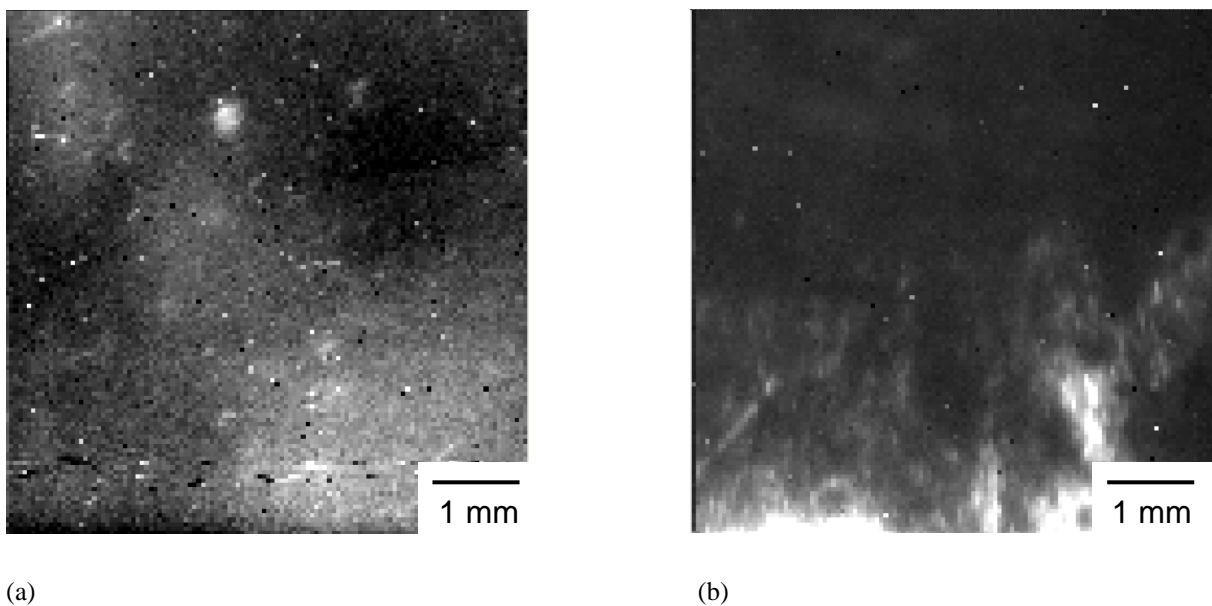


**Figure 5.2.2.5:** PL Maps on  $\mu\text{c-Si:H}$  samples with 23 % (a) and 77 % Raman-crystallinity (b). The inhomogeneous regions are in the order of 25 % and independent on the selected spectral range. Statistical analyses of all PL Maps do not show any correlation between Raman-crystallinity and spatial deviations of the PL signal.

## 5. Other thin-film Si phases – amorphous and microcrystalline Si

It is important that these regions are independent on the spectral position of luminescence. That means that the regions do not illustrate different Si phases, such as a-Si:H or  $\mu\text{c-Si:H}$ . Statistical analysis of all maps (standard deviation etc.) do not obtain any correlation between the crystallinity and the inhomogeneity of the samples. The only difference of the PL Maps is the absolute PL intensity. The relative deviations within the maps are in the same range of around 25 % and were considered in the correlation between PL intensity and Raman-crystallinity (see: Fig. 5.2.2.1(a)). That could indicate instabilities in the deposition process of the  $\mu\text{c-Si:H}$  layers. Similar results were observed for a-Si:H (see: sub-chapter 5.1).

### Summary and conclusion:

Rather low Raman intensities in amorphous/slightly crystallized  $\mu\text{c-Si:H}$  films compared to those of higher crystalline samples were assumed in the last chapter. This is confirmed in this chapter. Actually the intensity of the 8 %  $\mu\text{c-Si:H}$  is about 10 times less than that one of crystallinities desired for tandem cells. Therefore no influence of the a-Si:H top cell can be detected on Raman measurements on the a-Si:H/ $\mu\text{c-Si:H}$  tandem cell. So the calculated Raman-crystallinity on a-Si:H/ $\mu\text{c-Si:H}$  tandem cells can be considered as equal to the crystallinity of the  $\mu\text{c-Si:H}$  bottom cell alone.

It was possible to detect  $\mu\text{c-Si:H}$  signal by PL on specially prepared samples without the dominating a-Si:H layer. However, the effort in measurement time and time for data analysis increases significantly, despite of the more simple cell structure. This is partially caused by the much lower PL intensity of  $\mu\text{c-Si:H}$  layers, which is overlapped by luminescence from the glass substrate. Indeed the glass signal is up to 20 times higher than that one from  $\mu\text{c-Si:H}$ , depending on the crystallinity. The low intensity becomes additionally reduced by the limited layer thickness of 500 nm, instead of 1.6  $\mu\text{m}$  as in the tandem cells. The differences in the deposition conditions between the tandem cell and the specially prepared  $\mu\text{c-Si:H}$  layers may also affect the spectral features of the PL signal. That includes the different layer thickness as well as the different substrate. Therefore, it must be emphasized that the obtained results cannot be directly transferred to the tandem cells.

The most important thin-film effect is the enhanced recombination at interfaces. On samples with layer thicknesses less than the generation depth of excess carriers it does not only affect the spatial distribution of PL (see: chapter 3), but also other PL features, such as the deactivation energy. The deactivation energy allows the determination of barrier heights between a trap level and the conduction band, in bulk samples. But on 500 nm  $\mu\text{c-Si:H}$  the deactivation energy represents the barrier between a bulk trap state and states in the bandgap created by interfaces. However, that was a helpful indication for the increasing formation of interfaces within the sample (e.g. nc-Si:H grains in a-Si:H matrix). That is a good example for successful adjustment and transfer of methods from bulk Si to thin-film ones – the second key-question of this work.

The importance of exact determination of the impact of thin-film effects is emphasized again. If this is successful, combined techniques, such as PL and Raman, offer a possibility to understand the transformation process from amorphous to microcrystalline silicon. For instance, it was possible to get quite reliable data of the sizes of the grains by careful interpretation of the data from both Raman and PL. A model was obtained, which describes a

## 5. Other thin-film Si phases – amorphous and microcrystalline Si

stepwise transformation from a-Si:H to  $\mu\text{c-Si:H}$ . Table 5.2.2.2 shows every ‘transformation step’ with the corresponding PL- and Raman features.

	Transformation from a-Si:H to $\mu\text{c-Si:H}$	PL-/Raman features
1.)	Transformation starts with a process of ordering in a-Si:H. The typical deviations of bond length and bond angle become reduced to a more ordered structure. The resulting ‘a’-Si:H differs from ordinary a-Si:H.	<ul style="list-style-type: none"> <li>– Redshift and decreasing peak width of ‘a’-Si:H PL peak</li> <li>– Very dominant signal from a-Si in Raman</li> </ul>
2.)	Single isolated nc-Si:H grains start to crystallize in ‘a’-Si matrix. The grains exhibit a wide range of grain sizes up to 13 nm. The average size is around 1 nm. The term ‘nc’-Si:H denotes different distributions of grain size.	<ul style="list-style-type: none"> <li>– Appearance of very broad ‘nc’-Si:H peak in PL</li> <li>– Decrease of low deactivation energies with increasing crystallinity in PL</li> <li>– Crystalline signal in Raman</li> <li>– Grain sizes extracted from PL and Raman</li> </ul>
3.)	Bigger nc-Si:H grains starts to agglomerate to columnar $\mu\text{c-Si:H}$ structures. Smaller nc-Si:H grains remain in ‘a’-Si:H matrix.	<ul style="list-style-type: none"> <li>– Presence of ‘<math>\mu\text{c}</math>’-Si:H PL peak</li> <li>– Blueshift and decreasing width of ‘nc’-Si:H PL peak</li> </ul>
4.)	Smaller nc-Si:H grains become directly embedded in $\mu\text{c-Si:H}$ columns at higher crystallinities. Microcrystalline columns become dominant and regions of isolated nc-Si:H grains in a-Si:H matrix vanish.	<ul style="list-style-type: none"> <li>– Disappearance of ‘a’-Si:H and ‘nc’-Si:H PL peaks</li> </ul>
5.)	Grains in ‘ $\mu\text{c}$ ’-Si:H columns order to a higher density. The term ‘ $\mu\text{c}$ ’-Si:H denotes different states of ordering in microcrystalline Si.	<ul style="list-style-type: none"> <li>– Redshift of ‘<math>\mu\text{c}</math>’-Si:H peak in PL</li> </ul>
6.)	Defects related to grain boundaries of $\mu\text{c-Si:H}$ become dominant at high values of crystallinity and lead to a decrease of radiative recombination by tail states in $\mu\text{c-Si:H}$ . Final average grain sizes are in the order of about 11 nm. This value agrees quite well with most TEM measurements on several $\mu\text{c-Si:H}$ films.	<ul style="list-style-type: none"> <li>– Stronger increase of ‘defect’ <math>\mu\text{c-Si:H}</math> PL peak at high crystallinity</li> <li>– Decrease of ‘<math>\mu\text{c}</math>’-Si:H PL peak at high crystallinity</li> <li>– Grain size extracted from Raman and PL</li> </ul>
	The entire process is quite disordered and chaotic, which results in an enormous stress level in the Si films.	<ul style="list-style-type: none"> <li>– Strong stress-induced variations of peak position and peak width in Raman</li> </ul>

**Table 5.2.2.2:** Model of the stepwise transformation from amorphous to microcrystalline silicon and the corresponding PL-/Raman features.

## 5. Other thin-film Si phases – amorphous and microcrystalline Si

Of course, this model is not totally new and based on knowledge obtained from other techniques (e.g.: known typical nc-Si:H grain size from TEM [Luy1997, Hou1998]) partially. Nevertheless, it is still remarkable to observe such complex process just by PL and Raman. A special care should be on the presence of the phases of ordered amorphous ('a'-Si:H) and nanocrystalline silicon ('nc'-Si:H). These phases are not investigated in detail, up to now.

The obtained stepwise model will be compared with established models from literature [Mat2004, Kas2006] now. There the growth of  $\mu\text{c-Si:H}$  can be separated into two parts. The first one deals with processes on atomic scale, which forms a basis for the further crystallization/growth processes of  $\mu\text{c-Si:H}$ . Three models have been established to describe this: surface-diffusion model, etching model, and chemical-annealing model. All of these models deal with a huge impact of hydrogen atoms. They interact with the amorphous Si and lead to the formation of structure that is more ordered and/or stronger Si-Si bonds. This can be associated with the suggested presence of an order 'a'-Si:H phase. The second part describes the crystallization process itself. The model suggest crystalline islands in the a-Si:H matrix and the second part of the  $\mu\text{c-Si:H}$  growth process begins, where the islands act as nucleus for further crystallization. These islands can be associated with the detected nc-Si:H grains. Smaller agglomerations of a few grains are possible, too. Following the model, an enforced coalescence of the islands takes place due to the enhanced surface diffusion of silane, which results in a smooth surface. This gives rise to an internal stress, mainly in the a-Si:H layer. Here the model allows to localize the origin of the detected stress in  $\mu\text{c-Si:H}$  layers. After that, the surface roughness is enhanced due to an orientation-dependent crystal growth rate. This allows the final formation of the characteristic  $\mu\text{c-Si:H}$  columnar structures with their very high amount of twin boundaries by epitaxial-like crystal growth. In summary, the suggested model obtained by PL and Raman agrees quite well with models from literature. But it is obviously clear that PL and Raman do not offer a view into process on the atomic scale.

## **Part II**

### **6. Electroluminescence investigations on bulk mc-Si solar cells**

Additional to investigations on thin-film samples investigations were also performed on completely processed bulk mc-Si solar cells. Thereby the focus was on electroluminescence (EL). Sub-chapter 6.1 deals with the specific temperature behavior of BB luminescence in case of excitation by electrical current. It differs significantly from the behaviors in PL. Sub-chapter 6.2 deals with a special type of defect, which does not emit any luminescence in case of PL. But under excitation by reversed bias it emits specific luminescence features (ReBEL), which are related to breakdown sites.

These measurements might be helpful for further investigations on thin-film samples dealing with the same topics. Therefore, the basic processes must be understood at first on bulk material without the parasitic effects on thin films. That would give the needed reference for the desired knowledge transfer.

#### **6.1 Anomalous temperature behavior of band-to-band (BB) EL in mc-Si solar cells**

Although, the silicon luminescence is a phenomenon, extensively studied for many years, some details specific for the luminescence of solar cell material still attract the scientific interest. For instance, the impact of several excitation conditions on the temperature behavior of the band-to-band (BB) luminescence intensity. In case of PL, the temperature behaviors are associated to different material qualities. The normal temperature behavior, a decrease of PL intensity with increasing temperature, is associated to high-grade silicon. The anomalous temperature behavior, an increasing PL intensity with increasing temperature, is associated to low grade Si. This was already discussed in sub-chapter 1.2.1. This chapter is about the temperature behavior of the BB intensity during EL measurements. It turned out that there is a big impact of the excitation conditions. Therefore, it is not so easy to compare results obtained by PL with those obtained by EL. The samples were studied with the PL Imaging setup and the setup for temperature dependent EL measurements, which are described in sub-chapter 2.1. The obtained results were published in *Physical Status Solidi (c)* [Klo2011].

### Investigated samples:

A solar cell fabricated on a standard block cast p-type silicon wafer with thickness of 180  $\mu\text{m}$  was subjected to electroluminescence imaging of BB radiative transition at room temperature by an InGaAs camera. Areas exhibiting quite uniform but either weak or strong luminescence were selected (Fig. 6.1.1). Samples of size approximately  $2 \times 2 \text{ mm}^2$ , containing contacting fingers on top were prepared from those areas. Temperature dependent measurements were performed on 3 samples, which were extracted from areas showing high luminescence (P1 and P3) and area of low luminescence (P2).

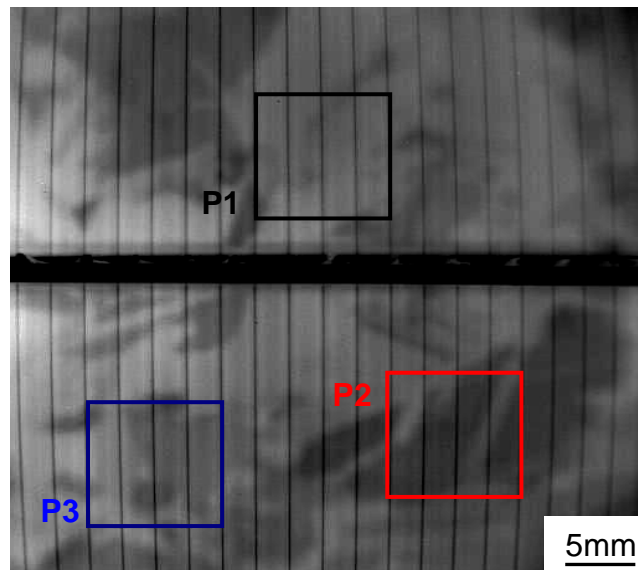


**Figure 6.1.1:** EL imaging of a mc-Si solar cell at 300 K. Marked regions are selected for temperature dependence measurements, because of different EL intensities.

### Results:

EL spectra of the samples were recorded at different temperatures and different forward currents. The integral of the BB peak in the spectra was taken as a measure of the radiative recombination rate. A linear dependence of the EL intensity on the exciting current was found for all measuring temperatures on all samples. This guarantees operating in the low-injection regime and prevents any parasitic effects of high injection. Figure 6.1.2 illustrates the typical dependence on the exciting current at 300K. The experimental points were fitted with straight lines to emphasize the linear dependence on the excitation. The slopes of the lines for the samples extracted from the 'good areas' (P1 and P3) of the wafer are higher than that from the low quality one. At very low current densities (below  $10 \text{ mA/cm}^2$ ) no luminescence was detectable. It might be possible that this is because of the radiative fraction of the space charge recombination at low voltages [Mic1969].

## 6. Electroluminescence investigations on bulk mc-Si solar cells

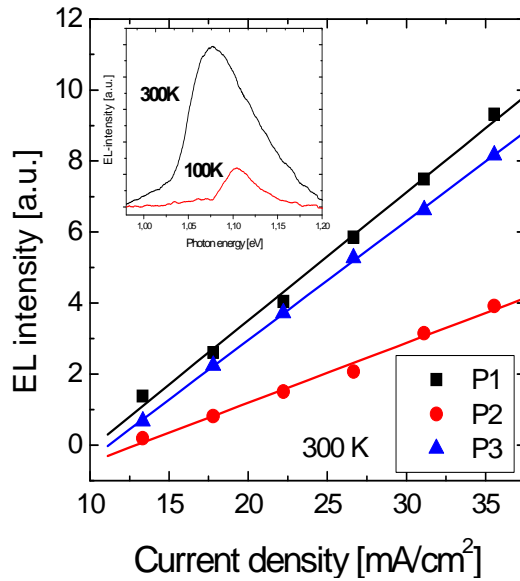


**Figure 6.1.2:** Integral BB intensity as function of current density at 300 K. The solid lines are linear fits to the experimental data. Inset shows EL spectra at P1 (300 K and 100 K).

The inset shows the temperature dependence of EL spectra at P1 (current density 31.1 mA/cm<sup>2</sup>). Surprisingly, in case of EL all samples show an anomalous behavior, namely, increasing signal with temperature (Fig. 6.1.3), but the rate of this increase differs. Comparative measurements of the temperature behavior in case of PL were excited by a ns-Laser (Continuum Precision 2 equipped with Panther EX OPO) with a pulse length of around 5 ns and a repetition rate of 30 Hz. The wavelength was fixed at 800 nm and the averaged laser power was 30 mW. The opposite behavior is detected in case of PL experiments. This is shown in figure 6.1.3 on the example of sample P1.

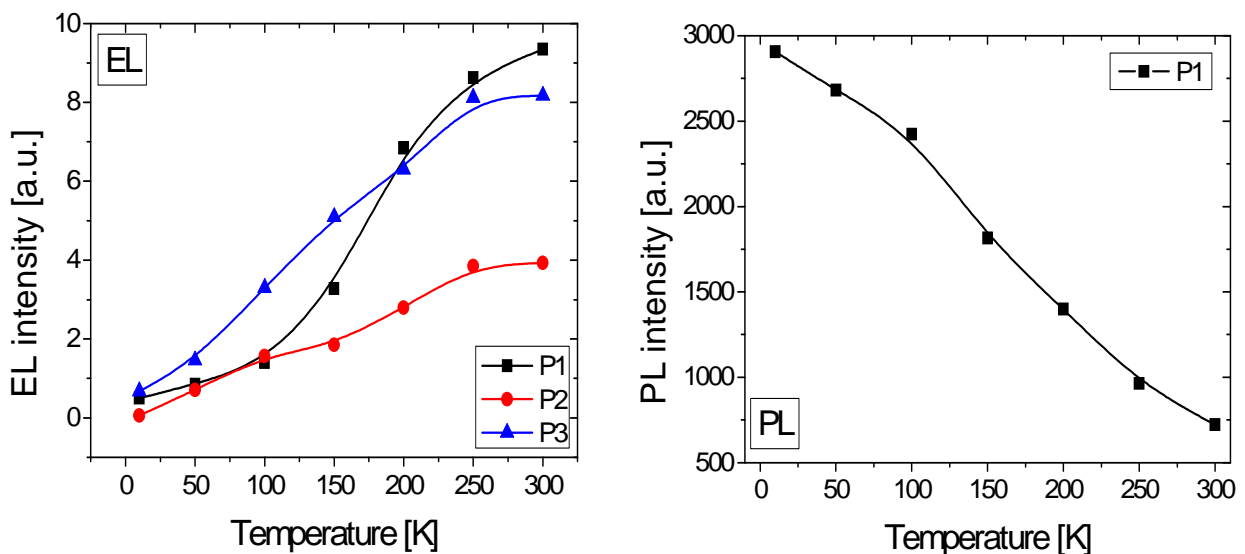


**Figure 6.1.3:** Contrary temperature behaviors of the BB intensity in case of EL and PL.



## 6. Electroluminescence investigations on bulk mc-Si solar cells

Peak position and peak width (FWHM) of the BB peak follow the expected behavior for silicon in the entire temperature range. Figure 6.1.4 shows the temperature dependences of those two parameters (symbols) together with the expected dependences (dashed curves). The expected position of the peak was calculated by Varshni's formula [Var1967] accounting for the temperature induced band gap shrinkage and for the energy of the optical phonons mediating the transition. The temperature-induced peak broadening was estimated assuming a transition between two 3-dimensional energy bands and according three-dimensional changes linearly with temperature. The temperature dependence of the peak width is proportional to the value for direct semiconductors  $1.8 k$ , where  $k$  is the Boltzmann constant [Schu1997]. Deviations of peak position and peak width from the calculated curves are observed below 100 K, which we attribute to a difference between the temperature recorded on the sensor of the refrigerator and the real temperature on the sample. Due to the electric current flow, heat is dissipated and the sample temperature becomes higher locally. A temperature gradient across the wafer is formed. The heat dissipation, the voltage drop, and the maximal excess carrier concentration occur at the junction. Thus, the luminescence is mainly generated there, too. That is why the peak position and width reflect the local temperature near the junction. However, the luminescence is determined by the concentration of minority carriers, which diffuse to the backside. The temperature of the bulk of the wafer is close to that of the sensor. The elevated sample temperature can explain why no carrier freezing is observed down to 10 K. The main part of the temperature dependence of the broadening is given by  $1.8 kT$ . The dependence of other broadening mechanisms (phonon [Bebb1972], impurities and strain [Bal1983]) is weak and visible in the offset of the peak width and in the deviation at very low temperatures (Figure 6.1.4(b)).

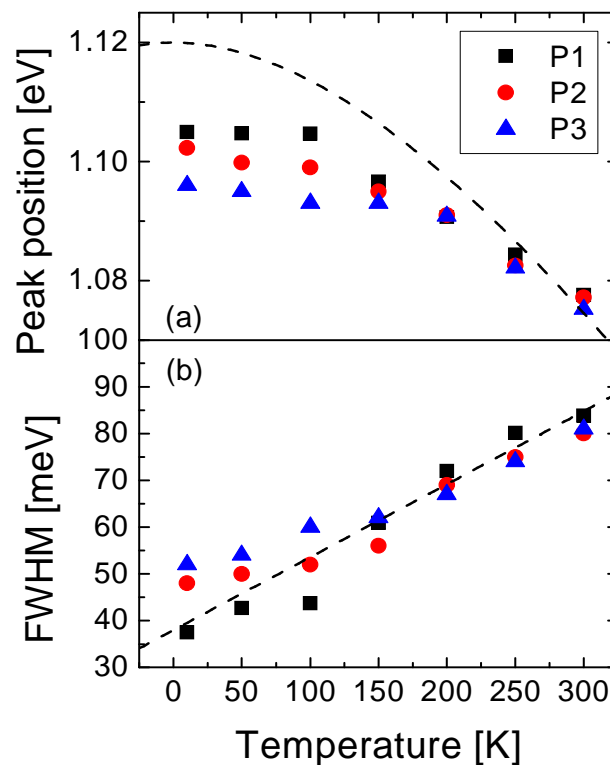


**Figure 6.1.4:** Temperature dependence of the BB peak parameters peak position (a) and peak width (FWHM) (b). The dashed lines note the expected behavior.

## Discussion:

The increase of the luminescence with temperature is in contrast to earlier reports where on pure silicon a decrease has been observed. However, such behavior has been detected previously [Arg2007a]. It has been suggested that the anomaly is a result of a temperature induced change of Shockley-Read-Hall (SRH) lifetime. Indeed, assuming that the lifetime of minority carriers is determined by recombination through a shallow level in the band gap of silicon one can show that the recombination rate increases and the lifetime decreases with increasing temperature [Arg2007b]. At fixed excitation rate, the radiative recombination is affected by the non-radiative pathways, lowering the total amount of the minority carriers. Such competitive non-radiative transitions could be mediated by shallow levels in the band gap. According the SRH statistics, those levels should be more effective recombination centers at high temperatures and much less at low temperatures, where they are predominantly occupied by one carrier type.

Such model could explain the anomalous temperature behavior quite well, but raises questions about the physical origin of the shallow recombination levels. Here a model is presented that explains the anomalous temperature behavior in case of electroluminescence as a result of amplified surface recombination. In case of quite thin samples (e.g. solar cells) the effective minority carrier lifetime increases on increasing temperature due to the restricted carrier diffusion and the surface recombination. The most probable explanation in case of samples with high surface recombination is illustrated in figure 6.1.5 and based on limited diffusion length due to the sample thickness.

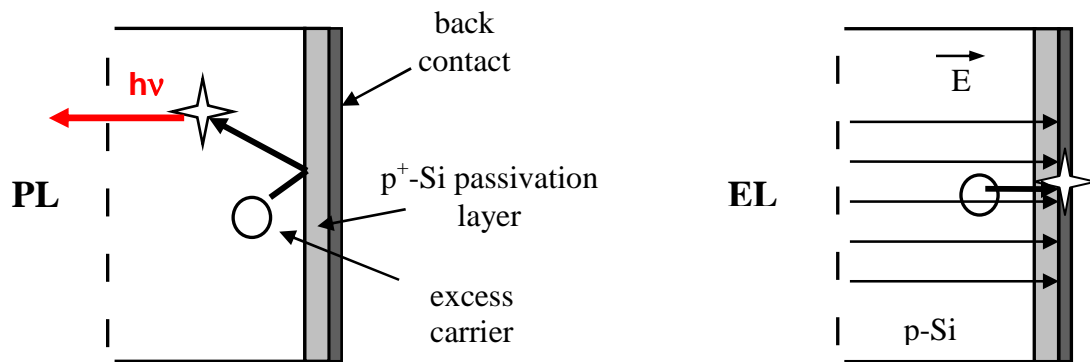


**Figure 6.1.5:** Sketch of the model to explain contrary temperature behaviors in PL and EL. Applied electric field attracts carriers to back contact overcoming the p/p<sup>+</sup>-barrier in case of EL.

In a solar cell, the back side is usually passivated and equipped with a p/p<sup>+</sup> doping junction (back surface field (BSF)) for preventing the minority carriers of reaching the surface. So the carriers become reflected at the BSF and have a higher probability for radiative recombination. Those techniques successfully reduce the recombination on the backside and lead to a higher charge collection at the junction at the cell front in case of PL. This is illustrated in the figure by a radiative recombination process. However, in case of EL, the minority carriers in the vicinity of the back side could not be reflected back into the bulk, because of the electric field, which drives them to the back surface. In such case the effective

## 6. Electroluminescence investigations on bulk mc-Si solar cells

surface recombination is amplified and the carrier diffusion length becomes limited by the cell thickness. This leads to non-radiative surface recombination.

To estimate the temperature behavior of BB luminescence it was assumed that the luminescence is proportional to the excess carrier in the bulk. Indeed, such relation has been observed in a broad range of excitations (Fig. 6.1.2). In case of constant generation  $G$  (constant forward current) the excess carrier concentration  $\Delta n$  is proportional to the minority carrier lifetime  $\tau$ ,  $\Delta n \sim G\tau$ . The temperature behavior of the BB intensity is determined by two factors. One is the radiative recombination coefficient  $B(T)$  and the other is the minority carrier lifetime  $\tau(T)$ . The BB intensity reflects mainly the temperature dependence of the lifetime in these experiments. It was assumed that the effective lifetime  $\tau_{eff}$  is determined by a recombination in the bulk  $\tau_{bulk}$  and recombination at the surface  $\tau_{surface}$ :

$$\frac{1}{\tau_{eff}} = \frac{1}{\tau_{bulk}} + \frac{1}{\tau_{surface}} \quad (6.1.1)$$

The surface recombination limits the diffusion length of the carriers to the cell thickness  $d$ . Thus the surface lifetime could be estimated by  $\tau_{surface} = L^2/D(T)$ , where  $L$  denotes the lifetime, which is equal to the cell thickness  $d$  and  $D(T)$  is the temperature dependent diffusivity of the minority carriers. A more sophisticated analysis of the minority carrier diffusion in such structure leads to [Spr1994]:

$$\tau_{surface} = \frac{4d^2}{\pi^2 D(T)} \quad (6.1.2)$$

The diffusivity decreases with temperature  $D(T) \sim T^{-1.5}$  [Bat2003], leading to increasing surface recombination lifetime. It was calculated that the effective lifetime, assuming a room temperature diffusivity of the minority electrons  $D(300\text{ K})=30\text{ cm}^2/\text{s}$  [Spr1994] and a deep level mediating the bulk recombination. The SRH model was used for calculating the bulk lifetime. The results are given in figure 6.1.6.

It is seen that the calculated dependence of the effective lifetime reproduces quite well the temperature dependence of the BB luminescence. The surface recombination determines the effective lifetime at low temperatures, whether at high temperature the bulk one dominates.

The temperature dependence of the surface and the bulk recombination rates can explain the temperature behaviors in literature [Bre2008]. Depending on the position of the energy level mediating the bulk recombination and depending on the concentration of those recombination centers one can obtain differently steep profiles for the temperature behavior of the effective lifetime.

The temperature dependence of BB EL provides a means to compare the non-radiative recombination rate in the bulk with that at the surface without relying on absolute photometric analysis. This could be used in photovoltaics to compare the silicon material quality of the wafers. The steeper the BB EL temperature dependence the lower the non-radiative recombination rate in the bulk.

## 6. Electroluminescence investigations on bulk mc-Si solar cells

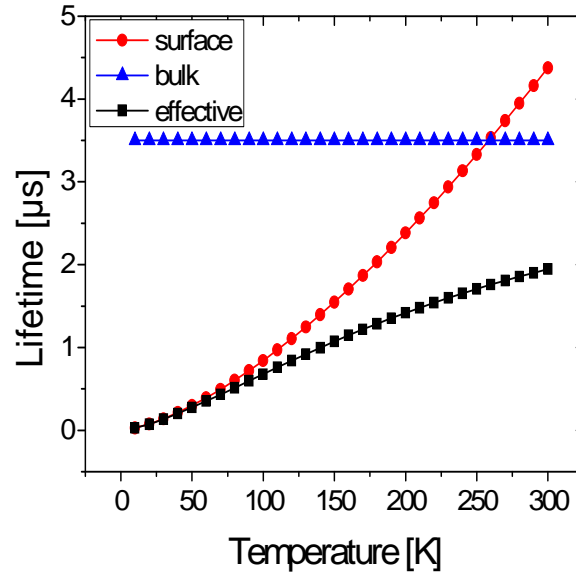


**Figure 6.1.6:** Temperature dependence of effective lifetime, surface recombination lifetime and bulk recombination lifetime.

### Summary and conclusions:

The temperature behavior of BB luminescence was investigated on samples of a completely processed mc-Si solar cell. Anomalous temperature behavior is observed at defect rich as well on defect free parts of a p-type silicon solar cell. The results were analyzed in view of surface and SRH recombination.

The major contribution is due to recombination at the back surface. It is a strong sink for minority carriers, which are driven there by the applied field in case of electroluminescence experiment. This amplifies the surface recombination, which is limiting the diffusion length of the minority carriers to the wafer thickness. An additional reason could be recombination through shallow levels in the band gap [Arg2007a].

The most important result of this investigation is the fact that the temperature behavior of BB EL does not only reflect the material quality. It is overlaid by the electrical properties again.

The contribution of these investigations for further investigation on thin films is given by emphasizing the fact that the temperature behavior of EL is not totally related to the material quality, as in PL. But it is mainly related to the impact of surface recombination/surface passivation, which is very important on thin-film samples, because of the high amount of interfaces and thin layers.

## 6.2 Distribution of defects and breakdown sites in UMG-Si cells studied by luminescence imaging

The breakdown voltage of solar cells is an important parameter characterizing their quality. A low breakdown voltage indicates a high risk of damages of the entire solar module because of local heating in the module and therefore limiting the module's life span. The breakdown behavior of mc-Si solar cells has been investigated by lock-in thermography (LIT) [Bre2010] and electroluminescence imaging in forward (EL) and reverse biased mode (ReBEL) [Lau2009]. Breakdown is usually caused by two distinct mechanisms: avalanche breakdown and internal field emission [Kwa2009]. The breakdown sites are localized at defect regions of a solar cell. A classification of the breakdown types was established by different groups depending on their appearing voltage and voltage dependence [Kwa2009, Bre2011]. Several approaches to explain the origin of the breakdown behavior were published over the last years. Some of them are ohmic shunts, contamination of the wafer surface with Al particles prior to the phosphorous diffusion step specifically for breakdown type 1 [Lau2010] and clusters of oxide precipitates [Bot2009]. Nevertheless, the origin of the breakdown behavior in silicon solar cells is still under discussion.

This chapter deals with new aspects of the breakdown, focusing on differences and interactions between the defects exhibiting dislocation-related luminescence at room temperature (especially D1 [Kos1999]) and defects exhibiting ReBEL.

### Investigated samples:

Solar cells (15 cm x 15 cm) made from upgraded metallurgical grade silicon (UMG-Si) of two different materials qualities were used for the investigations. The cells exhibit significant differences in their dark I-V characteristics (especially break down behavior).

### Results and Discussion:

Electroluminescence images were acquired at room temperature using the PL Imaging setup. But electrical current was applied for excitation instead of LED light. EL spectra were measured by the same system of spectrometer and detector, which was used for investigations of the anomalous temperature behavior of EL, in the previous sub-chapter.

The typical ReBEL spectrum included in figure 6.2.1 shows a broad peak between 1000 and 1800 nm. At longer wavelength, beginning with 2000 nm, a very intense broad signal is observed. This must be related to heat, because of its increase with time and the spectral correlation with signal, which are typically detected by LIT. As compared to previous reports

## 6. Electroluminescence investigations on bulk mc-Si solar cells

[Chy1956, New1955] no light emission in the visible range (400 - 800 nm) was observed. ReBEL in the near-infrared part of light was not yet reported, up to now

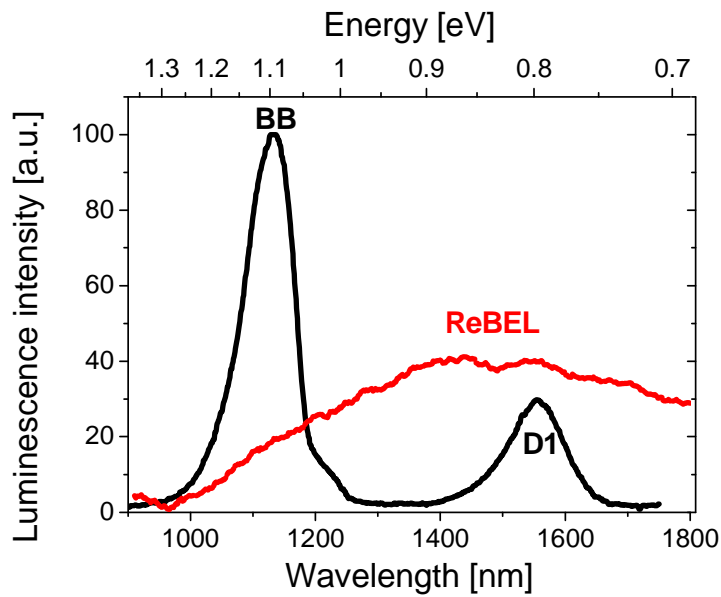
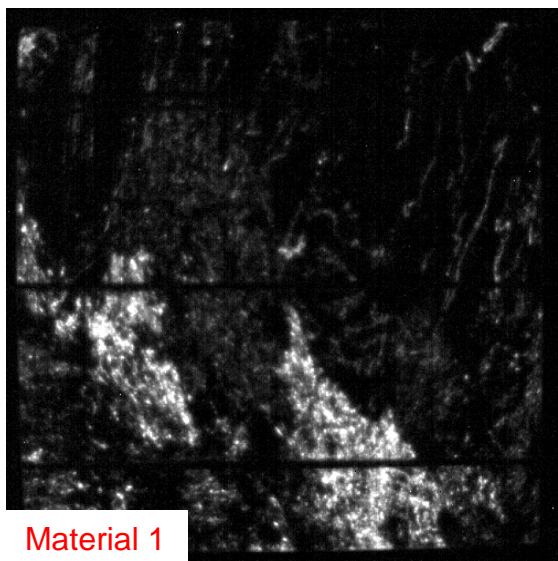
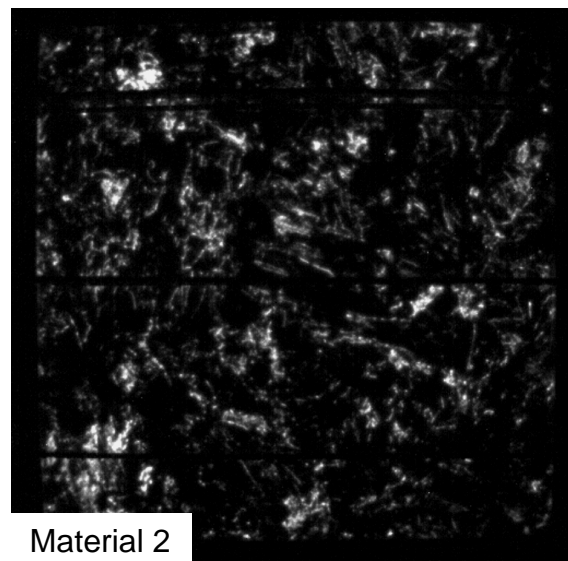


**Figure 6.2.1:** Examples of PL and ReBEL spectra at 300 K on defect regions in mc-Si.

The correlation between electrical properties and ReBEL is demonstrated in figure 6.2.2. Figures 6.2.2(a, b) show the distribution of the ReBEL emission observed for  $25 \text{ mA/cm}^2$ . The relation between the total ReBEL intensity spectrally integrated over the entire solar cells and the applied reverse voltage (data points) is shown in figure 6.2.2(c). It correlates almost 1 to 1 with the dark I-V characteristics (lines). Breitenstein et al. [Bre2011] suggested such a correlation.



(a)



(b)

## 6. Electroluminescence investigations on bulk mc-Si solar cells

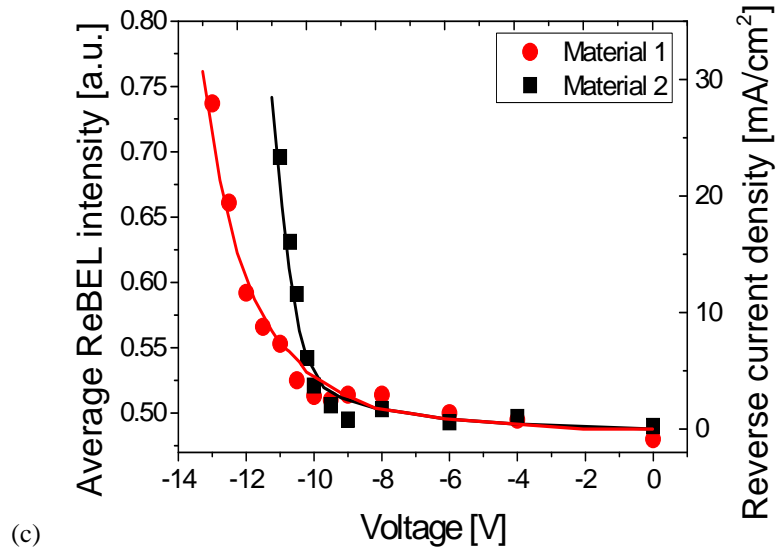
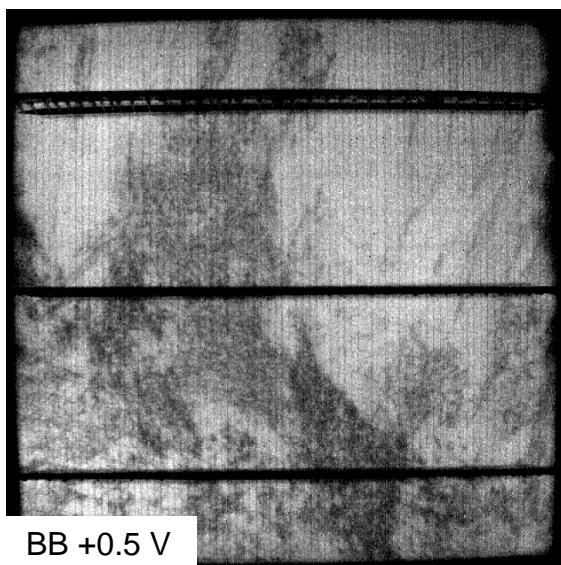
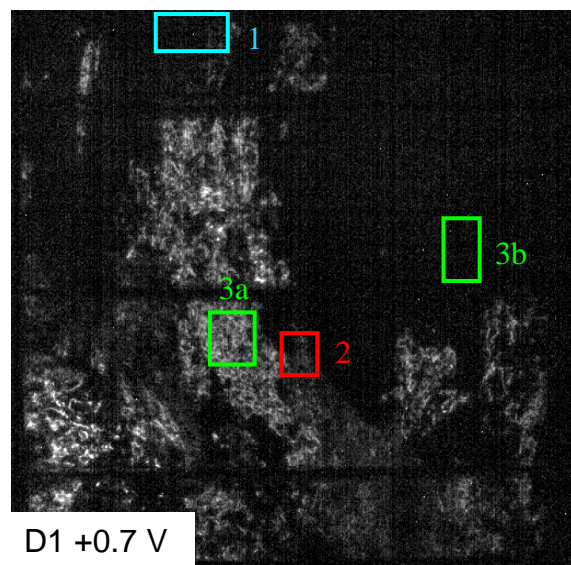


**Figure 6.2.2:** Correlation between ReBEL and electrical properties on complete mc-Si solar cells: ReBEL of material 1 (a); ReBEL of material 2 (b); correlation of ReBEL overall intensity (data points) and dark I-V characteristics (lines) (c).

More details about the spatial distribution of the luminescence image of the cell of material 1 are shown in figure 6.2.3. The standard BB image (Fig. 6.2.3(a)) illustrates the distribution of carrier lifetime. Regions of reduced BB intensity indicate recombination-active defects. The distribution of crystal defects causing D1 luminescence band is visualized in the D1 image (Fig. 6.2.3(b)). Figure 6.2.3(c) shows the ReBEL distribution. Certain regions of different breakdown types can be distinguished depending on their intensities and voltage dependences. Regions with different breakdown types are marked in figures 6.2.3(b, c) by rectangles. The corresponding voltage dependences of the different types are given in figure 6.2.3(d). Breakdown type 1 shows linear voltage dependence from about -5 V to -13 V. Extended regions of breakdown type 2 start to appear at -8 V to -9 V, emitting ReBEL with exponential voltage dependence. This breakdown type is correlated with a low D1 intensity in its vicinity.

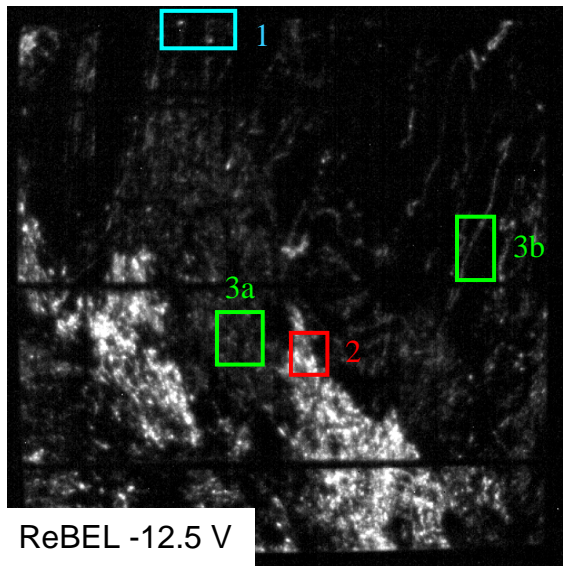


(a)

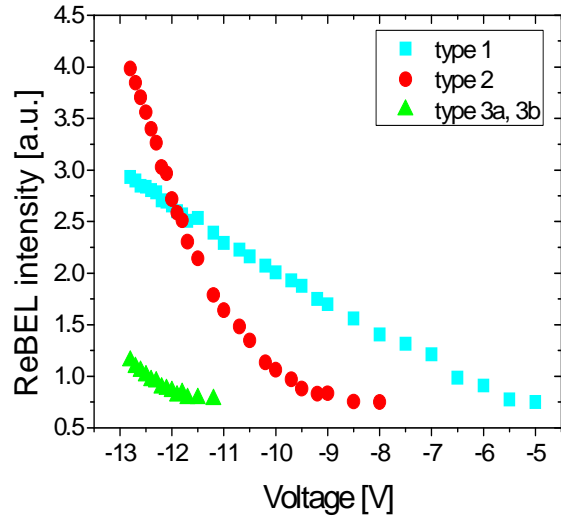


(b)

## 6. Electroluminescence investigations on bulk mc-Si solar cells



(c)



(d)

**Figure 6.2.3:** Spatial distribution of luminescence on complete mc-Si solar cells: BB at +0.5 V (a), D1 at +0.7 V (b), ReBEL at -12.5 V (c) and voltage dependence of the different breakdown types 1, 2, 3a and 3b (d). Corresponding regions are marked in figures (b) and (c).

Breakdown type 3 is the most important one for the electrical properties of the solar cells. That means the voltage at which it appears correlates with the beginning of the breakdown in the I-V characteristics. This voltage differs from solar cell to solar cell. The classification of types 1-3 is very similar to previous reports [Kwa2009, Bre2011]. Two regions of this breakdown type 3 are marked in figure 6.2.3 and are labeled 3(a) and 3(b).

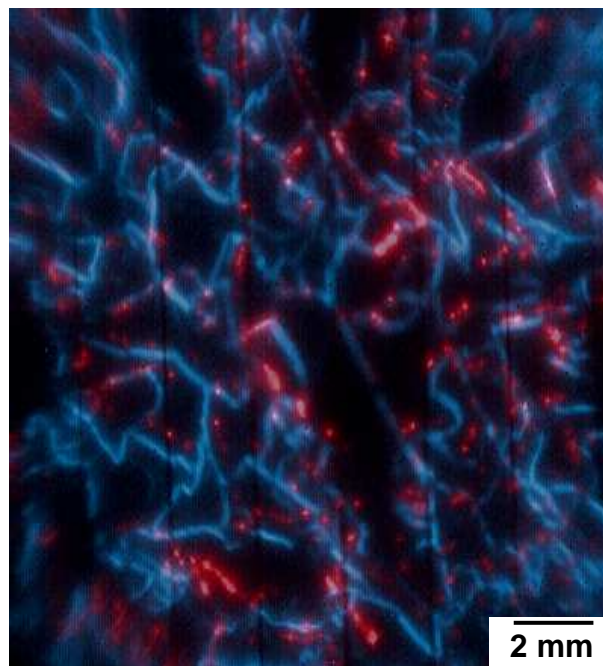


**Figure 6.2.4:** Superposition of D1 (blue) and ReBEL (red) in region 3a in figure 6.2.3. The spatial resolution is about 50  $\mu\text{m}$ .



## 6. Electroluminescence investigations on bulk mc-Si solar cells

Previously it was assumed that defects exhibiting D1 luminescence under forward bias should also exhibit ReBEL [Bot2009]. This hypothesis bases on low resolution imaging. Figure 6.2.4, however, which shows the region 3a with higher magnification, clearly demonstrates a spatial separation of defects emitting D1 luminescence (blue network-structures) and of defects emitting ReBEL (red spots).

This is a very surprising result and forces the implication that grain boundaries and other defects emitting D1 luminescence do not take part in the breakdown. It must be pointed out that in the vicinity of defects emitting D1 luminescence only breakdown sites emitting ReBEL of type 3 could be detected, but neither type 1 nor type 2.

The neighborhood of defects emitting the type 3 ReBEL and of defects emitting D1 luminescence indicates a possible relation between both defects. A corresponding region is labeled 3a in figure 6.2.3. Other breakdown sites - labeled 3b in figure 6.2.3 - show the same voltage dependence, but exhibit no local relation to defects emitting D1 luminescence. Because of this behavior it is possible that these defect types differ in their origin of ReBEL. Therefore a separation of the breakdown type 3 [Kwa2009, Bre2011] into 3a and 3b was suggested. Type 3a is directly correlated to the presence of D1 in its vicinity. The other type 3b has the same voltage dependence but appears independent on defects emitting D1 luminescence.

### **Summary and conclusion:**

Electroluminescence imaging of BB and D1 could be correlated with ReBEL in the near-infrared part of UMG-silicon solar cells whereas in the visible part of the spectrum no light was observed. The correlation between the electrical properties (dark I-V characteristics) and ReBEL has been confirmed. A spatial separation between defects and grain boundaries emitting D1 luminescence and defects emitting ReBEL was observed by high resolution imaging. Moreover, an interaction between radiative defects and non-radiative defects in the vicinity has been indicated. This could lead to a reduced affinity for breakdown in the vicinity of radiative defects. The existence of an additional breakdown type has been supported, which is characterized by the presence of intense D1 luminescence in the vicinity.

The results of these first measurements [Klo2012] were deepening investigated with microscopic methods (including EBIC) indicating that breakdown sites heavily attract excess charge carriers. Therefore, these carriers cannot recombine radiative at the neighboring extended defects. This may explain the missing D1 luminescence at breakdown sites [Man2012a].

The applicability of these investigations on thin-film solar cells seems to be limited on large grained or poly-Si films, where defects are comparable to those in mc-Si. So it is probable that the observed relation between defects and breakdown sites is transferable. The transfer to a-Si:H and  $\mu\text{c-Si:H}$  cells seems to be very limited.

## 7. Summary and conclusion

This chapter is designed to conclude and summarize the results, which were obtained in the part of the thin-film samples. The investigations on the mc-Si solar cells will be mentioned very shortly. The chapter will not give a general summary and conclusion about the different Si thin-film samples. That was already done in the corresponding chapters. Instead of this, it will discuss the obtained results with a focus on the three key-questions of this work. Note that these key-questions were not only investigated on Si thin films as reported in this work, but also on other thin-film samples (e.g. CIS). The questions and the corresponding answers are:

### 1. How to correct/minimize thin-film effects?

Most thin-film effects, such as interface recombination, parasitic luminescence from other sources etc., are known in principle. Nevertheless, the difficult part of every characterization/investigation process is to determine the exact impact on a specific type of sample. Some simple rules can help to reduce this impact of the thin layers/samples and should be considered before the actual characterization/investigation process starts.

- Investigations of partly processed samples are necessary. They allow the attribution of signals to specific layers of the completely processed samples. Moreover, it can reveal interactions between different layers and/or the impact of several treatments on the layers (see: chapter 4).
- Another limiting point on the investigation of partially processed samples is that the production of the required samples is sometimes very tricky or even impossible. For instance,  $\mu\text{c-Si:H}$  films could not be deposited directly on TCO as in the case of the corresponding a-Si:H/ $\mu\text{c-Si:H}$  tandem cells. An additional wetting layer ( $\text{SiN}_x$ ) is necessary and even though the stabilized layer thickness is very low compared to the tandem cells. That enhances the impact of interface recombination and can affect structural and optical properties of the Si films due to the enormous impact of various deposition conditions.
- Investigations should be performed in different setups/geometries. This can be helpful to correct/minimize thin-film effects, because of various sensitivities to several effects of thin films. For instance, the cross-section PL setup is not sensitive to optical interferences. A disadvantage is the unavoidable dependence of the PL intensity on the layers thickness. Another one is the missing possibility for scanning PL. All these disadvantages vanish in case of Standard PL setup on the cost of optical interferences.
- Combinations of several investigation techniques are very helpful to minimize thin-film effects, even if all used techniques are affected by the same effect. An example for this is the enhancement of recombination at interfaces. It affects both, EBIC and PL measurements, despite of the different physical mechanisms. Important is the different magnitude of the impact (see: sub-chapter 3.2). That allows rough estimations about the exact impact of thin-film effects for each technique. Sometimes techniques exhibit complementary sensitivities to different components of the sample. Then these techniques can be used

## 7. Summary and conclusion

to investigate the components of the sample independently of each other (e.g. Raman vs. PL and EBIC vs. PL in sub-chapter 5.1).

It is not possible to eliminate the thin-film effects completely, despite of adjustments of the investigation process and the knowledge about several effects in thin films (see: sub-chapter 2.3) It must be considered that most of the suggested procedures slightly affect the corrected data. For instance, deconvolutions of spectra can lead to reduced spectral resolution, especially in case of very intense parasitic signals (see: sub-chapter 5.2). For that reasons it is from high importance to determine limitations for every applied technique on specific thin-film samples.

The first limitation for all techniques, which base on the generation of electron-hole pairs by excitation (PL, EBIC, etc.), is the actual excitation depth. Note that this often differs from the physically defined depth. An example for this is the physically defined penetration depth of light by the Beer-Lambert law (see: sub-chapter 2.3). If the investigated layer/sample is thicker than this excitation depth, it can be assumed that spectral features keep unaffected. Nevertheless, other features, such as intensities and spatial distributions, can be still affected by various thin-film effects. The second limitation is the diffusion length of the excess carriers. It is usually limited by layer/sample thicknesses due to recombination at interfaces. It appears more often than the limitation by the generation depth. It can affect almost every feature of the obtained data (e.g. strongly reduced signal intensities, specific spatial distributions caused by structured interfaces, etc.).

### **2. What knowledge/methods can be transferred from bulk Si to thin-film ones?**

In principle, all characterization/investigation techniques can be used on thin-film samples, if thin-film effects are considered.

Often investigation techniques do not provide the same kind of data as in bulk materials, for what the techniques are designed for. One example for this is the camera-based PL Imaging setup. It is designed for luminescence imaging of mc-Si wafers with a long-wave LED array for optimal PL signal. On thin-films, the emitted luminescence intensity is too low for typical camera systems. Instead of this, the transmitted excitation light gives an approach to the actual layer thickness as well as topographical information about several layers of the stack (see: sub-chapter 3.1).

PL features of large grained silicon (grain sizes of about hundred micrometres) are almost completely comparable with those on bulk mc-Si, after removing of parasitic luminescence. That means the typical BB and defect-related luminescence can be observed and the features behave like in mc-Si. Note that such samples still require careful interpretation of the corrected data, considering thin-film effects. For instance, the spatial resolution of scanning PL must be higher to detect grain boundaries due to the lower effect of shadowing or smaller grain sizes (see: chapters 3 and 4). High resolution in the range of a few micrometres requires other setups (e.g. confocal PL). That amplifies the problem of laser-induced modifications of the samples due to the related higher focus of the laser beam. However, it is not sure that these setups can actually reveal the desired spatial resolution. It is possible that other thin-film effects (e.g. deviations of layer thickness, interface recombination) restrict the available resolution additionally.

## 7. Summary and conclusion

Also at lower grain sizes (few micrometers), luminescence feature known from mc-Si can be observed. However, in these cases the intensity of BB luminescence is drastically reduced or even not present due to the high impact of grain boundaries. Such PL spectra are dominated by DRL. These luminescence features are comparable to those on bulk mc-Si. Moreover they allow knowledge transfer from bulk Si to thin-film ones and backwards. For instance, detected oxide precipitates in poly-Si thin films treated by high-temperature RTP-processes were found to be possible evolution steps of those OP's observed in bulk mc-Si (see: chapter 4).

In other cases, the transfer of knowledge from mc-Si is more complicated. Shifts of the crystalline Raman peak are a strong indication for stress in mc-Si. On thin films, this approach is strongly limited by additional shift of the Raman peak induced by different crystalline quality (see: sub-chapter 4.2).

Among all thin-film effects, recombination at interfaces seems to be the most critical one. It affects spectral features, spatial distributions and reduces the signal intensity drastically. However, the most critical point is that interface recombination cannot be eliminated in any way. Slight reductions of the impact can be obtained by investigations of partially processed samples due to different affinities of recombination at interfaces depending on the exact interface composition (e.g. Si/air or Si/metal contact) (see: sub-chapter 5.1). But this positive effect is rather low. It is not possible to passivate the surfaces by HF dip or other acids, which are commonly used on mc-Si wafers. Such treatment could damage and possibly destroy the thin layers. Besides, thin amorphous and microcrystalline Si layers are already passivated by hydrogenation during the deposition process.

Analysis methods of luminescence features can be restrictedly transferred from bulk Si. The impact of thin films is always present and must be considered. One example for this is that extraction of the deactivation energy from temperature-dependent PL measurements. This method does not necessarily exhibit the barrier high between two bulk states but rather between a bulk and an interface state. Therefore, quantitative statements are not possible, but qualitative tendencies can be found. So it was possible to confirm the formation of grain boundaries (interfaces) within the layers during the transformation from a-Si:H to  $\mu\text{c-Si:H}$  because of decreasing deactivation energies with increasing crystallinity. Note that the actual thickness of a layer is one of the main reasons for enhanced interface recombination. In some cases, the effective layer thickness is higher than the expected one (e.g. tandem cells, where excess carriers can move through bottom and top cell).

### 3. What can be learned about the physical aspects of typical thin-film Si phases?

The optical properties of a-Si:H seem to be rather independent on deposition conditions compared to  $\mu\text{c-Si:H}$ . So no significant differences in PL features have been detected between literature data measured on bulk thicknesses (few micrometres) and thicknesses desired for thin-film solar cells (few hundred nanometers). The only indication of a different layer thickness comes from the extracted deactivation energies, which reveal high impact of interface recombination. Therefore it can be suggested that thin a-Si:H layers behave like bulk a-Si:H. In contrast to that exhibits  $\mu\text{c-Si:H}$  very strong dependences on deposition conditions (including layer thickness). That is probably caused by the fact that  $\mu\text{c-Si:H}$  is a more complex phase than a-Si:H as an intermediate phase between a-Si:H and c-Si.

## 7. Summary and conclusion

One of the main results of this work are PL- and Raman investigations on  $\mu\text{c-Si:H}$  layers of various crystallinities, which allow a suggestion of a stepwise transformation process from amorphous to microcrystalline silicon (see: sub-chapter 5.2).

1. At first ordinary a-Si:H becomes more ordered. That means the typical deviations of bond length and bond angle become reduced to a more ordered form – ‘a’-Si:H.
2. Single isolated nc-Si:H grains starts to crystallize in ‘a’-Si matrix. A wide distribution of grain sizes appear. The average size is around 1 nm.
3. Bigger nc-Si:H grains start to agglomerate to  $\mu\text{c-Si:H}$  columns, whereas smaller nc-Si:H grains remain in ‘a’-Si:H matrix.
4. Smaller nc-Si:H grains become directly embedded into the  $\mu\text{c-Si:H}$  columns.
5. The grains in the microcrystalline columnar structures grow further and order to a more compact structure with increasing crystallinity. The density of grain increases.
6. Increasing radiative recombination at defects in  $\mu\text{c-Si:H}$  can be associated with the increasing impact of  $\mu\text{c-Si:H}/\mu\text{c-Si:H}$  grain boundaries. Therefore, it becomes dominant at very high values of crystallinity. The average grain size is around 10 nm.

The entire process is characterized by a high level of stress within the  $\mu\text{c-Si:H}$  films.

Comparisons with theoretical models show quite good agreements. For instance, the suggested ordered form of a-Si:H (‘a’-Si:H) could be associated with a-Si:H, which is affected by structural changes induced by hydrogen, where the interactions with hydrogen results in substitution of stronger Si-Si bonds instead of weak a-Si:H bonds. This provides the basis for the formation of nc-Si:H. A special care should be on the presence of ‘a’-Si:H and ‘nc’-Si:H. Further investigations of these phases seem to be very interesting.

Investigations on wafer based mc-Si solar cells could provide an approach for knowledge transfers to thin-film Si about the efficiency of surface recombination (anomalous temperature behavior of BB EL) and the characterization of breakdown sites.

Of course, the results are not suitable to answer the three key-questions totally. I do not believe that this is possible at all. However, it was able to found some basic statements about investigations of thin films and its comparability with bulk materials. These can be used as starting point for further investigations on other thin-film samples. However, in real investigation or characterization processes the specific properties of the actual sample cannot be generalized in any way.

# List of abbreviation and symbols

$\alpha$  – absorption coefficient  
a-Si:H – hydrogenated amorphous silicon  
 $B$  – radiative recombination coefficient  
BB – band-to-band  
BC – back contact  
c-Si – crystalline silicon  
Cz-Si – monocrystalline silicon produced by Czochralski method  
DRL – defect-related luminescence  
 $E_c$  – energy position of the conduction band  
 $E_d$  – deactivation energy  
 $E_g$  – band gap energy of silicon  
 $E_v$  – energy position of the valence band  
EBIC – electron-beam induced current  
EL – electroluminescence  
FZ-Si – monocrystalline silicon produced by float zone method  
 $g$  – grain size  
 $h$  – Planck's constant  
i-Si – intrinsic silicon  
 $k$  – Boltzmann's constant  
 $L$  – diffusion length  
 $\lambda$  – wavelength  
mc-Si – multicrystalline silicon  
 $\mu$ c-Si:H – hydrogenated microcrystalline silicon  
 $n$  – electron concentration  
 $\nu$  – frequency  
n-Si – n doped silicon  
nc-Si:H – hydrogenated nanocrystalline silicon  
OP's – oxide precipitates  
 $p$  – hole concentration  
p-Si – p doped silicon  
PL – photoluminescence  
PV – photovoltaic  
 $R$  – recombination rate  
REBEL – reverse-biased electroluminescence  
SRH – Shockley-Read-Hall  
 $T$  – temperature  
 $\tau$  – excess carrier lifetime  
TCO – transparent conductive oxide  
TEM – Transmission-electron microscope  
TD's – thermal donors  
UMG-Si – multicrystalline silicon produced from upgraded metallurgical grade silicon  
 $X_C$  – Raman-crystallinity

# References

## Publication/presentations related to the Ph.D. thesis:

- A. Klossek, T. Arguirov, T. Mchedlidze, M. Kittler, ‘Anomalous temperature behavior of band-to-band (BB) EL in mc-Si solar cells’, EMRS Spring Meeting, June 7-11 2010, Strasbourg (France)
- A. Klossek, T. Arguirov, T. Mchedlidze, M. Kittler, *Phys. Stat. Sol. (c)* **8**, 911 (2011)
- A. Klossek, C. Krause, T. Arguirov, W. Seifert, M. Kittler, D. Amkreutz, M. Schmidt, ‘Characterisation of thin-film samples by Photoluminescence and correlation between PL and EBIC’, 48. Punktdefekttreffen, October 13-14 2011, Dresden (Germany)
- A. Klossek, D. Mankovics, M. Kittler, ‘Distribution of defects and breakdown sites in UMG-Si cells studied by luminescence imaging’, SiliconPV conference, April 3-5 2012, Leuven (Belgium)
- A. Klossek, D. Mankovics, M. Kittler, *Energy Procedia* **27**, 143-146 (2012)
- A. Klossek, C. Krause, T. Arguirov, H.-M. Krause, W. Seifert, F. Friedrich, S. Calnan, O. Gabriel, B. Stannowski, M. Kittler, ‘Characterisation of thin-film a-Si/ $\mu$ c-Si tandem solar cells on glass substrate’, EMRS Spring Meeting, May 14-18 2012, Strasbourg (France)
- A. Klossek, C. Krause, T. Arguirov, H.-M. Krause, W. Seifert, F. Friedrich, S. Calnan, O. Gabriel, B. Stannowski, M. Kittler, *Cryst. Res. Technol.* **48**, 5 (2013)

- [Ale1990] H. Alexander; “Versetzen in Halbleitern” in *Festkörperforschung für die Informationstechnik* (ed. R. Hölzle and W. Schmitz), Vorlesungsmanuskripte (1990)
- [Ami2004] S. Amiruddin, et al., 14th International Photovoltaics Science and Engineering Conference (PVSEC-14), Bangkok, Thailand, pp. 111–112. (2004)
- [Amk2011] D. Amkreutz, J. Müller, M. Schmidt, T. Hänel and T. F. Schulze, *Prog. Photovolt: Res. Appl.*, **19**, 8, 937-945 (2011)
- [Arg2002] T. Arguirov, W. Seifert, M. Kittler, and J. Reif, *J. Phys.: Condens. Matter* **14** 13169-13177 (2002)
- [Arg2003] T. Arguirov, W. Seifert, M. Kittler, J. Reif, *Mat. Sci. Eng. B* **102**, **251** (2003)
- [Arg2007] T. Arguirov, W. Seifert, G. Jia, M. Kittler, *Semiconductors* **41**, 405 (2007)
- [Arg2007a] T. Arguirov, Electro-optical properties of dislocations in silicon and their possible application for light emitters. PhD thesis, BTU Cottbus (2007)
- [Arg2007b] T. Arguirov, W. Seifert, G. Jia, and M. Kittler, *Semiconductors*, **41** (4), 436 (2007)
- [Ayr2002] R. R. Ayra, D. E. Carlson, *Prog. Photovoltaics* **10**, pp. 67-68 (2002)

## References

- [Bab1995] T. Baba, et al., 13th European Photovoltaic Solar Energy Conference (EUPVSEC-13), pp. 1708–1711 (1995)
- [Bal1983] M. Balkanski, R. F. Wallis, E. Haro, Phys. Rev. B **28**, 1928–1934 (1983)
- [Bat2003] J. Batista, A. Mandelis, D. Shaughnessy, Appl. Phys. Lett. **82**, 4077 (2003)
- [Bha1983] P. K. Bhat, G. Diprose, T. M. Searle, I. G. Austin, P. G. LeComber, and W. E. Spear, Physica **117B** & **118B**, 917-919 (1983)
- [Bebb1972] H. B. Bebb, E. W. Williams, Semiconductors and Semimetals, edited by R. K. Willardson and A. C. Beer, Academic, New York, Vol. **8**, p. 181 (1972)
- [Bec2011] C. Becker, T. Sontheimer, S. Steffens, S. Scherf, Bernd Rech, Energy Procedia **10**, 61-65 (2011)
- [Ber1997] R. B. Bergmann, G. Oswald, M. Albrecht, V. Gross, Solar Energy Materials and Solar Cells, **46**, 147-155 (1997)
- [Ber1999] R. B. Bergmann, Appl. Phys. A Materials Science & Processing, **69**, 2, 187–194 (1999)
- [Bin2002] S. Binetti, S. Pizzini, E. Leoni, R. Somaschini, A. Castaldini, J. Appl. Phys. **92**, 2437 (2002)
- [Bot2009] K. Bothe, K. Ramspeck, D. Hinken, C. Schinke, J. Schmidt, S. Herlufsen, R. Bredel, J. Bauer, J.-M. Wagner, N. Zakharov, O. Breitenstein, J. Appl. Phys. Lett. **106**, 104510 (2009)
- [Bou1983] F. Boulitrop, A. Chenevas-Paule, and D. J. Dunstan, Solid State Communications, **48**, 2, pp. 181-184 (1983)
- [Bre2008] O. Breitenstein, J. Bauer, M. Kittler, T. Arguirov, W. Seifert, SCANNING VOL. **30**, 331–338 (2008)
- [Bre2010] O. Breitenstein, Lock-in Thermography-Basics and Use for Evaluating Electronic Devices and Materials, 2nd ed. Springer, Berlin (2010)
- [Bre2011] O. Breitenstein, J. Bauer, K. Bothe, W. Kwapil, D. Lausch, U. Rau, J. Schmidt, M. Schneemann, M. C. Schubert, J.-M. Wagner, W. Warta, J. Appl. Phys. **109**, 071101 (2011)
- [Bren1995] R. Brendel, M. Hirsch, R. Plieninger, J. H. Werner, In Proc 13th Europ. Photovolt. Solar Energy Conf., p. 432 (1995)
- [Bus1988] E. Bustarret, M. A. Hachicha, M. Brunel, Appl. Phys. Lett. **52**, 1675 (1988)
- [Car1997] R. Carius, F. Finger, U. Backhausen, M. Luysberg, P. Hapke, M. Otte, H. Overhof, Materials Research Society Symposium Proceedings **467**, 283 (1997)
- [Cav1993] A. Cavallini, M. Vandini, F. Corticelli, A. Parisini, A. Armigliato, Inst. Phys. Conf. Ser. **134**, 115 (1993)
- [Che1952] I. C. Cheeseman, Proc. Phys. Soc. A **65**, 25 (1952)
- [Chy1956] A. G. Chynoweth and K. G. McKay, Phys. Rev. **102**, 269 (1956)
- [Das2003] D. Das, Solid State Communications **127**, 453–456 (2003)
- [Dec1983] H. W. Deckman, C. B. Roxlo, E. Yablonovitch, Optics Letters **8**, 9 (1983)
- [Der1981] H. Dersch, J. Stuke, J. Beichler, Appl. Phys. Lett. **38**, 456 (1981)
- [Die1998] F. Diehl, B. Schroder, H. Oechsner, (1998), J. Appl. Phys. **84** (6), 3416 (1998)
- [Dre2011] F. Dreckschmidt and H.-J. Möller, Phys. Status Sol. (c) **8**, 4 (2011)
- [Dro1976] N. A. Drozdov, A. A. Patrin, V. D. Tkatchev, Sov.-Phys. JETP Lett. **23**, 597 (1976)
- [Dro1977] N. A. Drozdov, A. A. Patrin, V. D. Tkatchev, Phys. Stat. Sol. (b) **83**, K137 (1977)
- [Dro1981] N. A. Drozdov, A. A. Patrin, V. D. Tkatchev, Phys. Stat. Sol. (a) **64**, K63 (1981)
- [Dzi1977] J. Dzierwior, W. Schmid, Appl. Phys. Lett. **31**, 346 (1977)
- [Eng1973] D. Engemann, R. Fischer, Amorphous and Liquid Semiconductors, London: Taylor& Francis Ltd., 947 (1973)



## References

- [Eng1977] D. Engemann, R. Fischer, *Phys. Stat. Sol. (b)* **79**, 195 (1977)
- [Feh1997] F. P. Fehlner, *J. Non-Cryst. Solids* **218**, 360 (1997)
- [Fin1997] F. Finger, R. Carius, P. Hapke, L. Houben, M. Luysberg, M. Tzolov, *Materials Research Society Symposium Proceedings* **452**, 725 (1997)
- [Fuh2002] W. Fuhs, *PVNET Workshop Proceedings, RTD Strategies for PV, Ispra, Italy*, pp. 172–175 (2002)
- [Fuk1996] S. Fukatsu, Y. Mera, M. Inoue, K. Maeda, H. Akiyama, H. Sakaki, *Appl. Phys. Lett.* **68**, 1889 (1996)
- [Fuj1998] M. Fujii, M. Yoshida, S. Hayashi, and K. Yamamoto, *J. Appl. Phys.* **84**, 4525 (1998)
- [Gan1970] S. Ganesan, A. A. Maradudin, J. Oitmaa, 1970 *Ann. Phys.* **56**, 556–94 (1970)
- [Ger1968] H. Gerischer, M. E. Michel-Beyerle, F. Reberstrost, H. Tributsch, *Electrochimica Acta* **13**, 6 (1968)
- [Gre1995] M. A. Green und M. J. Keevers, *Progress in Photovoltaics* **3**, 189 (1995)
- [Gre2003] M.A. Green, *Advances in Solar Energy*, American Solar Energy Society, pp. 187-814 (2003)
- [Gre2004] M. A. Green, P. A. Basore, N. Chang, D. Clugston, R. Egan, R. Evan, D. Hogg, S. Jarnason, M. Keevers, P. Lasswell, J. O’Sullivan, U. Schubert, A. Turner, S. R. Wenham, and T. Young, *Solar Energy* **77**, 6, 857-863 (2004)
- [Gre2012] M. A. Green, K. Emery, Y. Hishikawa, W. Warta, E. D. Dunlop, *Prog. Photovolt: Res. Appl.* **20**, 12–20 (2012)
- [Hah2003] G. Hahn and P. Geiger, *Prog. Photovolt: Res. Appl.* **11** 341–346 (2003)
- [Hal1952] R. N. Hall; *Phys. Rev.* **87**, 387 (1952)
- [Hal1959] R. N. Hall, *Proc. IEE B* **106**, Suppl. 17, 923 (1959)
- [Hig1992] V. Higgs, M. Goulding, A. Brinklow, P. Kighthley, *Appl. Phys. Lett.* **60**, 1369 (1992)
- [Hig1992a] V. Higgs, E. C. Lightowers, S. Tajbakhsh, P. J. Wright, *Appl. Phys. Lett.* **61**(9), 1087 (1992)
- [Hig1993] V. Higgs, M. Kittler, *Appl. Phys. Lett.* **63**, 2085 (1993)
- [Hou1998] L. Houben, M. Luysberg, P. Hapke, R. Carius, F. Finger, H. Wagner, *Philosophical Magazine A* **77**, 1447 (1998)
- [Ike1998] K. Ikeda, T. Sekiguchi, S. Ito, M. Suezawa, *Solid State Phenomena*, **63-64**, 481-488 (1998)
- [Im1993] J. S. Im, H. J. Kim, M. O. Thompson, *Appl. Phys. Lett.* **63**, 1969 (1993)
- [Jen1954] D. A. Jenny, R. H. Bube, *Phys. Rev.* **96**, 1190–1191 (1954)
- [Kaa2000] A. Kaan Kalkan, S. J. Fonash, C. Shang-Long, *Appl. Phys. Lett.* **77**, 55 (2000)
- [Kan1972] K. Kanaya, S. Okayama, *J. Phys. D* **5**, 48 (1972)
- [Kas2006] S. Kasap, P. Capper, C. Koughia, *Springer Handbook of Electronic and Photonic materials*, Springer Science + Buisness Media Inc., ISBN-10: 0-387-26059-5 (2006)
- [Kee2005] M. J. Keevers, A. Turner, U. Schubert, P. A. Basore, M. A. Green, Remarkably effective hydrogenation of crystalline silicon on glass modules, *Proc. of 20th European Photovoltaic Solar Energy Conference, Barcelona, Spain*, 226-229 (2005)
- [Ken2003] A. J. Kenyon, E. A. Steinman, C. W. Pitt, D. E. Hole, and V. I. Vdovin, *J. Phys.: Condens. Matter* **15**, 2843-2850 (2003)
- [Kit1993] M. Kittler, W. Seifert, V Higgs, *Phys. Stat. Sol. (a)*, **137**, 327-335 (1993)
- [Kit1995] M Kittler, W. Seifert, V. Higgs, *Mat. Res. Soc. Symp. Proc.* **378**, 989 (1995)
- [Kit1995a] M Kittler, W. Seifert, *Scanning Microscopy* **9**, 677 (1995)
- [Kle2003] S. Klein, F. Finger, R. Carius, T. Dylla, B. Rech, M. Grimm, L. Houben, M. Stutzmann, *Thin Solid Films* **430**, 1-2, 202-207 (2003)

## References

- [Klo2011] A. Klossek, T. Arguirov, T. Mchedlidze, M. Kittler, *Phys. Stat. Sol. (c)* **8**, 911 (2011)
- [Klo2012] A. Klossek, D. Mankovics, M. Kittler, *Energy Procedia* **27**, 143-146 (2012)
- [Klo2013] A. Klossek, C. Krause, T. Arguirov, H.-M. Krause, W. Seifert, F. Friedrich, S. Calnan, O. Gabriel, B. Stannowski, M. Kittler, *Cryst. Res. Technol.* **48**, 5 (2013)
- [Kno1996] J. Knobloch, S. Glunz, D. Biro, W. Wart, E. Schäffer, W. Wetling, *Proceedings of the 25th IEEE Photovoltaic Specialists Conference, Washington, DC*, **405–408** (1996)
- [Kos1999] Y. Koshka, S. Ostapenko, I. Tarasov, S. McHugo, J. P. Kalejs, *Appl. Phys. Lett.* **74**, 1555 (1999)
- [Kür1989] W. Kürner, R. Sauer, A. Dornen, and K. Thonke, *Phys. Rev. B* **39**, 18 (1989)
- [Kve1995] V. V. Kveder, E. A. Steinman, S. A. Shevchenko, H.G. Grimmeiss, *Phys. Rev. B* **51**, 10520 (1995)
- [Kve1996] V. V. Kveder, E. A. Steinman, and H. G. Grimmeiss, *Sol. Stat. Phen.* 47-48, 419 (1996)
- [Kve2001] V. Kveder, M. Kittler, W. Schröter, *Phys. Rev. B* **63**, 115208 (2001)
- [Kwa2009] W. Kwapil et al., *J. Appl. Phys.* **106**, 063530 (2009)
- [Lau2009] D. Lausch, K. Petter, H. v. Wenckstern, M. Grundmann, *Phys. Stat. Sol. RRL* **3**, pp.70-72 (2009)
- [Lau2010] D. Lausch, K. Petter, R. Bakowskie, C. Czekalla, J. Lenzner, H. v. Wenckstern, M. Grundmann, *Appl. Phys. Lett.* **97**, 073506 (2010)
- [Lec2002] P. Lechner and H. Schade, *Prog. Photovoltaics* **10**, pp 85-98 (2002)
- [Led2000] G. Ledoux, O. Guillois, D. Porterat, C. Reynaud, *Phys. Rev. B* **62**, 23 (2000)
- [Led2002] G. Ledoux, J. Gong, F. Huisken, O. Guillois, and C. Reynaud *Appl. Phys. Lett.* **80**, 4834 (2002)
- [Lel1992] Y. S. Lelikov, Y. T. Rebane, S. Ruvimov, A. A. Sitnikova, D. V. Tarhin, Y. G. Shreter, *Phys. Stat. Sol. (b)* **172**, 53-63 (1992)
- [Lia2008] N. M. Liao, W. Li, Y. D. Jiang, Y. J. Kuang, K. C. Qi, Z. M. Wu, S. B. Li, *Appl. Phys. A* **91**, 349–352 (2008)
- [Lon1977] D. A. Long, *Raman Spectroscopy*, McGraw-Hill International Book Company, New York (1977)
- [Luc2011] J. Luckas, S. Kremers, D. Krebs, M. Salinga, M. Wuttig, C. Longeaud, *J. Appl. Phys.* **110**, 013719 (2011)
- [Lul1987] G. Lulli, P. G. Merli, and M. V. Antisari, *Phys. Rev. B* **36**, 8038 (1987)
- [Luy1997] M. Luysberg, P. Hapke, R. Carius, F. Finger, *Philosophical Magazine A* **75** (1), 31 (1997)
- [Mac1955] G. G. Macfarlane and V. Roberts; *Phys. Rev.* **98**, 1865 (1955)
- [Man2012] D. Mankovics, R. P. Schmid, T. Arguirov, and M. Kittler, *Crystal Research and Technology* **47**, 11, pp 1148-1152 (2012)
- [Man2012a] D. Mankovics, A. Klossek, C. Krause, T. Arguirov, W. Seifert, M. Kittler, *Phys. Stat. Sol. (a)* **209**, 10 pp. 1908-1912 (2012)
- [Mat1996] T. Matsuyama, N. Terada, T. Baba, T. Sawada, S. Tsuge, K. Wakisaka, S. Tsuda, *J. Non-Cryst. Solids* **940**, 198–200 (1996)
- [Mat2004] A. Matsuda, *Journal of Non-Crystalline Solids* 338–340, 1–12 (2004)
- [McH1993] S. A. McHugo, W. D. Sawyer, *Appl. Phys. Lett.* **62**, 2519-2521 (1993)
- [Mch2009] T. Mchedlidze, O. Kononchuk, T. Arguirov, M. Trushin, M. Reiche, M. Kittler, *Sol. Stat. Phenom.*, **156-158**, 567-572 (2009)
- [Mch2011] T. Mchedlidze, J. Schneider, T. Arguirov, M. Kittler, *Phys. Stat. Sol. (c)* **8**, 1334 (2011)

## References

- [Mch2012] T. Mchedlidze, W. Seifert, M. Kittler, A. T. Blumenau, B. Birkmann, T. Mono, M. Müller, *J. Appl. Phys.* **111**, 073504 (2012)
- [Mch2012a] T. Mchedlidze, and M. Kittler, *J. Appl. Phys.* **111**, 053706 (2012)
- [Mei2002] J. Meier, J. Spitznagel, U. Kroll, C. Bucher, S. Faÿ, T. Moriarty, and A. Shah, *Sol. Energy Mater. Sol. Cells* **74**, 457(2002)
- [Meil2006] F. Meillaud, A. Shah, C. Droz, E. Vallat-Sauvain, and C. Miazza, *Sol. Energy Mater. Sol. Cells* **90**, 2952 (2006)
- [Mer2005] T. Merdzhanova, *Microcrystalline Silicon Films and Solar Cells Investigated by Photoluminescence Spectroscopy Vol. 41* Forschungszentrum Jülich GmbH Institut für Photovoltaik (2005)
- [Mer2006] T. Merdzhanova, R. Carius, S. Klein, F. Finger, D. Dimova-Malinovska, *Thin Solid Films* **511-512**, 394-398 (2006)
- [Mic1969] W. Michaelis and M. H. Pilkuhn, *Phys. Stat. Sol* **36**, 311 (1969)
- [Min1981] N. S. Minaev and A. V. Mudryi, *Phys. stat. sol. (a)* **68**, 561 (1981)
- [New1955] R. Newman, W. C. Dash, R. N. Hall, and W. E. Burch, *Phys. Rev.* **98**, 1536 (1955)
- [Ng2001] W. L. Ng, M. A. Lourenco, R. M. Gwilliam, S. Ledain, G. Shao, K. P. Homewood, *Nature* **410**, 192 (2001)
- [O'Re1991] B. O'Regan, M. Grätzel, *Nature* **353**, 737-740 (1991)
- [Ols1988] G. L. Olson and J. A. Roth, *Mater. Sci. Rep.* **3**, 1 (1988)
- [Ore1981] J. Orenstein, M. Kastner, *Phys. Rev. Lett.* **46**, 1421 (1981)
- [Oss1999] C. Ossadnik, S. Vepřek, I. Gregora, *Thin Solid Films* **337**, 148-151 (1999)
- [Ove1989] H. Overhof, P. Thomas, *Electronic Transport in Hydrogenated Amorphous Semiconductors*, Springer, Berlin (1989)
- [Pan1975] J. L. Pankove, *Optical Processes in Semiconductors*, Dover, New York 165-166 (1975)
- [Peu2003] P. Peumans, A. Yakimov, and S. R. Forrest, *J. Appl. Phys.* **93**, 7 (2003)
- [Poo2006] J. Poortmans, V. Arkhipov, John Wiley, "Thin film solar cells: fabrication, characterisation and application", edit and Sons Ltd., ISBN-13: 978-0-470-09126-5 (2006)
- [Piz2000] S. Pizzini, M. Guzzi, E. Grilli, and G. Borionetti, *J. Phys. Condens. Matter* **12**, 10131–10143 (2000)
- [Ric1981] H. Richter, Z. P. Wang., L. Ley, *Solid State Communications* **39**, 625 (1981)
- [Roo1954] W. van Roosbroeck, W. Shockley, *Phys. Rev.* **94**, 1558 (1954)
- [Ros2003] T. Roschek, „Microcrystalline Silicon Solar Cells Prepared by 13.56 MHz PECVD“, Dissertation Düsseldorf (2003)
- [Sau1985] R. Sauer, J. Weber, J. Stolz, E. R. Weber, K.-H. Küsters, H. Alexander, *Appl. Phys. A* **36**, 1 (1985)
- [Schl1974] H. Schlangenotto, H. Maeder, W. Gerlach; *Phys. Stat. Sol. (a)* **21**, 357 (1974)
- [Schm2011] R. Schmid, D. Mankovics, T. Arguirov, T. Mchedlidze, M. Kittler, *Phys. Stat. Sol. (c)* **8**, 1297 (2011)
- [Schr1990] D. K. Schröder, *Semiconductor Material and Device Characterization*, Wiley (1990)
- [Schu1997] E. F. Schubert, I. D. Goepfert, W. Grieshaber, J. M. Redwing, *Appl. Phys. Lett.* **71**, 7 (1997)
- [Sei2011] W. Seifert, D. Amkreutz, T. Arguirov, H-M. Krause, and M. Schmidt, *Sol. Stat. Phenom.* **178-179**, pp 116-121 (2011)
- [Sek1994] T. Sekiguchi, V. V. Kveder, K. Sumino, *J. Appl. Phys.* **76**, 7882 (1994)
- [Sek1996] T. Sekiguchi, K. Sumino, *J. Appl. Phys.* **79** (6) 3253-3260 (1996)
- [SGG2007] datasheet from Saint-Gobain Glass Visions (2007)

## References

- [Sha2004] A. Shah, et al., 14th International Photovoltaic Science and Engineering Conference (PVSEC-14), Bangkok, Thailand (Technical Digest), pp. 39–40 (2004)
- [Sho1952] W. Shockley and W. T. Read; *Phys. Rev.* **87**, 835 (1952)
- [Söd2010] T. Söderström, F.-J. Haug, V. Terrazzoni-Daudrix, and C. Ballif, *J. Appl. Phys.* **107**, 014507 (2010)
- [Spr1994] A. B. Sproul, *J. Appl. Phys.* **76** (5), 2851 (1994)
- [Sta1977] D. Staebler, C. Wronski, *Appl. Phys. Lett.* **31** 292 (1977)
- [Stan2002] B. J. Stanbery, *Solid State and Materials Science* **27**, 73 (2002)
- [Str1980] R. Street *Phys. Rev. B* **21**, 5775–5784 (1980)
- [Str1981] R. A. Street, *Advanced in Physics* **30**, 593 (1981)
- [Stu1987] M. Stutzmann, D. K. Biegelsen, R. A. Street, *Phys. Rev. B* **35** (11), 5666 (1987)
- [Sue1982] M. Suezawa, K. Sumino, Y. Nishina, *Jpn. J. Appl. Phys.* **21**, L518 (1982)
- [Sue1983] M. Suezawa, K. Sumino, *Phys. Stat. Sol. (a)* **78**, 639 (1983)
- [Sue1983a] M. Suezawa, Y. Sasaki, and K. Sumino; *Phys. Stat. Sol. (a)* **79**, 173 (1983)
- [Sze1981] S. M. Sze, *Physics of Semiconductor Devices*, John Wiley & Sons, New York 2<sup>nd</sup> Edit. (1981)
- [Taj1992] M. Tajima, H. Takeno, and T. Abe, *Mater. Sci. Forum* **83-87**, 1327 (1992)
- [Taj1994] M. Tajima, H. Takeno, M. Warshina, and T. Abe, *Materials Science Forum* **143-147**, pp 147-152 (1994)
- [Taj1995] M. Tajima, M. Tokita, and M. Warashina, *Materials Science Forum Vols.* **196-201**, pp 1749-1754 (1995)
- [Tay1998] H. Tayanaka, K. Yamauchi, T. Matsushita, In *Proc. 2nd World Conference on Photovoltaic Solar Energy Conversion* (European Commission, Ispra) p. 1272 (1998)
- [Tin1991] T. Tinoco, C. Rincón, M. Quintero, G. Sanchez Pérez, *Phys. Stat. Sol. (a)* **124**, 2 (1991)
- [Tru2003] T. Trupke, M. A. Green, P. Würfel, P. P. Altermatt, A. Wang, J. Zhao, and R. Corkish, *J. Appl. Phys.* **94**, 4930 (2003)
- [Tzo1997] M. Tzolov, F. Finger, R. Carius, P. Hapke, *J Appl. Phys.* **81**, 7376 (1997)
- [Var1967] Y. P. Varshni; *Phys. Stat. Sol.* **19**, 459 (1967)
- [Vep1987] S. Vepřek, F.-A. Sarott, Z. Iqbal, *Phys. Rev. B* **36**, 3344 (1987)
- [Vet2000] O. Vetterl, F. Finger, R. Carius, P. Hapke, L. Houben, O. Kluth, A. Lambertz, A. Mück, B. Rech, H. Wagner, *Solar Energy Mater. & Solar Cells* **62**, 97-108 (2000)
- [Wan2010] W. Wang, G. Wang, B. Tian, W. Wan, Z. Du, *Chinese Sci Bull* **55**, 18 (2010)
- [Wei2005] L. Weinhardt, O. Fuchs, D. Groß, G. Storch, E. Umbach, N. G. Dhere, A. A. Kadam, S. S. Kulkarni, and C. Heske, *Appl. Phys. Lett.* **86**, 062109 (2005)
- [Wol1996] I. D. Wolf, *Semicond. Sci. Technol.* **11**, 139–154. (1996)
- [Wor1992] K. Woronek, J. Weber, A. Höpner, H. F. Ernst, R. Buchner, M. Stefaniak, H. Alexander, *Mater. Sci. Forum* **83-87**, 1315 (1992)
- [Wro1976] C. Wronski, *Appl. Phys. Lett.* **28**, 671 (1976)
- [Wro2001] C. R. Wronski, D. E. Carlson, *Clean Electricity from Photovoltaics*, Imperial College Press, pp. 199–236. (2001)
- [Wür1982] P. Würfel, *J. Phys. C* **15**, 3967 (1982)
- [Yue1999] G. Yue, J. Lorentzen, J. Lin, D. Han, Q. Wang, *Appl. Phys. Lett.* **75**, 492 (1999)
- [Yue2000] G. Yue, D. Han, D. L. Williamson, J. Yang, K. Lord, and S. Guha, *Appl. Phys. Lett.* **77**, 20, (2000)

# Acknowledgement

First of all, I would like to express my largest gratitude to Prof. Dr. Martin Kittler and to Prof. Dr. Jürgen Reif for giving me the opportunity to prepare my Ph.D. thesis at the Joint Lab of IHP and Brandenburg University of Technology.

My special thanks to Dr. Tzanimir Arguirov, he always stands on my side when I need help. I have learned a lot from him in so many ways, not only about scientific work. He made me really enjoy this time. He is a true 'master' in science and life.

I am very grateful to Dr. Winfried Seifert and Hans-Michael Krause for their support and helpful discussions. They performed EBIC-, EDX-measurements etc. without these techniques this work would be not possible.

I will also thank for the experienced discussions with Dr. Teimuraz Mchedlidze during my thesis.

I especially thank my co-Ph.D-students at the Joint Lab, Daniel Mankovics, Christoph Krause and Dr. Maxim Trushin. It made the work much more easy and enjoyable to have colleges in the same situation.

Our secretaries Marion Borrmann and Kathrin Starr are kindly acknowledged for their continuous help with all the small and big administrative problems.

I am very thankful for the good cooperation and atmosphere with the Joint Lab colleagues during this work at BTU Cottbus. I only mention a few of the names here, Bernhard Schwartz, Jürgen Bertram, Markus Holla, Markus Ratzke, Reiner Schmid, Olga Varlamova, Biwang Yang and so on.

I would like to acknowledge our project partners. As mentioned the most important project was the PVcomB project, where special thanks belongs to Dr. Felice Friedrich, Dr. Onno Gabriel and Dr. Bernd Stannowski for samples and support with other investigation techniques. Other project partners from HZB were Dr. Daniel Amkreutz, Simon Steffens etc.

Of course, I got great support from my family.